NASA Contractor Report 3612

Turbulent Boundary Layer Over Solid and Porous Surfaces With Small Roughness

Fred Y. Kong, Joseph A. Schetz,
and Fayette Collier

GRANT NAG-1-119
SEPTEMBER 1982

NASA

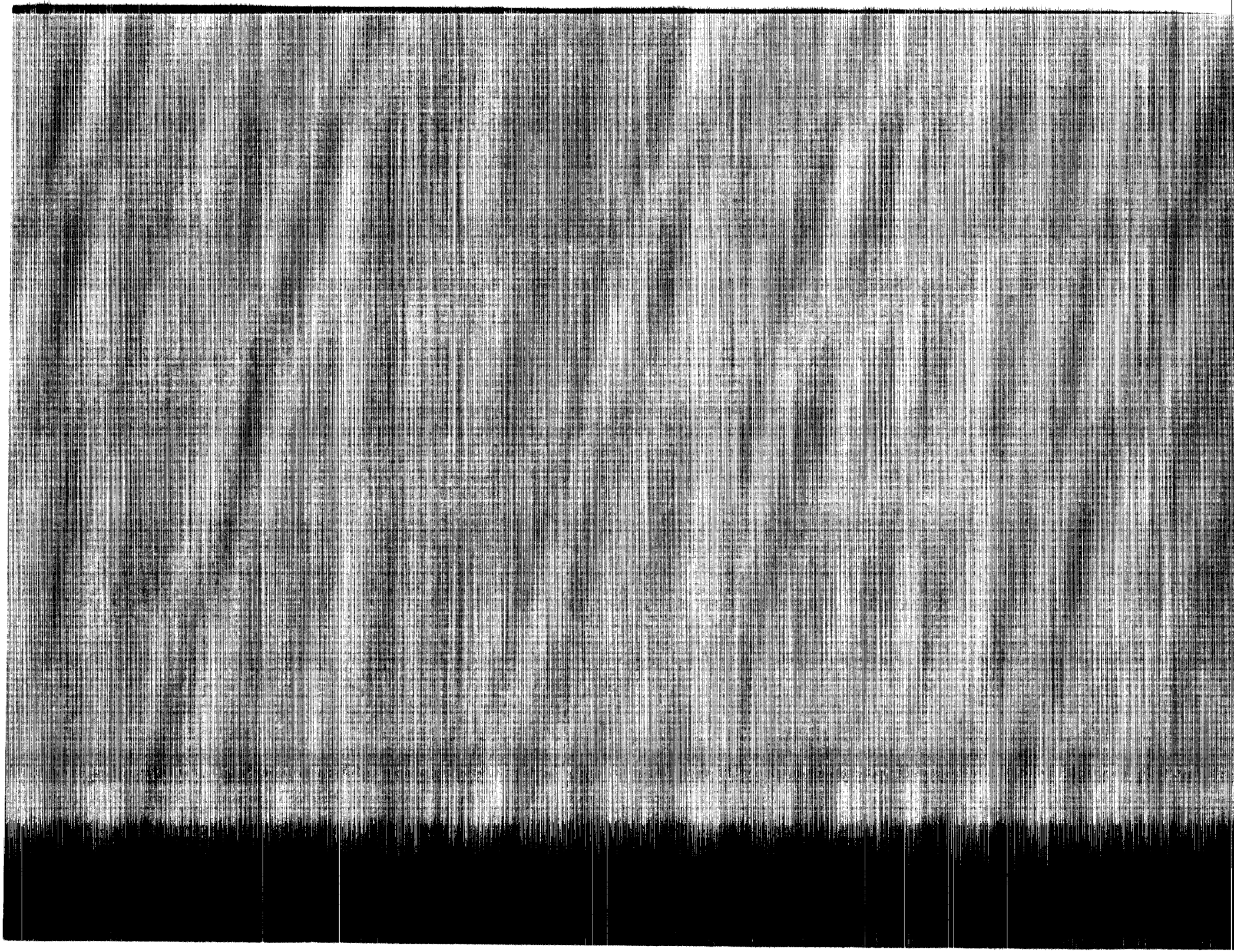

NASA Contractor Report 3612

Turbulent Boundary Layer Over Solid and Porous Surfaces With Small Roughness

Fred Y. Kong, Joseph A. Schetz,
and Fayette Collier
Virginia Polytechnic Institute and State University
Blacksburg, Virginia

Prepared for
Langley Research Center
under Grant NAG-1-119

National Aeronautics
and Space Administration

**Scientific and Technical
Information Branch**

1982

TABLE OF CONTENTS

LIST OF FIGURES

LIST OF TABLES

NOMENCLATURE

A	surface area of the element head.
C_f	skin friction coefficient
E	DC output
e	RMS output
F	axial force acting on the element head
K	sensitivity coefficient
k	roughness size
k^+	$= \frac{kU_*}{\nu}$ dimensionless roughness size
P_o	total pressure
P_∞, P_s	static pressure
q	dynamic pressure
Re_D	Reynolds number based on body diameter
Re_ℓ	Reynolds number based on length
Re_{δ^*}	Reynolds number based on displacement thickness
Re_θ	Reynolds number based on momentum thickness
S	Arc distance from body nose
U	local mean velocity
U_e	edge velocity
U_∞	freestream velocity
U^+	$= \frac{U}{U_*}$
U_*	$= \sqrt{\tau_w/\rho}$ skin friction velocity
$\sqrt{\frac{\overline{u'^2}}{U_e}}$	axial turbulence intensity
$\sqrt{\frac{\overline{v'^2}}{U_e}}$	normal turbulence intensity
$\overline{u'v'}$	Reynolds stress

W	weight
x	distance in the axial direction
Y	vertical distance from the wall
Y^+	$= \frac{YU_*}{\nu}$
τ_w	wall shear
ρ	density
ν	laminar kinematic viscosity
δ	boundary layer thickness
δ^*	displacement thickness
θ	momentum thickness

TURBULENT BOUNDARY LAYER OVER SOLID AND POROUS SURFACES WITH SMALL ROUGHNESS

By Fred Y. Kong, Joseph A. Schetz, and Fayette Collier
Virginia Polytechnic Institute and State University

INTRODUCTION

Over the years, considerable effort has been devoted to the study of turbulent boundary layer flow over porous or permeable surfaces with injection or suction. This work is important from the point of view of several practical applications such as: drag reduction on aerodynamic surfaces by maintaining laminar flow at high Reynolds numbers by suction, cooling of turbine blades by injection, boundary layer separation control by suction, aircraft thermal protection, engine noise abatement, etc. Some situations involve induced injection or suction by condensation or evaporation, such as: atmospheric flows over forests, lakes, and the ocean, chemical processing, drying operations. Therefore, a detailed understanding of the nature of turbulent boundary layers with injection or suction is of significant engineering importance.

The literature in this field is rich, and there have been a number of review articles that summarize all but the most recent work, Refs. (1) - (5). Some experimental and theoretical studies, Ref. (6) - (9), have been extended towards determining the form of the Law of the Wall, Eq. (1), suitable for cases with injection or suction, since that is the foundation for all turbulence transport models of the inner region no matter what the level of complexity. A controversy has arisen, and the problem can be traced directly to the determination of the wall shear. The accurate determination of this quantity

$$\frac{U}{U_*} = A \log \frac{YU_*}{\nu} + B \qquad (1)$$

is essential, since the so-called skin friction velocity, $U_* = \sqrt{\tau_w/\rho}$, enters directly into both coordinates on the Wall Law plot. Most workers have attempted to use either the slope of the velocity profile at the wall or the momentum integral equation to deduce the wall shear even though those techniques had been discredited years before for flows over solid surfaces. A notion of the poor reliability of those procedures can be obtained in Ref. (10) where the results of several variations of these techniques are compared. The reported results obtained in these ways for the more complicated case of flow over porous surfaces even with no injection or suction are further called into question because they do not agree with each other at the same Re_θ as shown in Fig. 1. It is a historical fact that the situation in the inner region of turbulent boundary layers on smooth, solid surfaces only became codified with the advent of direct measurements of skin friction with the floating element balances in the early 1950's.

The accuracy of the existing semi-empirical theories for flows over smooth, solid surfaces that have been built upon the directly measured wall shear data is sufficient for engineering estimation and design purposes. However, surfaces with some degree of roughness, which is unavoidable for any porous wall, present difficulties in the analysis. Specifically, even for roughness of intermediate size ($10 < k^+ < 70$), on a solid surface, it has been observed that each roughness pattern behaves in a characteristic way. The phenomenon is more complicated for the small roughness regime ($k^+ = 5 - 10$) as in Ref. (11). In that reference, Clauser presented the variation of the downward shift in the logarithmic region of the Wall Law, $\Delta (U/U_*)$ vs. k^+ for different roughness patterns. Since most of the porous surfaces necessarily involve some roughness, this extra complication must be taken into account carefully. Moreover, the effects of surface porosity, which allow small in- and out- flows through the surface even without applying injection or suction, adds further complications that are only now beginning to be understood. Thus, an important part of any injection or suction study must be a documentation of the flow over the surfaces of interest without injection or suction, so that the effects of surface roughness, porosity, and their combination can be displayed clearly. Also, the surface pattern of the porous material under study must be documented. Table I shows that few papers in the literature really concentrate on flows over porous surfaces without injection or suction and investigate the influences of surface roughness and porosity independently before considering injection or suction. This is another reason why there is no current theory which is considered to be reliable. It is necessary to understand these phenomena before analytical models can be built and further extension can be made to more complicated situations without confusion.

A previous investigation at Virginia Tech (Ref. 9) for flow over a sintered, porous wall of apparently small roughness had indicated a strong increase in wall shear without injection or suction. The values were higher than one might have expected for a rough, solid surface at the same k^+ if one makes some seemingly plausible assumptions about the relationship of a non-uniform sintered metal surface to uniform sand roughness on a solid surface. The measurements were made with a floating element balance. Control tests with a smooth, solid surface in the same model with the same instrumentation had yielded results in excellent agreement with established results. It was decided to repeat the tests using a non-porous wall with a clearly describable roughness in the same nominal range to clarify the situation. The points at issue were: 1) the influence of the porosity of the first wall and the possibility of small in- and out- flows and 2) the proper method of characterizing the roughness "size" of a non-uniform surface such as produced by sintering. For reference, an oblique-view, electron microscope photograph of the actual sintered, porous surface is shown in Fig. 2. The porous material is formed from metal powder with 70% of the particles in the range from 40 to 70 microns, with the rest smaller than 40 microns. If one takes 40 microns as a representative roughness size, a 600 grit sandpaper is a good match. Therefore, part of the current tests were run with the model surface covered with 3M 600 grit silicon carbide sandpaper. An electron microscope photograph of that material is shown in Fig. 3. In this picture, we can also see the glue which adheres the sand particles to the paper. The test conditions were such that $k^+ = 5 - 7$. This is in the same range as for the sintered, porous surface.

In order to examine the influence of the porosity directly without further assumption as in the foregoing cases; a perforated titanium plate (see Fig. 5) was also chosen for testing. Since the pores of the perforated titanium plate were made by impinging electronic beams on a smooth, titanium plate, the actual finished plate except for the holes themselves, is rather smooth compared to porous surfaces obtained by other processes. Therefore, the results of the perforated titanium wall can be compared with those of the smooth, solid wall to show the effects of the flow penetration through the perforated plate without any interference of distributed surface roughness.

Further, a solid, rough surface formed of bonded, fine screen called Dynapore and a porous, rough Dynapore wall were tested to make another check on the effect of porosity. The Dynapore plate (see Fig. 5) was formed by diffusion bonding layers of screen together. The rough, solid Dynapore was made by bonding a Dynapore plate with a solid steel sheet underneath and the rough, porous Dynapore was made simply by supporting a Dynapore plate with a coarsely perforated steel sheet underneath. The effects of different roughness patterns for the sandpaper-roughened wall and the Dynapore plate are also manifested in the results.

Besides the Law of the Wall, the turbulence flow field of the boundary layer should also be examined ($\overline{u'^2}$, $\overline{v'^2}$, $\overline{u'v'}$ as a minimum) to aid the development of higher order turbulent transport models.

It is also worth mentioning that documenting the turbulent flow over a porous surface without injection or suction has practical value in its own right. If one is considering a laminar flow control system using suction, the behavior of the flow if the suction system should fail is an important matter. Likewise, if an attempt is also to be made to reduce skin friction or heat transfer by injection, one needs to know the magnitude of any initial increase due to porous surface roughness to be overcome for no or low injection when a porous surface is employed compared to the base line case of a smooth, solid surface.

In summary, the major goal of the present work is to study the effects of small roughness and porosity on turbulent boundary layer behavior. The detailed documentation of turbulent boundary layer flow over porous surfaces without mass transfer can be useful for further extension of the semi-empirical theory to include the phenomenon of mass transfer.

To achieve this goal, six cases were studied in the current experiments:

1) smooth, solid wall
2) sand-roughened, solid wall
3) sintered metal, porous wall
4) perforated titanium wall
5) solid, rough bonded screening wall (Dynapore)
6) porous, rough bonded screening wall (Dynapore)

Measurements of the skin friction directly and the profiles of mean velocity,

axial and normal turbulence intensities and Reynolds stress were made at several axial locations and two freestream velocities, which correspond to dynamic pressures of 12.7 and 17.8 cm. H_2O. (45.1 and 53.3 m/sec.)

EXPERIMENTAL APPARATUS & INSTRUMENTATION

2.1 WIND TUNNEL

The testing was conducted in the Virginia Tech stability wind tunnel. This is a closed-circuit, continuous-flow facility with a 2m. x 2m. test section. The tunnel has the capability of achieving a maximum speed of 67.0 m./sec and Reynolds numbers of the order of 3×10^5 per m. with a low turbulence factor of 1.08. The tests were run at two different freestream velocities corresponding to dynamic pressures of 12.7 and 17.8 cm. H_2O. (45.1 and 53.3 m/sec.)

The tunnel static and total pressures were measured by using a Pitot-static tube*, the dynamic pressure was shown on a Barocel Electronic Manometer, Model 1173*, and the tunnel temperature was measured by using a digital thermometer, Model 1563-83-115-Hk+.

2.2 MODELS

A long axi-symmetric model with a streamlined nose and a cylindrical main body was used. The model is 4.04 m. long and 40.1 cm. in diameter and was mounted on a stand with a streamlined surface surrounding the stand structure (see Fig. 6). The circular cross section of the model was chosen to eliminate any corner effects or three dimensional flows. The large outside diameter of the body was chosen so that possible transverse curvature effects would be minimized by keeping the boundary layer thickness divided by the radius less than about 1:10. The actual values ranged from about 0.075 to 0.1175.

The model consists of four major sections: the nose, the testing area, the pivot and counterweight area, and the conical afterbody.

The 76.2 cm. long nose, shaped by the equation $r = 2.6\, x^{0.33}$ and blended into zero slope at the base, was constructed of Styrofoam and fiberglass. It contains pressure taps along the center line and around the circumference for aligning the model with the flow. The fiberglass was sanded, painted and waxed to a smooth, shiny finish.

The test area was designed to handle several configurations of solid and porous walls. There were three configurations, which includes six cases, tested in the current experiment (see Table II). The first of the three configurations tested had a 1.22m. long, solid wall, aluminum pipe that was machined smooth as shown in Fig. 6. Two test cases were run with this configuration: one was the smooth, solid wall case and the other one was the rough, solid wall case. The rough, solid wall was formed by carefully glueing

*Manufactured by Datametrics
+Manufactured by Instrulab Inc.

a large sheet of 3M 600 grit silicon carbide sandpaper over the smooth, solid wall. A thin "fairing" was formed on the base of the nose, so that there was no step up onto the sandpaper. This configuration had four measurement stations (#1, #2, #3, #4) which were located at 24.1 cm., 48.3 cm., 72.4 cm., and 96.5 cm. from the base of the nose (see Fig. 7).

There was only one test case run with the second configuration, which is the sintered metal, porous wall case*. The method of manufacturing this surface was to take powdered stainless steel, pour into a flat mold, and then heat just to the melting point so the particles fused together. The thickness of the sintered metal, porous wall is 0.3 cm. In the second configuration, the 1.22 m. long, solid wall testing area was replaced by a 0.61 m. long aluminum solid wall section, and a 0.61 cm. long, sintered, stainless-steel, porous wall section as shown in Fig. 8. This configuration had only one measurement station (#4) located at 96.5 cm. from the base of the nose (see Fig. 7).

Three test cases were run with the third configuration: one was the perforated titanium wall+ case and the others were the solid, rough Dynapore** wall and the porous, rough Dynapore wall cases. The thickness of the titanium wall is 0.066 cm., and the diameter of each hole is 0.15 mm. The spacing between holes is approximately 0.63 mm. The thickness of the solid and porous Dynapore walls are 0.145 cm. and 0.132 cm., respectively. In the third configuration, the sintered metal porous wall was replaced by the perforated titanium wall section, then the solid Dynapore wall section, then the porous Dynapore wall section as shown in Fig. 8. There were three measurement stations (#2, #4, #5) located at 72.4 cm., 96.5 cm., and 119.4 cm. from the base of the nose (see Fig. 7).

A typical wall static pressure distribution is presented in Fig. 9. It can be seen that dP/dx in the main test area is very small. The static pressure over the actual measurement section was determined from the Pitot-static probe on the boundary layer rake. The static pressure ahead of that was determined from wall taps. Both showed values very near the tunnel static pressure. We believe the apparent jump shown is not real. Some workers use a criteria of dc_p/dx per cm. less than 0.001 for a maximum 1% error in c_f. Our largest value was 0.0006 at sta. 5.

2.3 INSTRUMENTATION

A. Skin Friction Balance

The skin friction balance used for the direct wall shear measurements consists of a special, highly sensitive crystal strain gauge unit,*** (see Fig. 10), a 25.4 cm. long moment arm which was used to increase the sensitivity.

*Manufactured by Pall Trinity Micro Corporation
+Manufactured and kindly donated by Pratt & Whitney Aircraft Group
**80 x 700 Mesh over 80 x 80 Mesh Manufactured by Ambac, Michigan Dynamics Division, United Technologies
***Manufactured by Kistler Morse Company, Bellevue, Washington

a floating head, and a base mount for controlling the position of the element head in the model. Fig. 10 shows the skin friction balance setup for the second configuration. Two types of element head were used for the test as shown in Fig. 11. For the sand-roughened wall case, the heads were also carefully covered by sandpaper.

For all the test cases, the balance was calibrated in the laboratory and in the model just before testing. The calibration curves agreed well and showed excellent linearity with little or no hysteresis. In all cases, the head was painstakingly aligned flush with the main surface. The gap around the head was selected to be 0.75% of the diameter of the circular head following the suggestions of Ref. 12 to minimize the errors.

The output signal from the strain gauge was sent through a signal filter, model AF-410,+ to cut off the frequency below 0.1 Hz, then displayed on a HP 7100B strip chart recorder.

B. Pitot Rake

The mean velocity profiles in the boundary layer were obtained with a rake of small Pitot tubes (see Fig. 12). The rake was approximately 3.8 cm. high with one static port and 24 total pressure tubes staggered at increased spacing with distance from the wall. The rake was mounted on the model at the same downstream location as the skin friction balance and slightly to one side to prevent damage to the balance.

The output pressures from the Pitot rake were recorded by using a Scanivalve System,* which consists of four components: Scanivalve model D, pressure transducer model 237, power supply model B24-1.2, and electro-mechanical counter model 177004 020. The transducer output was read on a HP 7100B strip chart recorder with microvolt sensitivity ($\pm$ 0.1% full scale). The pressure transducer has the range of $\pm$ 0.25 psid and was calibrated within $\pm$ 0.15% full scale range.

C. Hot-Wire Anemometer

The turbulence profiles were obtained with TSI and DISA Constant Temperature Hot-wire Anemometer System. The Anemometer System used in this work consists of the following components:

1) Constant temperature hot-wire anemometer (TSI Model 1050). This anemometer has a very low noise (0.007% equivalent turbulence intensity) and high frequency response (500 kHz); therefore, it is suitable for high frequency turbulence measurements.
2) Signal linearizer (TSI Model 1052). The voltage output is linearized with the flow velocity by using a linearizer. The convenience of making turbulence measurements is increased when the voltage output is linear with the flow velocity. However, some accuracy is lost when going through any signal conditioning circuit. The advantage and disadvantage of using the linearizer are discussed in Ref. (18).

+Manufactured by Multimetrics Industries
*Manufactured by Scanivalve Inc.

3) Correlator (TSI Model 1015C). To be able to measure the turbulence intensity in two perpendicular directions and their directional correlation with an x-wire probe, we have to know the sum and difference of the output from the two wires. The function of the correlator is to perform these analog computations.
4) Digital integrating voltmeter (TSI Model 1076). Mean quantities of the flow were obtained from this voltmeter. The range of its integrator time constant is from 0.1 to 100 seconds and the voltage output range is from 0.001 to 100 volts.
5) RMS voltmeter (DISA Model 55D35). The RMS voltmeter serves to read the fluctuating quantities of the flow. It has a signal response range from 1 Hz to 400 kHz, integrator time constants from 0.3 to 100 seconds and an accuracy of 0.5% of full scale deflection.

A single wire, DISA 55P14 (5 μm diam. 1.25 mm long), was used for axial turbulence intensity ($\overline{u'^2}$); and an x-wire, TSI 1243 (5 μm diam., 45°, 1 mm spacing), was used for normal turbulence intensity ($\overline{v'^2}$); and Reynolds stress ($\overline{u'v'}$). An automatic traverse was used to move the hot-wire through the boundary layer. The hot-wire probes were all carefully calibrated before and during testing.

EXPERIMENTAL PROCEDURE

All the tests were run at two nominal speeds of 45.1 and 53.3 m/sec (dynamic pressure of 12.7 cm. and 17.8 cm. of H_2O) to give Reynolds numbers of approximately 2.93×10^6 and 3.38×10^6 based on the length to the first station.

Six cases were studied in this work. Each test follows the same procedure as described below:

1) The skin friction balance was calibrated in the model. Data for skin friction were then taken.
2) The pressure distributions were taken.
3) The Pitot rake was then mounted slightly to one side of the floating head, and the mean velocity profiles were obtained.
4) A single-wire probe, DISA 55P14, was mounted on the automatic traverse, and the measurements for axial turbulence intensity profiles were taken.
5) The single-wire probe was replaced by an x-wire probe, TSI 1243, and the measurements for axial turbulence intensity, normal turbulence intensity, and Reynolds stress profiles were obtained.
6) For the perforated titanium wall and the porous Dynapore wall cases, a miniature single-wire probe, DISA 55P11 (5 μm diam.) was mounted inside the model and about 0.159 cm. below the surface to check the flow penetration through the porous surfaces.

DATA REDUCTION & ERROR ANALYSIS

4.1 DATA REDUCTION

A. Skin Friction

The calibration curve of the skin friction balance is obtained by using

the setup as shown in Fig. 13. The thread has been straightened before it was used for the calibration. From the force balance, we found

$$F_c = \frac{W}{\tan\beta - \tan\alpha} \tag{2}$$

where F_c is the axial force acting on the floating head and W is the weight.

The calibration curves are linear and the error is less than $\pm$ 2% if the total axial force acting on the floating head is not over 1.0 gram which was true for most of our cases.

From Eq. (3), the wall shear could be calculated.

$$\tau_w = \frac{F_a}{A} \tag{3}$$

where F_a, the total force acting on the surface of the floating head during the runs, is obtained by interpolation from the calibration curve and A is the surface area of the floating head. Then, the skin friction coefficient was obtained Eq. (4).

$$C_f = \frac{\tau_w}{1/2\rho_\infty U_\infty 2} \tag{4}$$

Finally, the skin friction velocity was calculated from Eq. (5).

$$U_* = \sqrt{\tau_w/\rho_\infty} \tag{5}$$

B. Mean Velocity

The mean velocity was obtained from the Bernoulli's equation

$$P_o = P_s + 1/2\rho \quad U^2 \tag{6}$$

where the total pressure P_o and the static pressure P_s were obtained from the Pitot rake during the same run. Any explicit effect of turbulence on these mean measurements was neglected.

C. Turbulence Quantities

The axial turbulence intensity could be obtained both from the single-wire probe data from Eq. (7) or from the x-wire probe data from Eq. (8). However, the data obtained by the single-wire probe are generally considered to be more accurate than those by the x-wire probe. The normal turbulence intensity

and Reynolds stress were obtained by Eq. (9) and Eq. (10).

$$\sqrt{\frac{\overline{u'^2}}{U}} = \sqrt{\frac{\overline{e^2}}{\overline{E}}} \tag{7}$$

$$\sqrt{\frac{\overline{u'^2}}{U}} = \sqrt{\frac{(e_1 + e_2)^2}{(\overline{E_1 + E_2})}} \tag{8}$$

$$\sqrt{\frac{\overline{v'^2}}{U}} = \left(\frac{1 + K^2}{1 - 3K^2 + 4K^4}\right)^{1/2} \sqrt{\frac{\overline{(e_2 - e_1)^2}}{(\overline{E_1 + E_2})}} \tag{9}$$

$$\frac{\overline{u'v'}}{U^2} = \left(\frac{1 + K^2}{1 - K^2}\right) \frac{\overline{e_2^2} - \overline{e_1^2}}{(\overline{E_1 + E_2})^2} \tag{10}$$

The derivations of the above equations are detailed in Ref. 13. The above quantities could also be normalized by the edge velocity or the skin friction velocity instead of the local mean velocity through some simple algebraic operations.

4.2 ERROR ANALYSIS

The following analysis consists of calculating the maximum errors in the measured and computed data.

A. Vertical Distance

The vertical distance (Y) of each individual Pitot tube of the boundary layer rake is measured by an optical traveling microscope. The accuracy is within $\pm$ 0.00054 cm. or $Y^+ \pm 0.35$.

The automatic traverse used for moving the hot-wire probes in the boundary layer can give a minimum increment of 0.1 cm. The maximum error from calibration is estimated to be + 1%. The maximum estimated error for the lowest position of the hot-wire probe is $\pm$ 0.01 cm. Therefore, the maximum combined error in the determination of the probe position in the boundary layer could be $\pm$ 0.011 cm. which corresponds to an error of $\pm$ 5% in Y/δ^*.

B. Mean Velocity

The mean velocity profile in the boundary layer is obtained by using

the Pitot rake. Since the pressure transducer was calibrated within ± 0.15% of full scale deflection and the pressure was recorded on a strip chart recorder with an accuracy of ± 0.1% for full scale deflection, it is estimated that the pressure measurements are within ± 0.5% of the true value. This includes the error due to reading the strip chart recorder because of small variation from the mean value due to the likely oscillations within the boundary layer and tunnel vibration. Therefore, the maximum error of the mean velocity calculated from the pressure difference is less than 1%.

The mean velocity profiles were satisfactory except for the results from the Pitot tube which sits right in the body surface. Although, the tip of that particular Pitot tube had been flattened, as suggested by many researchers, the data point on the Wall Law plot was still always higher than it should be. Some suggested corrections for near wall measurements were applied to our results for that point; but no substantial improvement was obtained. Therefore, the first data point on the Wall Law plot was ignored.

C. Skin Friction

The most difficult part of the experiments is to obtain consistent and reliable skin friction results. The errors in the skin friction results are due to calibration, misalignment and uncertainty in reading the voltage output on the strip chart recorder.

The calibration indicated that the curves were linear and repeatable. Thus, the maximum error is ± 2% if the force acting on the head is less than 1.0 gram which is true for most of our tests.

The slight misalignment of the element head is unavoidable for a cylindrical surface, although the contour of the element heads were carefully made to match the body surface and the 3-D positioning device was also carefully designed to reduce the possibilities of misalignment. Control tests were done by lowering and raising the element head from its neutral position to see how the slight misalignment will affect the results. It is estimated that the maximum error will not be over ± 2.5% if the element head is carefully aligned.

The error due to the uncertainty in reading the strip chart recorder was found to be less than ± 1.5%.

Combining these errors gives a resultant maximum deviation of ± 6% in the measured value of the skin friction. The actual apparent error obtained for our smooth wall tests was approximately ± 2% in comparison with well-accepted results.

D. Turbulence Quantities

All the turbulence quantities were measured over the center of the element head. The gap around the heads and the possible slight misalignment of the element head may cause some errors in the measurements; however, these errors had been minimized by limiting the gap size and carefully aligning the element heads to match the contour of the body surface. This error has been estimated to be within ± 1%.

The major errors in the hot-wire results are due to the calibration, the temperature change during the test runs, and the uncertainty in reading the output through the voltmeters because of the oscillations of the flow in the boundary layer. Errors due to calibration were found to be less than ± 1% mainly in adjusting the span for the linearizer. Errors in reading the output data through the DC voltmeter and RMS voltmeter are found to be less than ± 1% and ± 0.5% respectively. However, the errors due to the temperature change during the test runs could be serious; therefore, the measurements were generally started after the tunnel was running for a short while when the temperature becomes stable (± 3°C). Also, the hot-wires were calibrated more often if there had been a significant temperature change. For the single-wire measurements, the error is not high because the test runs could be completed in a short time and the temperature change during this period is small. It is estimated to be less than ± 1.5% for both DC and RMS outputs. For x-wire measurements, the maximum error are higher and are estimated to be ± 3% for both DC and RMS outputs.

From the equation in section 4.1 and the errors described above, we can estimate the maximum errors for axial and normal turbulence intensities, and Reynolds stress to be roughly ± 3%, ± 5% and 11% respectively. These figures are consistent with what was found for our smooth wall results.

RESULTS

5.1 SMOOTH, SOLID WALL RESULTS

The smooth, solid wall tests were run primarily to document the adequacy of the instrumentation and procedures. These data also serve as "baselines" for comparison with the main test results.

Some mean velocity profiles obtained with the boundary layer rake are shown in Fig. 14a and b and 15 in terms of the conventional Wall Law plots and Defect Law plots (using Y/δ^*, since δ^* can be more precisely determined). The good agreement with Clauser's suggestion (Eq. (11)) for the logarithmic portion of the turbulent boundary layer can be seen on these plots. This implies accurate mean velocity profile and skin friction measurements.

$$\frac{U}{U_*} = 5.6 \log \frac{YU_*}{\nu} + 4.9 \qquad (11)$$

$$\frac{U_e - U}{U_*} = - 2.44 \ln \frac{Y}{\delta} + 2.5 \qquad (12)$$

$$\frac{U_e - U}{U_*} = 9.6 \left(1 - \frac{Y}{\delta}\right)^2 \qquad (13)$$

where $\delta \simeq 8\delta^*$.

Also, good agreement with suitably modified Clauser (Eq. (12)) and Hama (Eq. (13)) formulas (Ref. 14) for the inner and outer region of the turbulent

boundary layer was found on the Defect Law plots. They were modified to correspond to δ^* rather than δ. The data obtained at two different free stream velocities and four different axial locations showed excellent consistency.

The local skin friction coefficients are listed in Table IV along with some previous results in the same apparatus. These data, except for the new results at Sta. #4 at 12.7 cm. H_2O, agree within $\pm$ 1% with the well-established simple law (Ref. (15)):

$$C_f = 0.0128 \quad (Re_{\delta^*})^{-1/6} \tag{14}$$

Typical axial turbulence intensity plots are shown in Figs. 16 and 17. The data agreed very well with Klebanoff's classical results (Ref. (16)) for a smooth flat plate except near the outer edge of the layer. Comparisons not included here showed that data obtained with the x-wire were virtually identical to those obtained with the straight wire.

The axial and normal turbulence intensities obtained by the x-wire are compared with Klebanoff's results in Fig. 18 showing excellent agreement. Fig. 19 shows the normal turbulence intensity profiles at three different axial locations.

Fig. 20 shows that Reynolds stress profiles obtained by the x-wire are a little lower than Klebanoff's results. It should be noted that Klebanoff did not measure wall shear independently. He obtained values of $\overline{u'v'}$ up to the wall by extrapolation, thus forcing a value of unity at y = 0. Fig. 21 shows similar trends for the Reynolds stress profiles obtained at different locations with wall shear measured independently.

5.2 SAND-ROUGHENED, SOLID WALL RESULTS

These tests were run with the surface covered with 3M 600 grit silicon carbide sandpaper. The roughness pattern can be seen to be very uniform on the electron microscope photograph in Fig. 3. If one takes 1/600 in. as the definition of the roughness size, then the k^+ is about 5 for the q = 12.7 cm. H_2O test.

Law of the Wall plots for all stations on the sand-roughened and smooth walls are shown in Figs. 22a, b, c and d. It can be seen that the logarithmic portion of the Wall Law does shift downward slightly by an amount $\Delta U^* \simeq 1.0$ at Station 1 and 2, but it does not shift at Station 3 and shifts upward by an amount $\Delta U^+ \simeq 1.0$ at Station 4. Previous results for uniform sand grain roughness (Ref. 11) indicate that the downward shift is negligible in this k^+ range. It could perhaps be concluded that the shifts observed are within our error range, although they do show a consistent trend from station to station and test to test. This matter may well deserve further careful study.

The skin friction coefficients listed in Table III indicate a clear increase of the wall shear at all stations even for the roughness corresponding to this low k^+ range. The increase is about 13% $\sim$ 21% for q = 12.7 cm. H_2O test and 21% $\sim$ 34% for q = 17.8 cm. H_2O test. These results are also in close

agreement ($\pm$ 2%) with the data for uniform sand on flat plates deduced from pipe flow measurements (Ref. (17)).

Defect Law plots for sand-roughened and smooth walls are shown in Fig. 23. It can be seen that the velocity Defect Law is not affected by the roughness in this low range.

In Fig. 24, we show some comparisons of the axial and normal turbulence intensity profiles for rough and smooth walls. The effect is largest for the normal turbulence intensity. It is clear that even for this low k^+, sand roughness has a measurable effect on the turbulence field throughout the boundary layer.

The Reynolds stress profiles for rough and smooth walls are compared in the usual way as shown in Fig. 25(a). Since there are variations in U_* between the two cases, we believe it may be more enlightening to consider the results as $\overline{u'v'}/U^2$, where U is the local mean velocity, as shown in Fig. 25(b). In both cases, the rough wall results are higher as expected.

5.3 SINTERED METAL, POROUS WALL RESULTS

The sintered metal, porous wall results, without injection or suction serve to display the effects of porosity and small distributed roughness that accompany most of the porous surfaces. The porous material used for the present study was made from powdered stainless steel. The particles are not spherical originally, and they are distorted somewhat in the sintereing process. If an average dimension of 40 microns is taken as the definition of the roughness size, then for the test at q = 12.7 cm. H_2O, the k^+ is about 5. The thickness of the sintered metal, porous wall is 0.3 cm.

The sintered metal, porous wall and the sand-roughned, solid wall are in the same nominal roughness range of $k^+ \simeq 5$ for the q = 12.7 cm. H_2O test under the simple assumptions about the relationship of a non-uniform sintered metal, porous surface to uniform sand-roughness on a solid surface. Therefore, the comparison of these cases will indicate the effect of porosity alone.

The Law of the Wall plot in Fig. 26 shows that the downward shift of U^+ for the sintered metal, porous wall is much greater than that for a sand-roughened, solid wall in the same k^+ range. Table III shows that the skin friction coefficients are also increased more sharply for the sintered metal, porous wall than those for the sand-roughened, solid wall. It could be concluded that the porosity does contribute to the increase of skin friction and downward shift of the logarithmic portion of the Wall Law. This seems to be reasonable because the normal turbulence component will not die out on the porous surface.

Figs. 27a and b, and 28 indicate that the axial turbulence intensity, normal turbulence intensity and Reynolds stress are all somewhat higher for the sintered metal, porous wall than those for the sand-roughened, solid wall. Of course, all the turbulence quantities for the two "rough" wall cases are higher than those for the smooth, solid wall.

In order to compare the results between the porous rough wall and solid rough wall not only at the same k but also at the same k^+ ($= \frac{U_* k}{\nu}$), a comparison was made between the data for the sintered metal, porous wall with a q = 12.7 cm.

H_2O at Station 4 and for the sand-roughened, solid wall with a q = 17.8 cm. H_2O at Station 3 where the values of U_* are very nearly equal, and thus k^+ is closely matched for the two cases. Fig. 29 shows that the downward shift of U^+ for the sintered metal, porous wall is greater than that for the sand-roughened, solid wall. Figs. 30a and b and 31 indicate that all the turbulence quantities are higher for the sintered metal, porous wall case.

5.4 PERFORATED TITANIUM WALL RESULTS

Since the surface of the perforated titanium wall is, except for the isolated holes, rather smooth, the influence of porosity on a turbulent boundary layer can be seen directly by comparing the results between the perforated titanium wall and the smooth, solid wall. There is no need to make any assumption regarding roughness size and character as in the comparison between the sintered metal, porous wall and the sand-roughened, solid wall results.

The skin friction coefficients listed in Table III show a significant increase for the perforated titanium wall compared to the smooth, solid wall. The increase is about 30%. The skin friction coefficients obtained at Station 3 have been discarded because of experimental difficulties. It can also be seen from Table III that the increase of skin friction coefficients for the sintered metal, porous wall is about 20% over the perforated titanium wall. This is close to the skin friction coefficient increase for the sand-roughened, solid wall compared to the smooth wall. These results indicate that both small roughness and porosity contribute to an increase of skin friction of approximately 20% and 30% above the smooth wall data, respectively.

The typical Law of the Wall plot of Fig. 32 indicates that the downward shift of the logarithmic portion of the Wall Law is about $3.0 \sim 4.0$ due to the presence of porosity on a smooth surface. Fig. 32 also shows that there is no appreciable further downward shift of the logarithmic region of the Wall Law due to the presence of the small roughness of the sintered surface.

Fig. 33 shows that both small roughness and porosity will increase the axial turbulence intensity slightly. Fig. 34 shows the same trend as Fig. 33 where the normal turbulence intensity is increased slightly by the presence of small roughness and porosity. The increase of axial and normal turbulence intensities is about $1 \sim 2\%$ based on edge velocity. It was consistently found that the turbulence intensities decayed more rapidly across the layer for flow over the perforated titanium surfaces. Perhaps this is a result of the regular, open-spaced porosity pattern. Fig. 35 shows that Reynolds stress is also increased, and the increase can reach to 100% in the near wall region.

Theoretically, the effect of porosity is due to the normal turbulence component penetrating the porous surface if there is no pressure gradient along the body surface. To check the existence of turbulence penetration through the surface, a very sensitive miniature single-wire probe was mounted beneath the perforated titanium wall to about 0.159 cm. The results in Fig. 36 indicate that the velocity fluctuation gets higher, but the mean velocity remains almost zero with increasing wind tunnel speed. The slight variation in mean velocity could be the result of temperature change in the wind tunnel during testing.

5.5 BONDED SCREENING WALL RESULTS

The screen mesh type of roughness of the solid, rough Dynapore wall has

a different nature than the particle type of roughness such as the sand-roughened, solid wall and sintered metal, porous wall. However, the characterization of this very fine screen mesh type of roughness is just as difficult as the particle type of roughness. For simplicity, if we take the diameter of the screen wire of the Dynapore sheet, which is approximately 0.0076 cm. measured from Fig. 5, as the representative size dimension of this rough surface, then the k^+ is approximately 9 for the q = 12.7 cm. H_2O test.

5.5.1 SOLID, BONDED SCREENING WALL RESULTS

The "solid", Dynapore surface was made by bonding a solid sheet underneath a Dynapore sheet. Since the Dynapore sheet is very flimsy, it is difficult to cut clean holes for the floating heads. The edges of the holes and the nearby surface were badly damaged on the first Dynapore sheet we received. Also, inserting and glueing the tube around the head (see Fig. 10) tend to distort the surface of the cylinder. Therefore, we could not get good skin friction measurements with this surface except for the last station where the damage was minor. As an alternative, skin friction coefficients calculated from the Momentum Integral Method are also listed in Table III. Profiles were measured at additional stations.

The effect of the screen mesh type of roughness can be shown directly by comparing the results between the solid, rough Dynapore wall and the smooth, solid wall. A Wall Law plot is shown in Fig. 37. It can be seen that the logarithmic portion of the Wall Law is shifted downward by an amount $\Delta U^+ \simeq 1.0$ compared to the smooth wall results. That downward shift is a little higher than that produced by the small sand grain roughness.

Fig. 38 shows that the axial turbulence intensity on the solid Dynapore wall is higher than that of the smooth, solid wall. Also, the axial turbulence intensity increases more rapidly when one gets closer to the wall.

Figs. 39 and 40 indicate that there are almost no increases in both the normal turbulence intensity and Reynolds stress for the solid Dynapore wall case. This is surprising because the surface roughness should increase the mixing process in the boundary layer.

5.5.2 POROUS BONDED SCREENING WALL RESULTS

The porous Dynapore was made by supporting a Dynapore sheet with a thin perforated steel plate underneath. The thickness of the perforated steel plate is 0.081 cm. and it has 16 small holes (d = 0.159 cm.) per square cm.. Although the Dynapore material is flimsy, the damage to the surface due to the cutting process was found to be less for this piece. It was observed that there is a small hill near the front edge of measuring station 4 on the surface of the cylindrical body. We took data both when the element head was aligned with the top of the hill and then aligned with the smooth part of the body surface. The final skin friction coefficient in Table III is the average value from these two measurements.

Since the roughness on both the solid and porous Dynapore wall is exactly the same, the comparison of these two cases can adequately show the influences of porosity on the boundary layer behavior directly.

The skin friction data in Table III show they are about 30 ∿ 40% higher for the porous than for the solid Dynapore wall cases. That is close to the increase of skin friction for the sintered metal porous wall over the sand-roughened solid wall. Also, the increase of skin friction coefficient for the porous Dynapore wall over the smooth wall is about 60%, which is higher than the corresponding increase for a sintered metal porous surface.

The Wall Law plots of Figs. 41 and 42 show that the downward shift of the logarithmic portion of the Wall Law is about 4.5 for the porous Dynapore wall which is also a little higher than the corresponding downward shift for the sintered metal porous wall. Fig. 42 shows that the downward shift of the logarithmic region of the Wall Law for the porous Dynapore wall is much greater than that for the solid Dynapore wall.

From Fig. 43, it can be seen that the axial turbulence intensity of the porous Dynapore wall is about 1% (based on edge velocity) higher than that of the solid Dynapore wall. However, the axial turbulence intensity of both the porous and solid Dynapore walls is higher than that of the smooth wall. It is also observed that the increase of the axial turbulence intensity became more rapid closer to the wall.

Fig. 44 shows that the normal turbulence intensity is about 2% (based on edge velocity)higher for the porous Dynapore wall than that for the solid Dynapore wall. It also can be noted that the increase of normal turbulence intensity becomes more rapid closer to the wall. The Reynolds stress profiles in Fig. 45 indicates the same trend as the axial and normal turbulence intensity profiles, but the maximum increase of Reynolds stress can be as high as 100% (based on local mean velocity) in the near wall region.

As we did for the perforated titanium wall, the penetration of the turbulence through the porous Dynapore was detected by a single-wire probe under the porous Dynapore wall. It can be seen from Fig. 46 that there is no mean flow but measurable turbulence passing through the porous surface.

5.6 PRESSURE DROP THROUGH THE POROUS MATERIALS

In order to aid in understanding the behavior observed with the three different porous materials used, a measure of their "porosity" was obtained by determining the pressure drop through each material as a function of volume flow rate (or average normal injection velocity). The results are given in Fig. No. 47 where the wide variation for the different materials can be noted.

CONCLUDING REMARKS

The turbulent boundary layer over a smooth wall, a rough, solid wall and porous, rough and "smooth" walls was studied. The goal was to investigate the influences of small roughness ($k^+ = 5 - 10$) and porosity independently and their combined effects on turbulent boundary layer behavior. Here we have concentrated on small roughness because of its importance in practical engineering applications. The effect of porosity due to the existence of the penetration of turbulence through porous surfaces has been confirmed.

For the smooth, solid wall case, accurate results were obtained for the Law of the Wall, the Defect Law, the axial and normal turbulence intensities, and the Reynolds stress when compared with well-established data.

Two solid, rough wall cases were studied in this work. One was the sand-roughened, solid wall which had a sand grain type of roughness on the surface with an average $k^+ = 5$ for the tests. The second was the solid, rough Dynapore wall which has a screen mesh type of roughness on the surface. For both cases, the effect of small roughness is to shift the logarithmic portion of the Wall Law by a small to negligible amount. However, the increase in the skin friction values is not negligible; the increase is about 20% $\sim$ 30% above the smooth wall value. It is observed that small roughness does not affect the Defect Law. The axial and normal turbulence intensities are increased slightly. The increase is about 1% based on the edge velocity, and the increase of Reynolds stress is somewhat higher.

Three different porous wall cases were studied, namely a sintered metal, porous wall; a perforated titanium wall and a porous Dynapore wall. The effect of porosity can be shown when comparing the sintered metal, porous wall results to the sand-roughened, solid wall results. Although the character of the roughness for these two cases is different, the average k^+ is in the same range of 5 $\sim$ 7. To see the effect of porosity directly without any interference of different surface roughness patterns, one can compare the results between the "smooth" perforated titanium wall and the smooth, solid wall, or between the porous and solid Dynapore walls, where the roughness patterns of these two surfaces are exactly the same. The comparisons reveal that the effect of porosity is to shift the logarithmic region of the Wall Law downward by an amount $\Delta U^+ = 3 \sim 4$ from the solid wall results and to increase the skin friction values by about 30% $\sim$ 40%. The axial and normal turbulence intensities and Reynolds stress are increased, and the increase becomes more rapid when one gets closer to the wall.

The combined effects of small roughness and porosity can be seen by comparing the results between the sintered metal, porous wall and the smooth, solid wall or between the porous, rough Dynapore wall and the smooth, solid wall. The downward shift of the logarithmic region of the Wall Law and the increase of the skin friction value by the combined effects of small roughness and porosity is found to be roughly the sum of their individual effects. However, the turbulence quantities do not show the same trend clearly, although all the turbulence quantities are increased by the small roughness and porosity.

All these results demonstrate that a porous, rough wall simply does not influence the boundary layer in the same way as a solid, rough wall. Therefore, turbulent boundary layer models for cases with injection or suction must include surface roughness and porosity effects; however, these effects cannot simply be interpolated from the results for a sand-roughened, solid wall.

REFERENCES

1. Baronti, D., Fox H., and Soll, D., "The Turbulence Boundary Layer with Mass Transfer," Astronautica Acta, 1964.

2. Jeromin, L.O.F., "The Status of Research in Turbulent Boundary Layers with Fluid Injection," Progress in Aerospace Science, Vol. 10, Pergamon Press, New York, 1970.

3. Coles, D., "A Survey of Turbulent Boundary Layers with Mass Transfer," Rand Corp., Rept. P-4697, Sept. 1971.

4. Kays, W. M. and Moffat, R. J., "The Behavior of Transpired Turbulent Boundary Layers," Studies in Convection, Vol. 1, edited by B. Launder, Academic Press, New York, 1975.

5. Squires, L. C., "Turbulent Boundary Layers with Suction or Blowing," AFOSR-HTTM-Stanford Conference on Complex Turbulent Flows, Sept. 1980.

6. Stevenson, T. N., "A Law of the Wall for Turbulent Boundary Layers with Suction or Injection," Cranfield College of Aeronautics, Rept. 166, Cranfield, England, July 1963.

7. Tennekes, H., "Similarity Laws for Turbulent Boundary Layers with Suction and Injection," Journal of Fluid Mechanics, Vol. 21, 1965.

8. Simpson, R. L., "The Turbulent Boundary Layer on a Porous Wall," Ph.D. Thesis, Stanford University, 1968.

9. Schetz, J. A. and Nerney, B., "Turbulent Boundary Layer with Injection and Surface Roughness," AIAA Journal, Vol. 15, No. 9, Sept. 1977.

10. Huffman, G. D., Zimmerman, D. R., and Bennett, W. A., "The Effect of Free-Stream Turbulence Level on Turbulent Boundary Layer Behavior," AGARD Report AG-164, North Atlantic Treaty Organization.

11. Clauser, F. H., "The Turbulent Boundary Layer," Advances in Applied Mechanics, Vol. 4, Academic Press, London, 1956, pp. 1-51.

12. Tcheng, P., "Development of a Servo Transducer for Direct Skin-Friction Measurement," Dept. of Mechanical Engineering, Old Dominion University, July, 1979.

13. Kong, F. Y., "Effects of Hot-Wire Probe Misalignment on Turbulence Measurements," M.S. Thesis, Aerospace and Ocean Engineering Department, VPI & SU, 1979.

14. Hinze, J. O., Turbulence, McGraw-Hill Inc., 1959.

15. White, F. M., Viscous Fluid Flow, McGraw-Hill, Inc., 1974.

16. Klebanoff, D. S., "Characteristics of Turbulence in a Boundary Layer with Zero Pressure Gradient," NACA Report 1247, 1955.

17. Schlichting, H., Boundary Layer Theory, McGraw-Hill, Inc., 1968.

18. Naot, P. and Kreith, F., "On the Penetration of Turbulence Through Perforated Flat Plates," Int. J. of Heat Mass Transfer, Vol. 23, p. 566-568, 1979.

19. Bradshaw, P. and Unsworth, K., "An Improved Fortran Program for the Bradshaw-Ferriss-Atwell Method of Calculating Turbulent Shear Layers," Aero Report 74-02, Imperial College of Science and Technology, Feb. 1974.

20. Schetz, J. A., Favin, S., and Billig, F. S., "Analysis of Flow in the HWADM Combustor," Progress Report, Applied Physics Laboratory, The Johns Hopkins University, 1980.

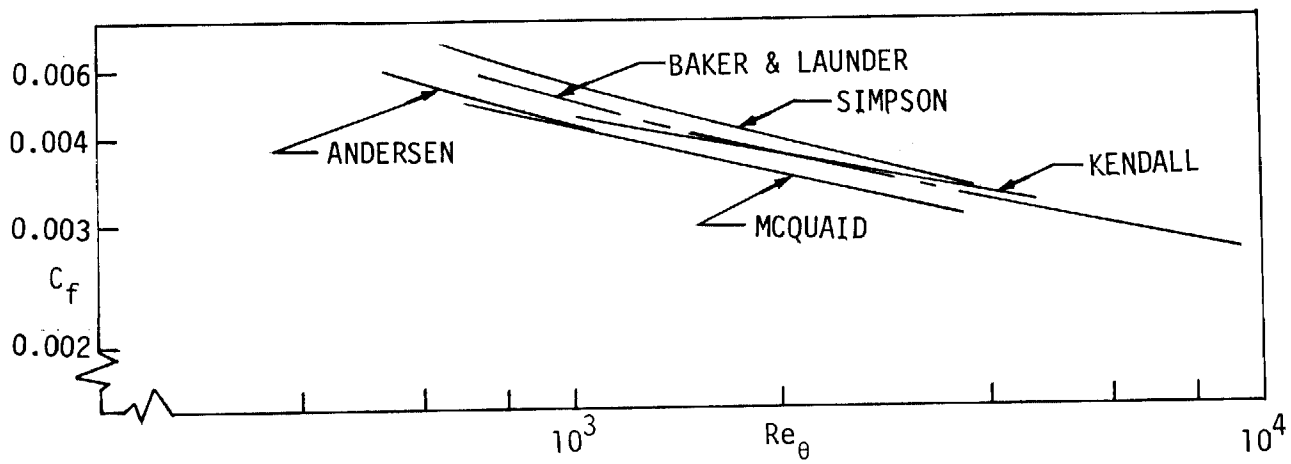

Fig. 1. Comparison of prior experimental (not directly measured) results for skin friction on porous surfaces without injection or suction from Ref. (5).

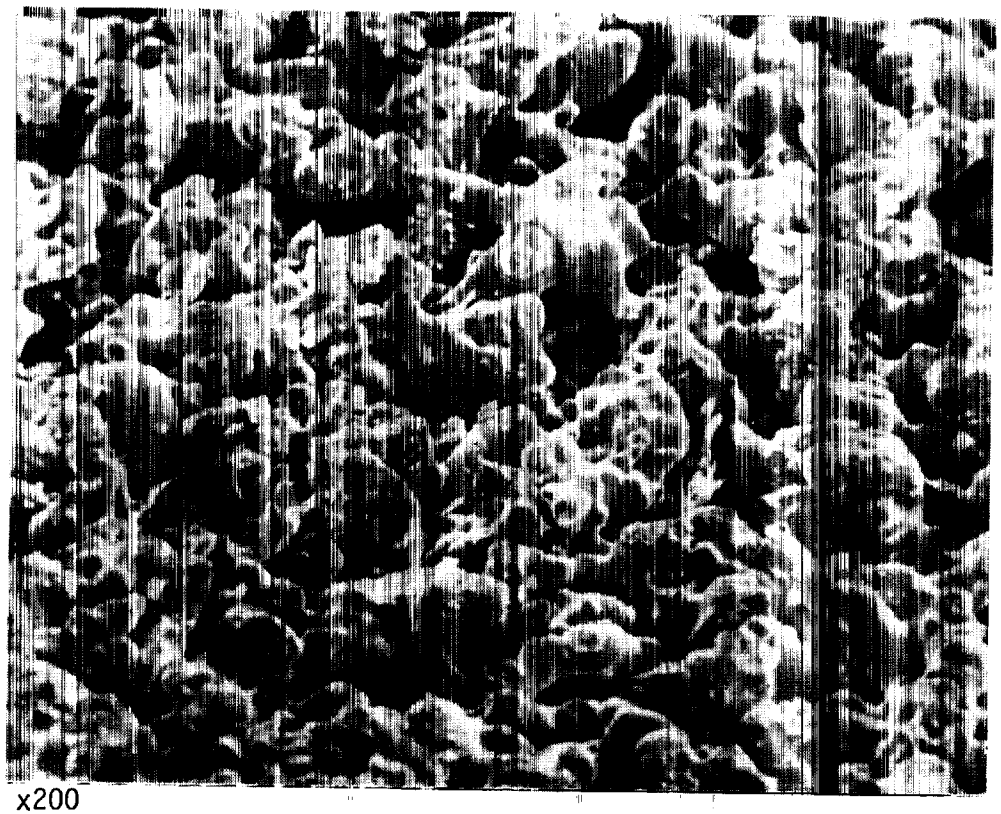

Fig. 2. Electron microscope photograph of the sintered metal, porous surface used in the experiments.

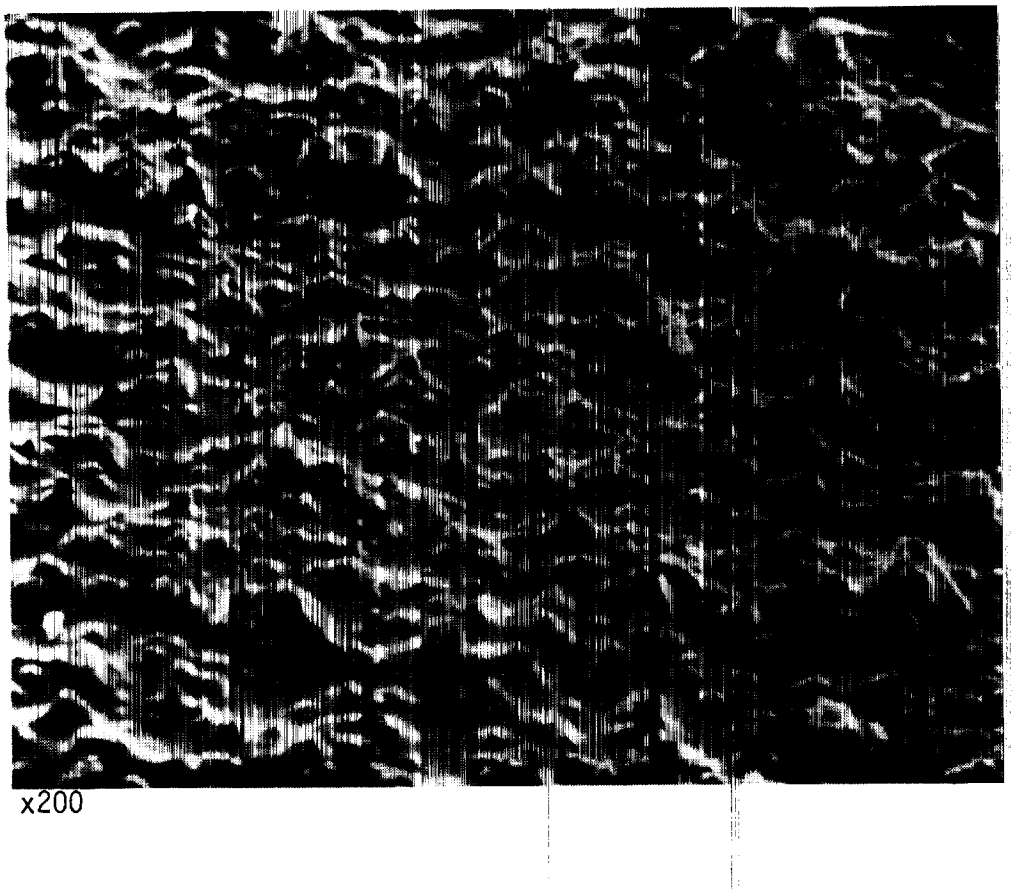

Fig. 3. Electron microscope photograph of 3M 600 grit silicon carbide sandpaper used in the experiments.

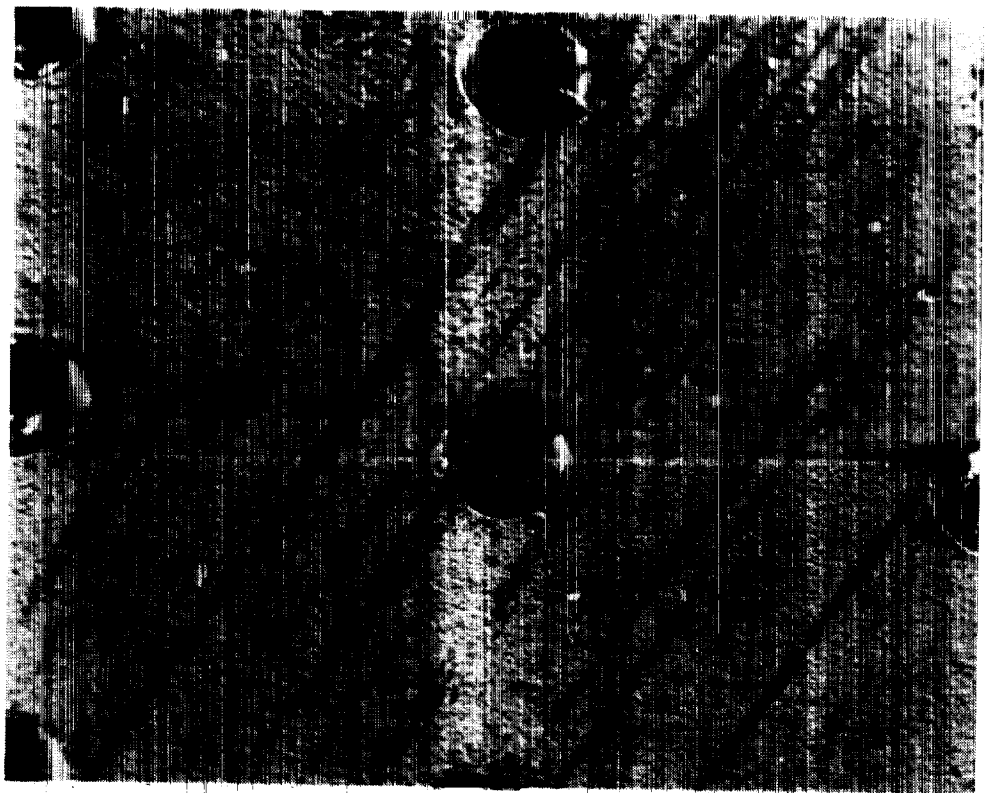

Fig. 4. Electron microscope photograph of the perforated titanium sheet used in the experiments.

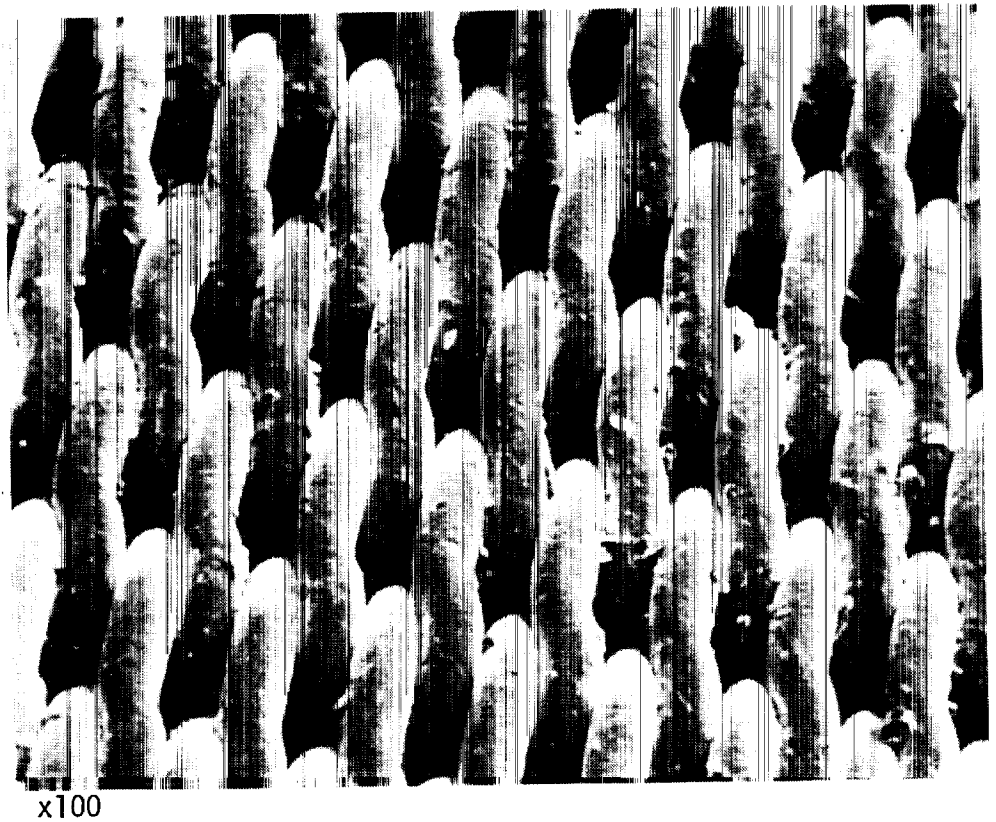

Fig. 5. Electron microscope photograph of the Dynapore sheet used in the experiments.

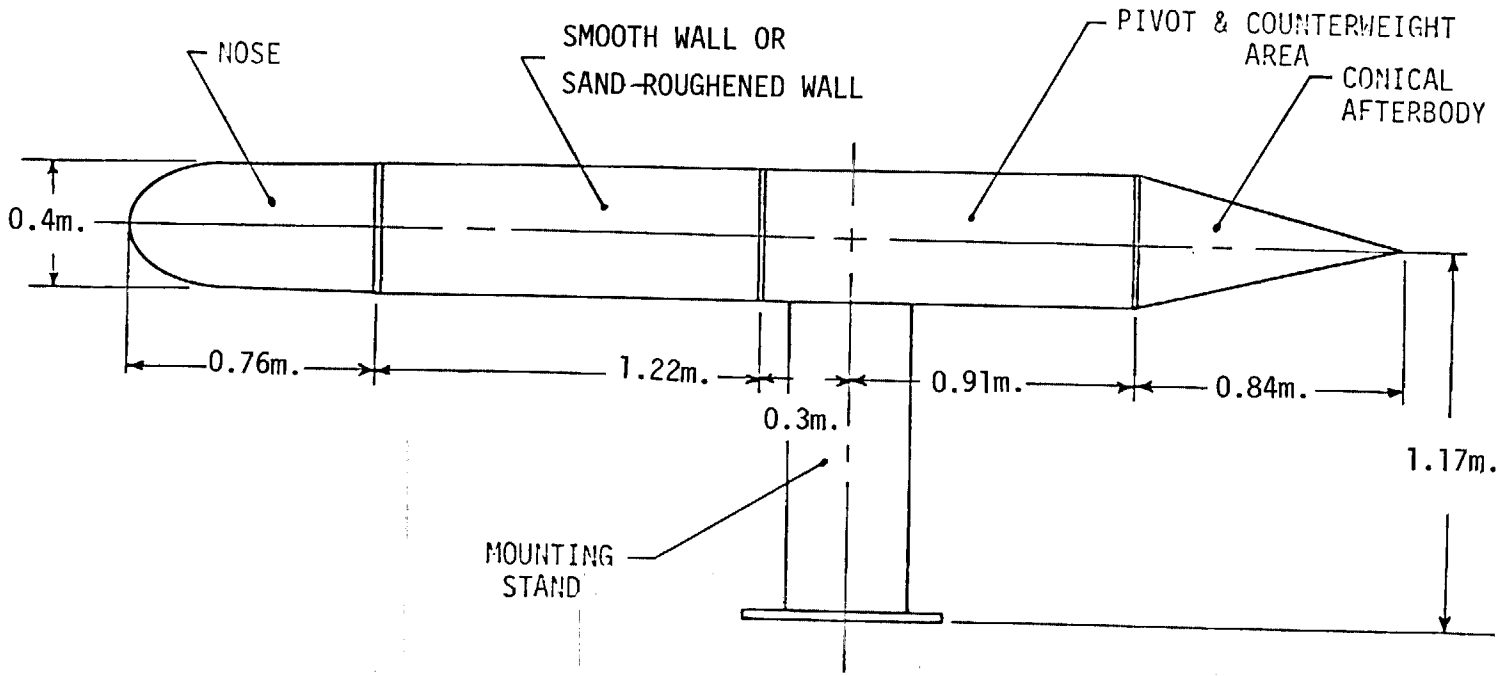

Fig. 6. Axisymmetric wind tunnel model for configuration 1.

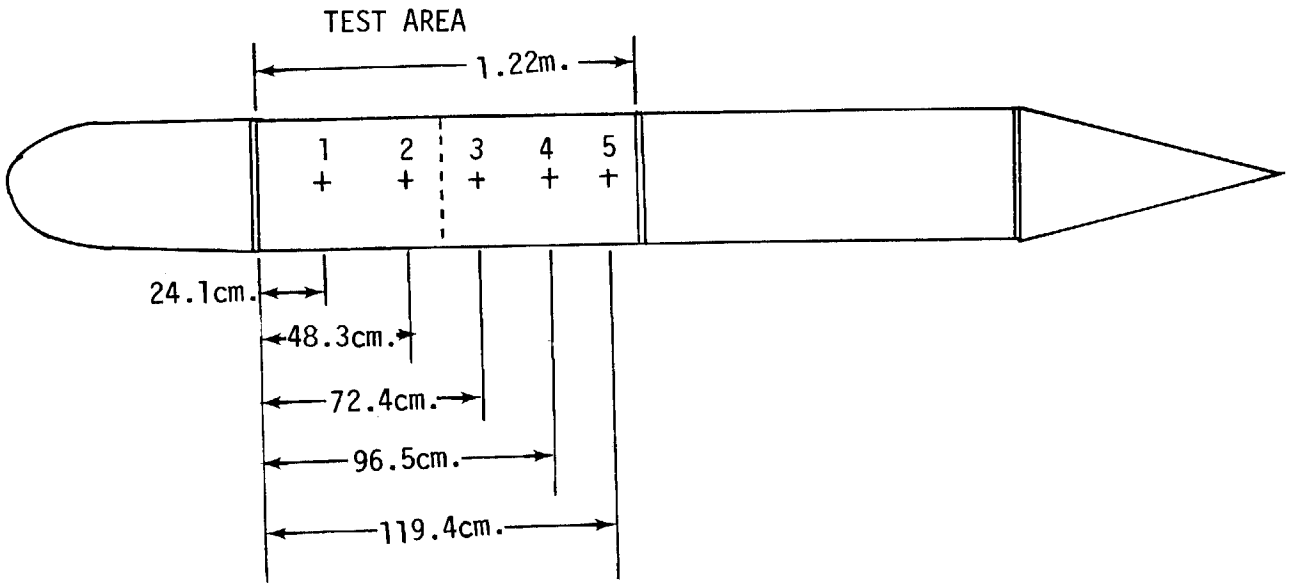

Fig. 7. Measurement station numbers and locations for all cases.

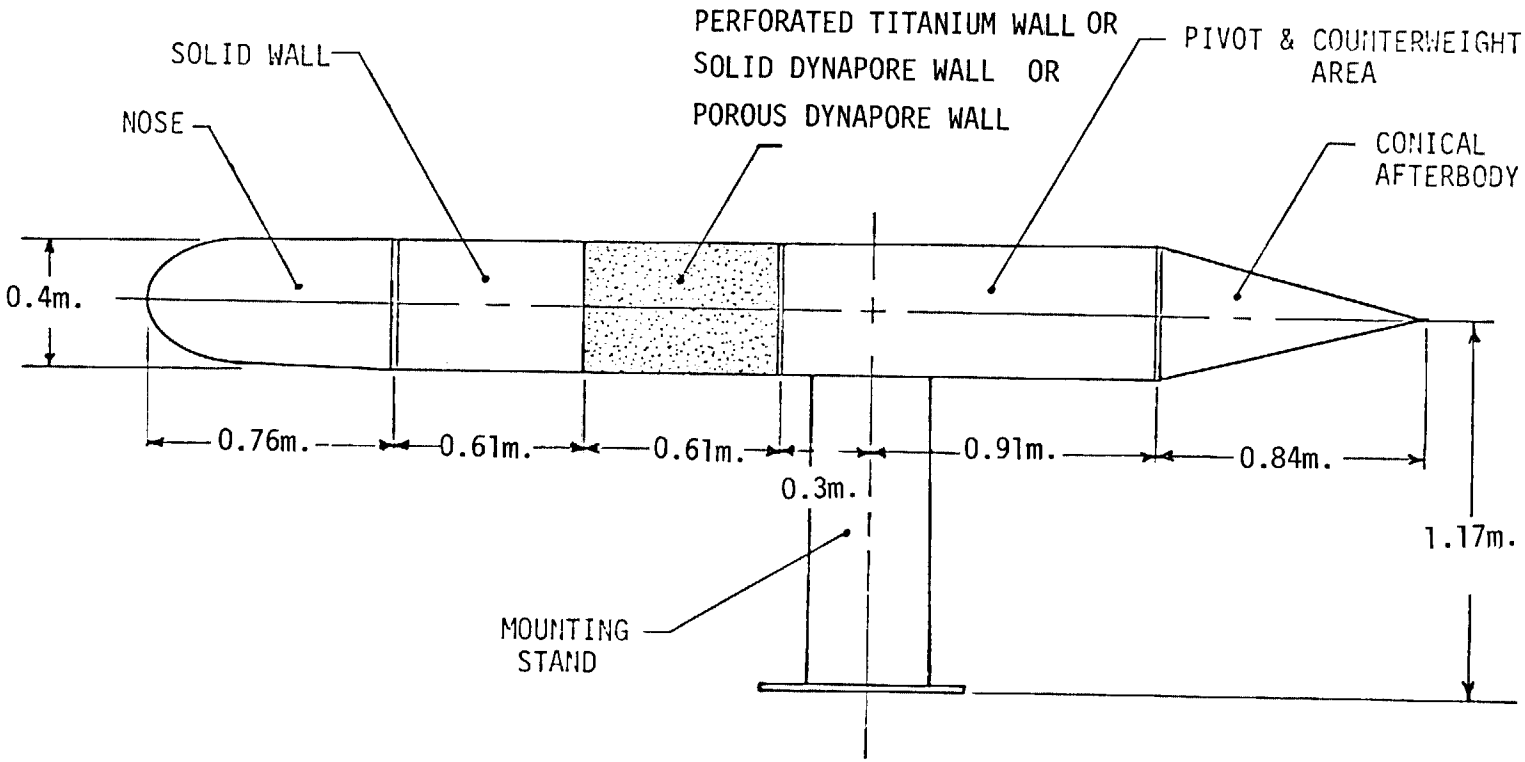

Fig. 8. Axisymmetric wind tunnel model for configuration 3.

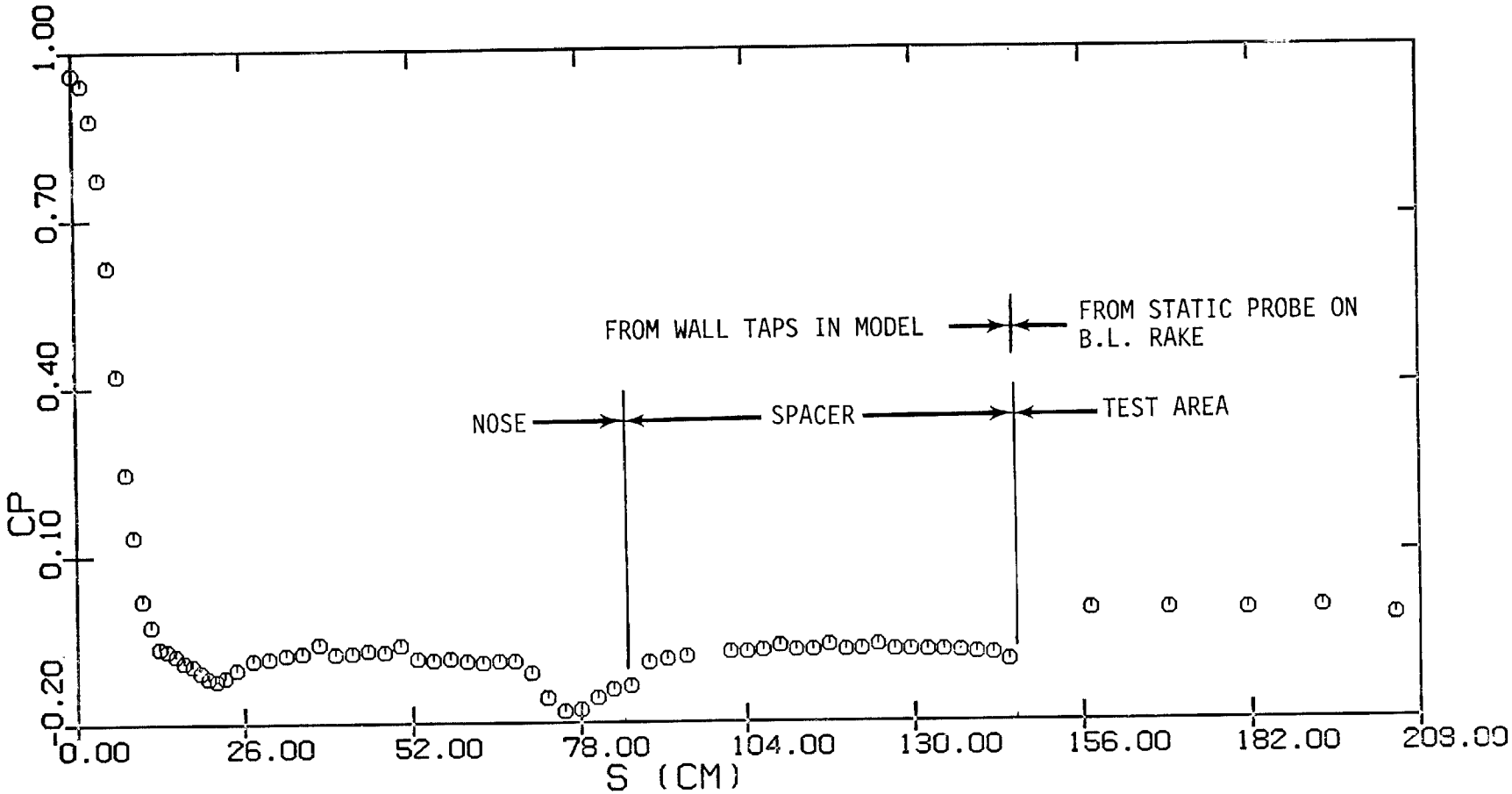

Fig. 9. Pressure Distribution along the Body

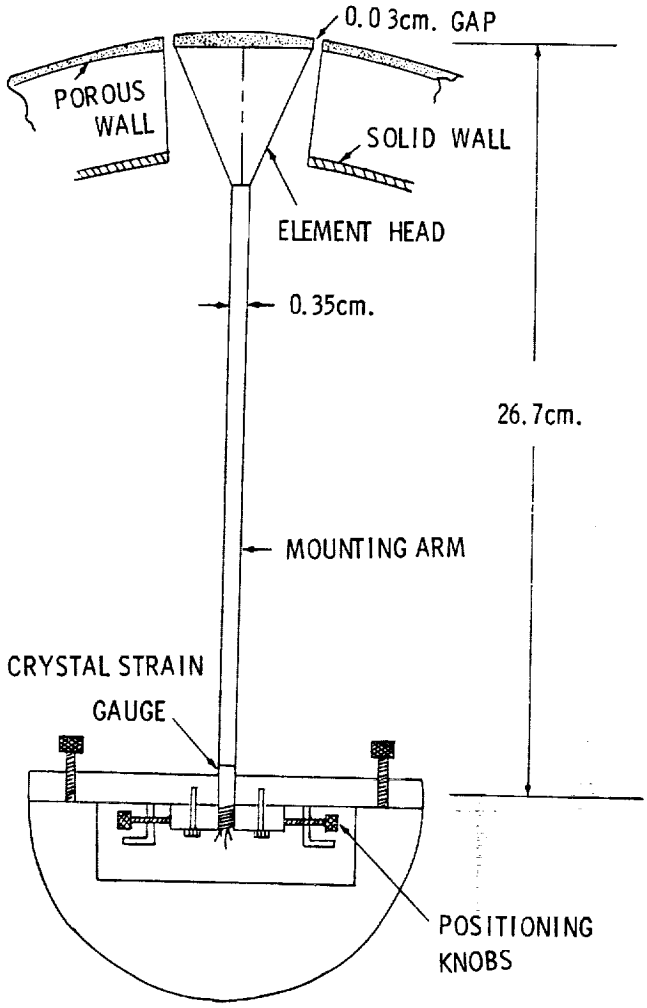

Fig. 10. Skin friction balance for configuration 2 and 3.

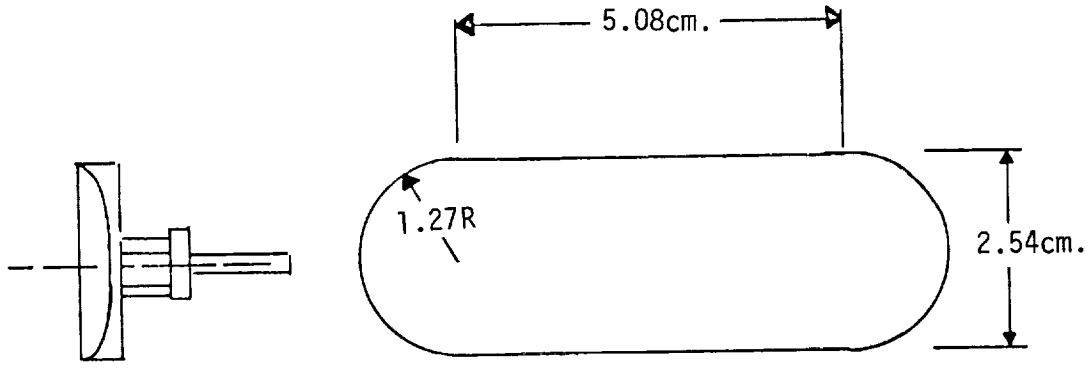

ELEMENT HEAD FOR CONFIGURATION 1.

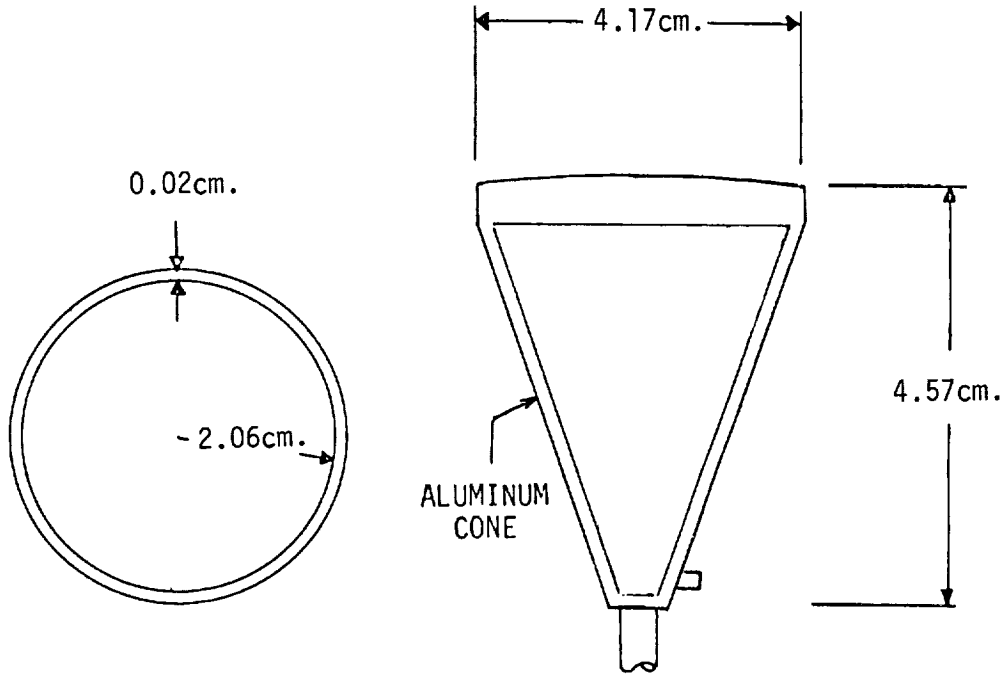

ELEMENT HEAD FOR CONFIGURATION 2 & 3.

Fig. 11. Element heads used in the experiments.

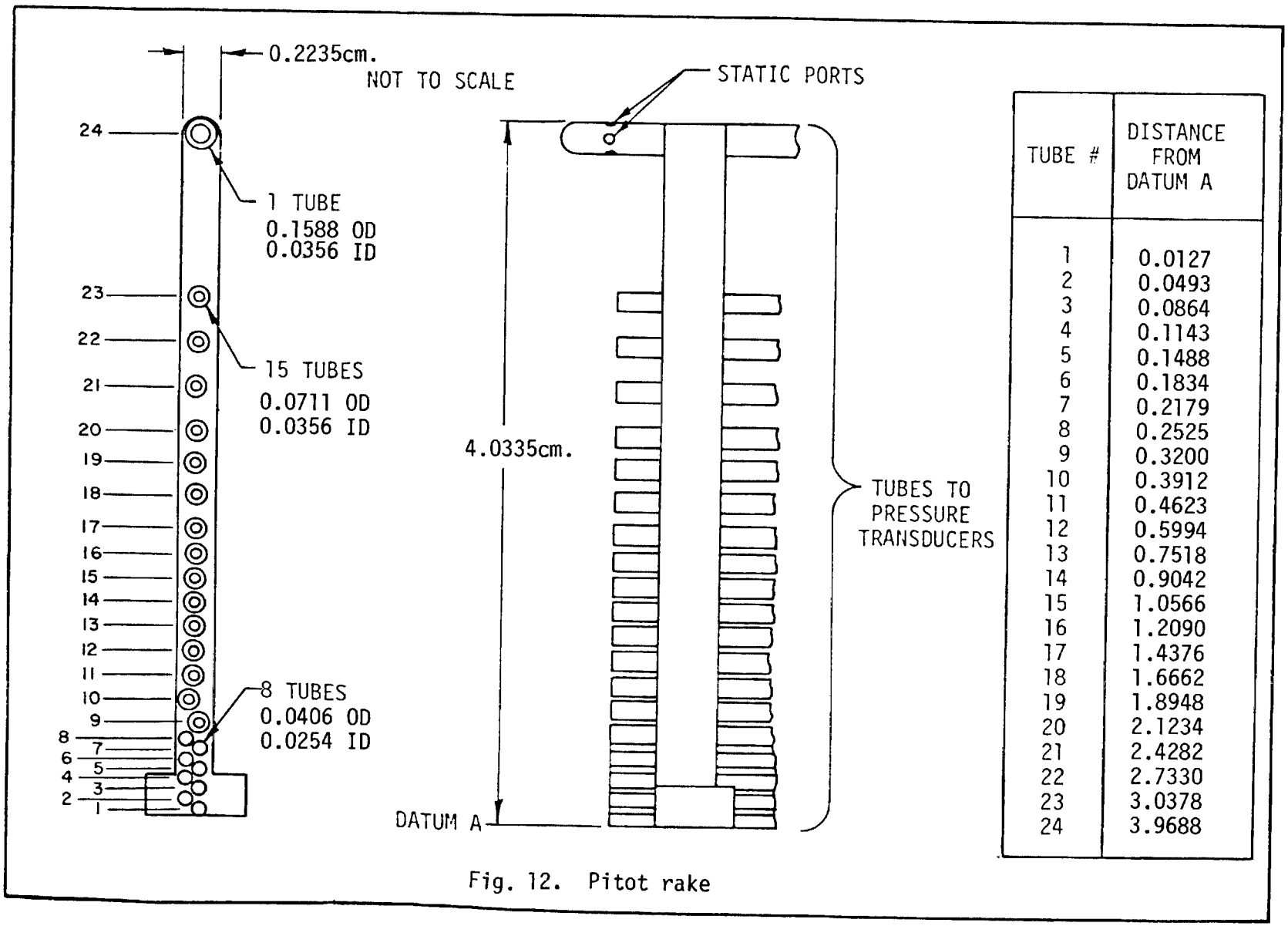

TUBE #	DISTANCE FROM DATUM A
1	0.0127
2	0.0493
3	0.0864
4	0.1143
5	0.1488
6	0.1834
7	0.2179
8	0.2525
9	0.3200
10	0.3912
11	0.4623
12	0.5994
13	0.7518
14	0.9042
15	1.0566
16	1.2090
17	1.4376
18	1.6662
19	1.8948
20	2.1234
21	2.4282
22	2.7330
23	3.0378
24	3.9688

Fig. 12. Pitot rake

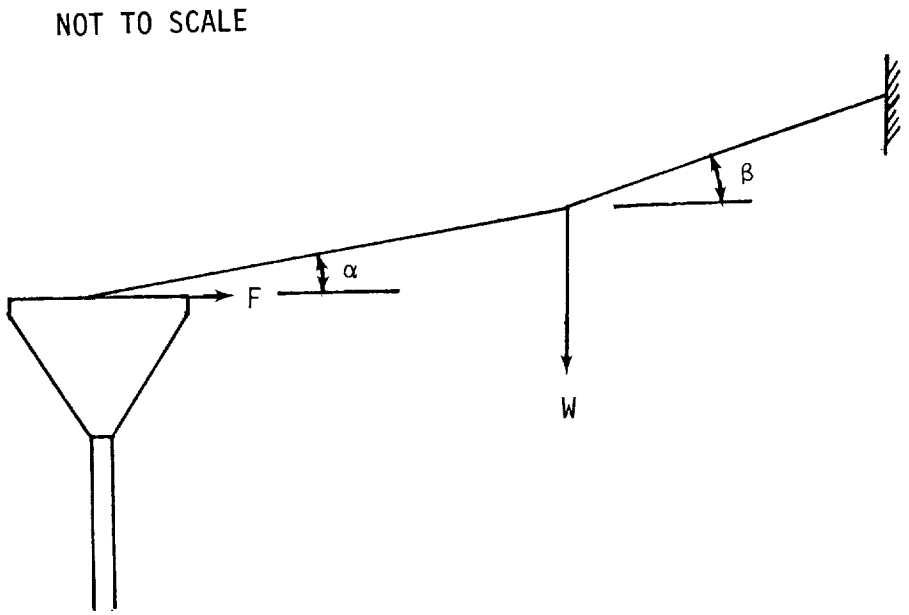

Fig. 13. Skin friction calibration setup.

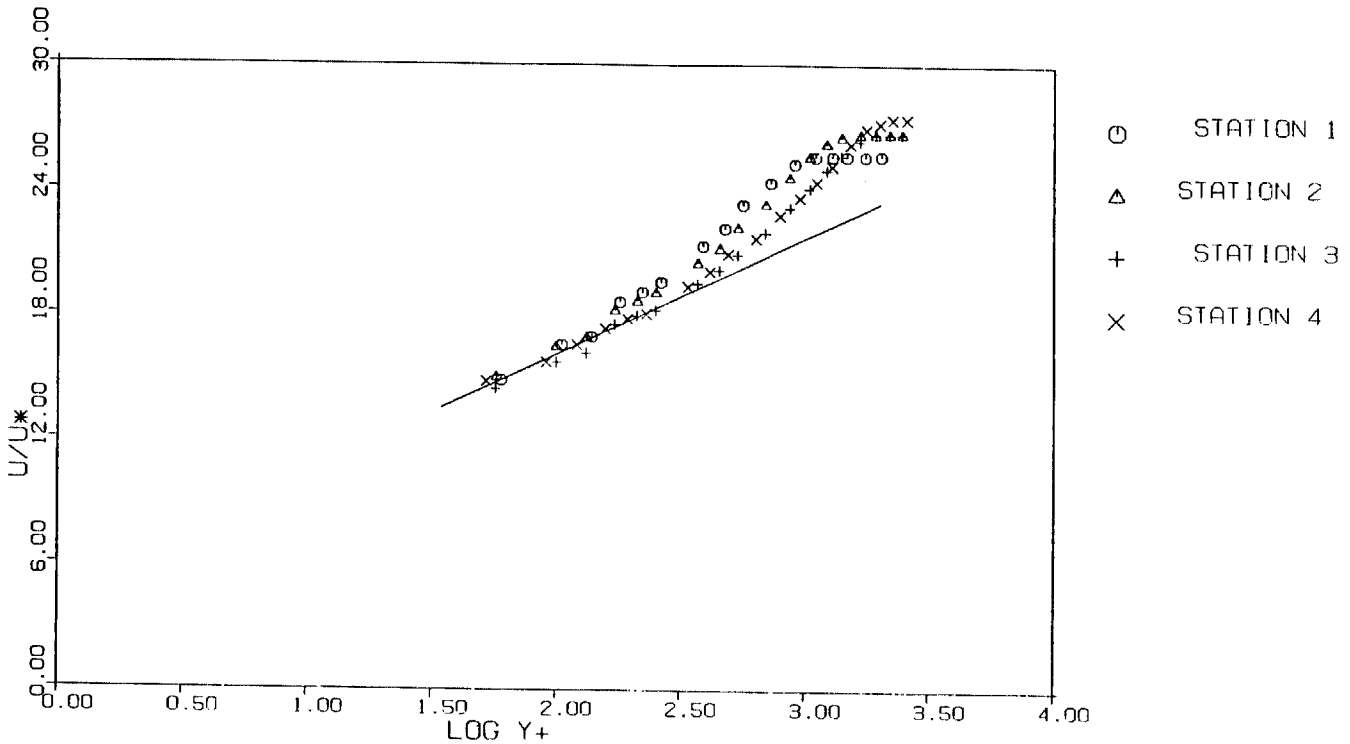

Fig. 14(a). Law of the Wall plot of smooth, solid wall results, all stations, q=12.7 cm. H_2O. —— Clauser Log Law

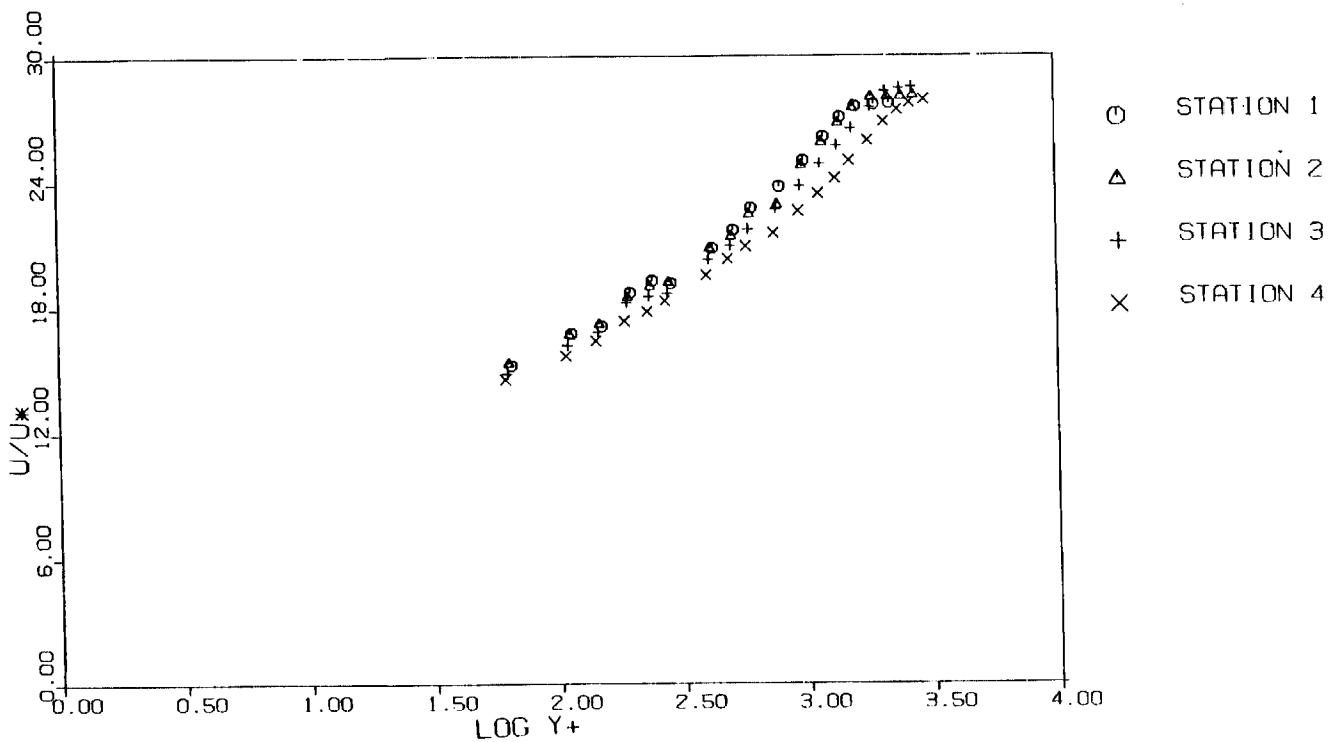

Fig. 14(b). Law of the Wall plot of smooth, solid wall results, all stations, q=17.8 cm. H_2O.

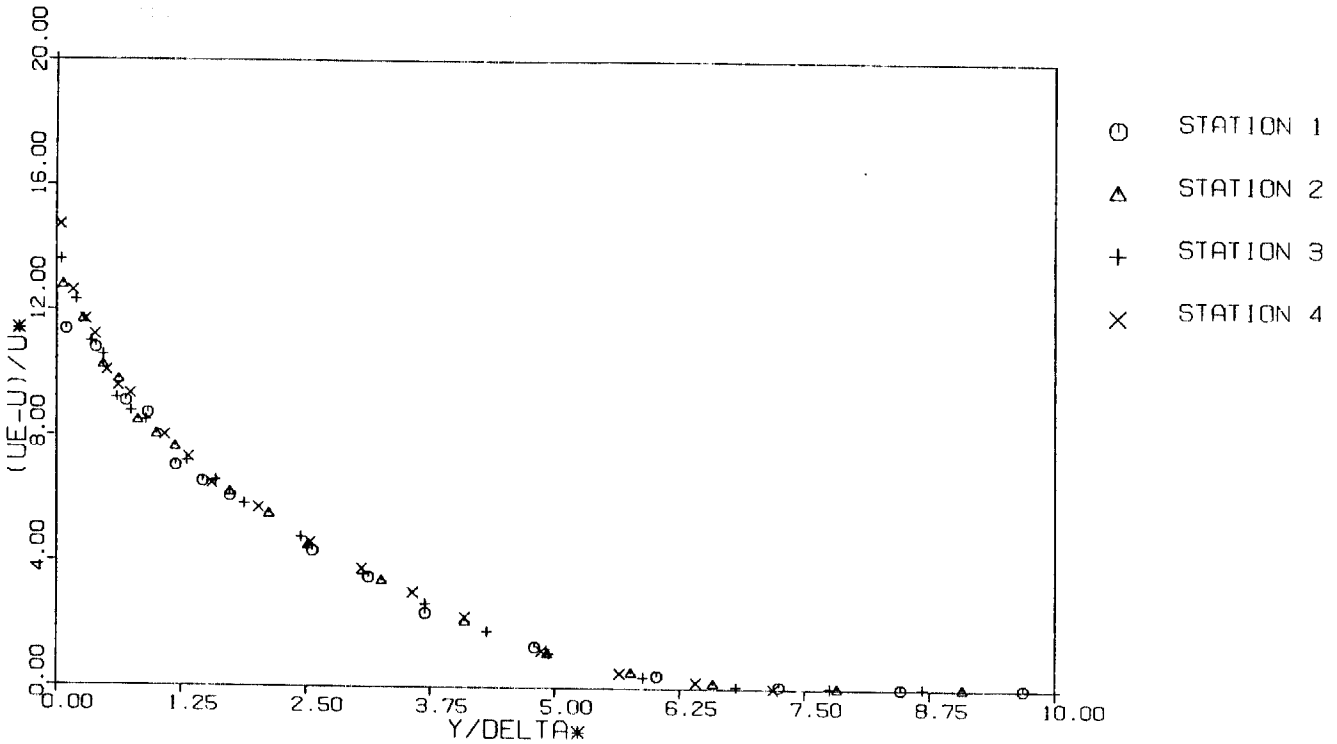

Fig. 15 . Defect Law plot of smooth, solid wall results, all stations, q=12.7 cm H_2O.

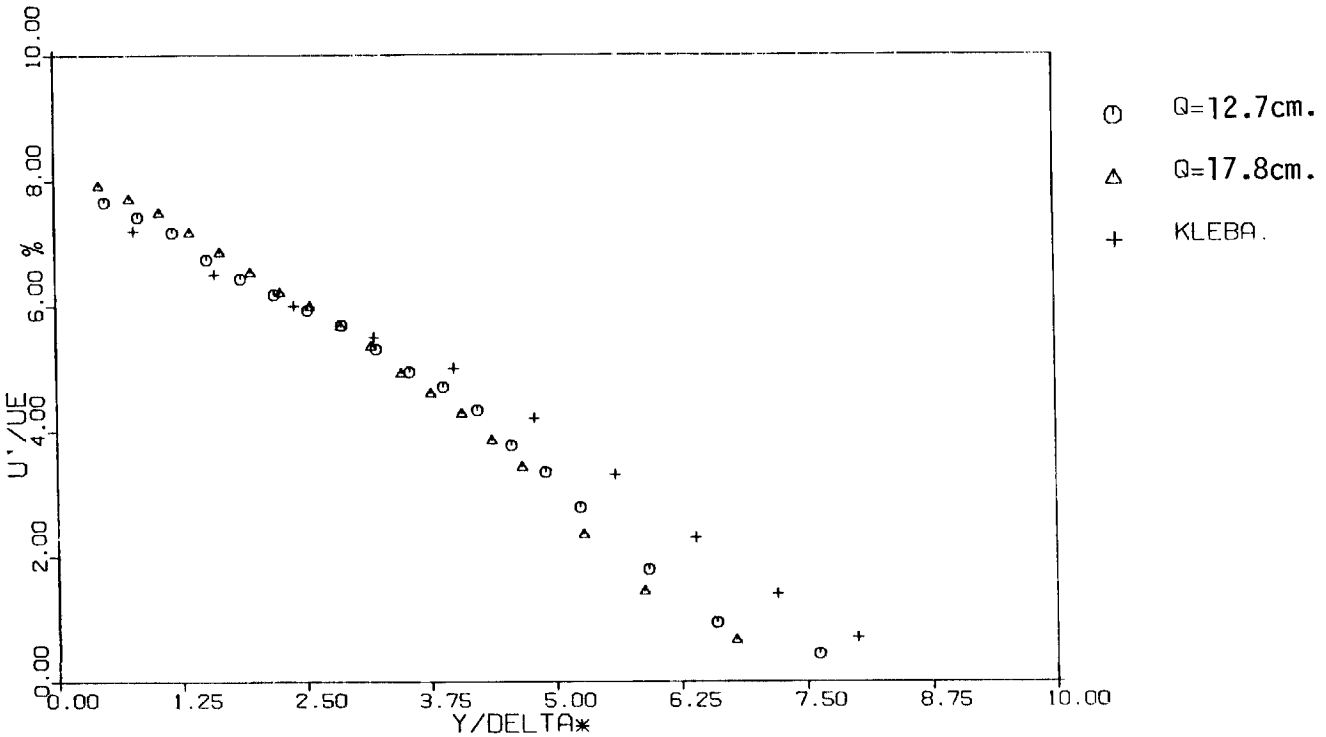

Fig. 16 . Axial turbulence intensity profiles for smooth, solid wall tests, station 4, q=12.7 and 17.8 cm. H_2O. Compared with results of Klebanoff.

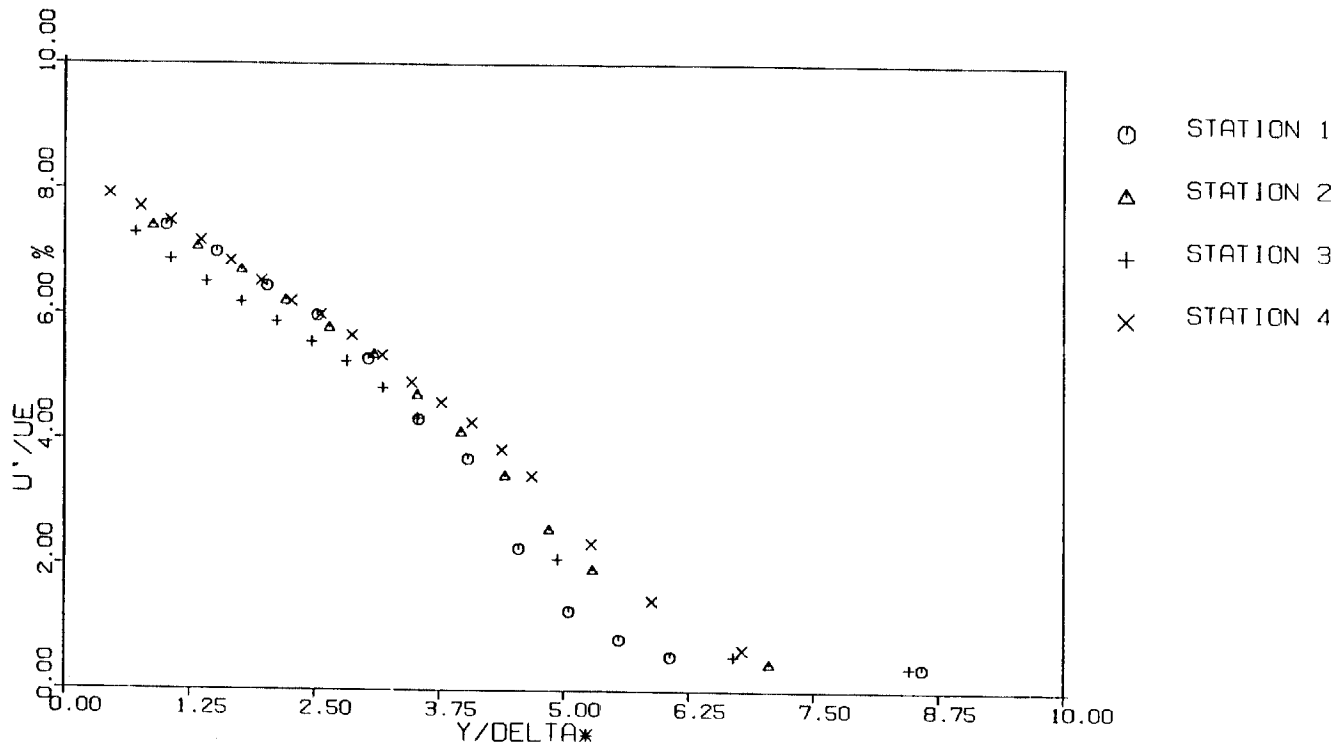

Fig. 17. Axial turbulence intensity profiles for smooth, solid wall tests, all stations, q=17.8 cm. H_2O.

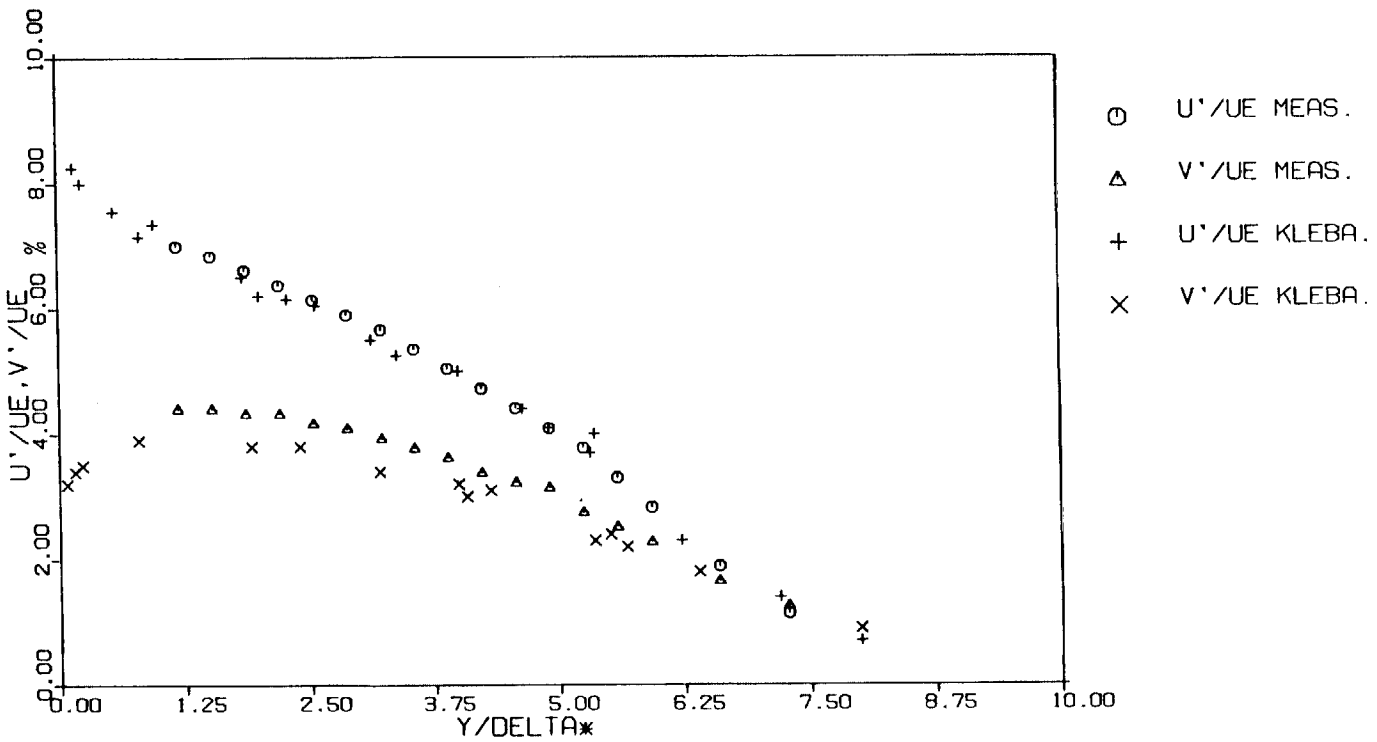

Fig. 18. Axial and normal turbulence intensity profiles for smooth, solid wall tests, station 4, q=12.7 cm. H_2O.

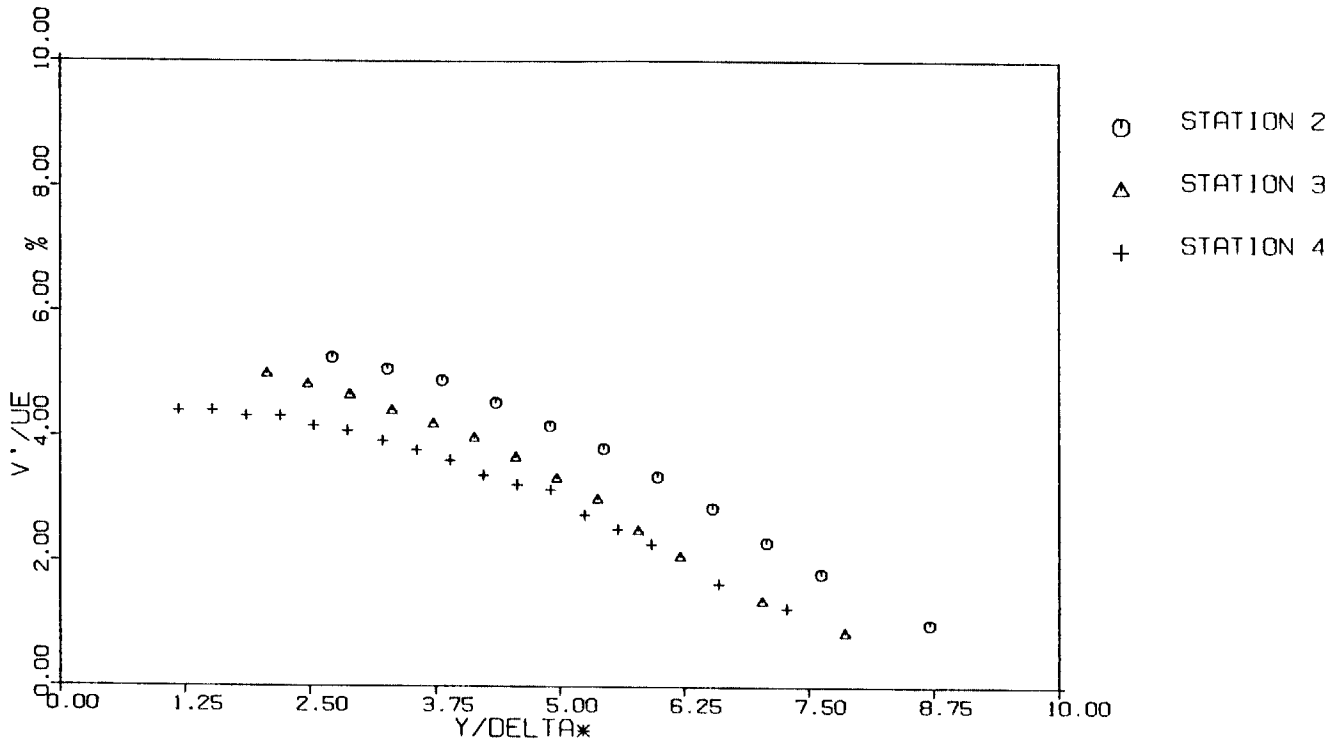

Fig. 19. Normal turbulence intensity profiles for smooth, solid wall tests, station 2, 3, and 4, q=12.7 cm. H_2O.

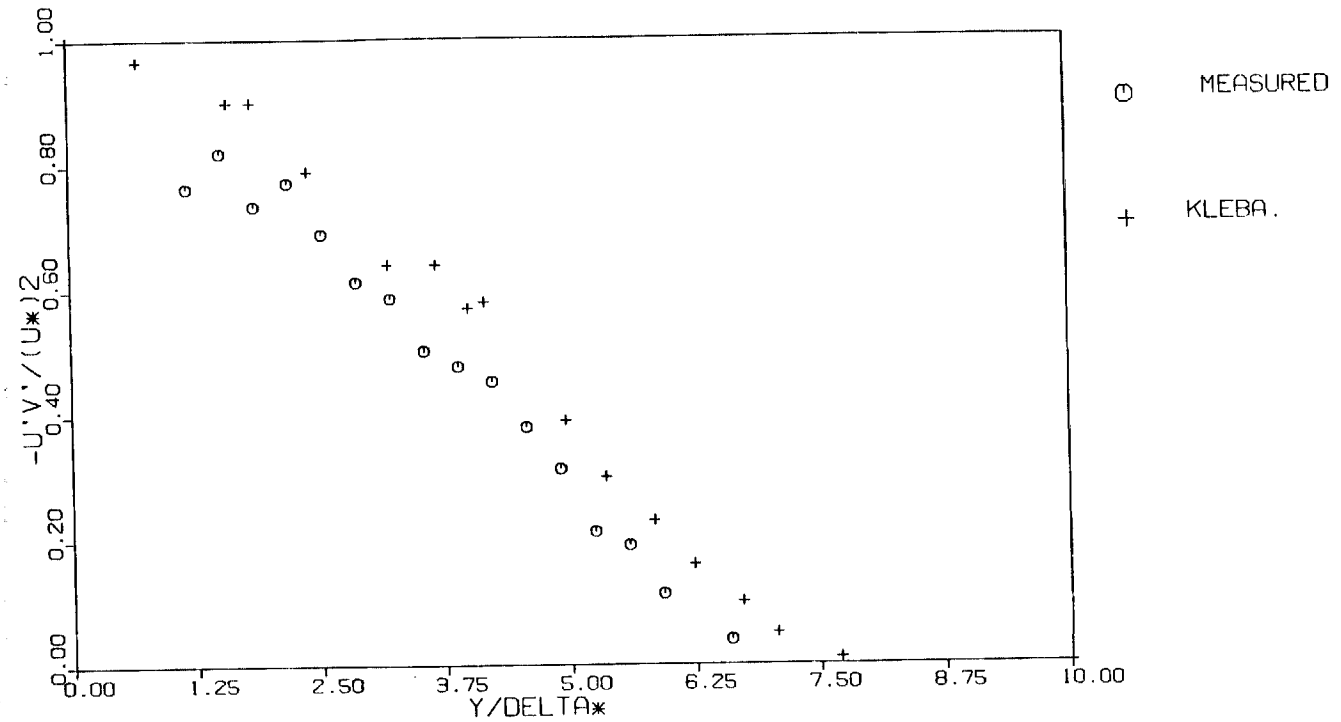

Fig. 20. Reynolds stress profiles for smooth, solid wall tests, station 4, q=12.7 cm. H_2O. Compared with results of Klebanoff.

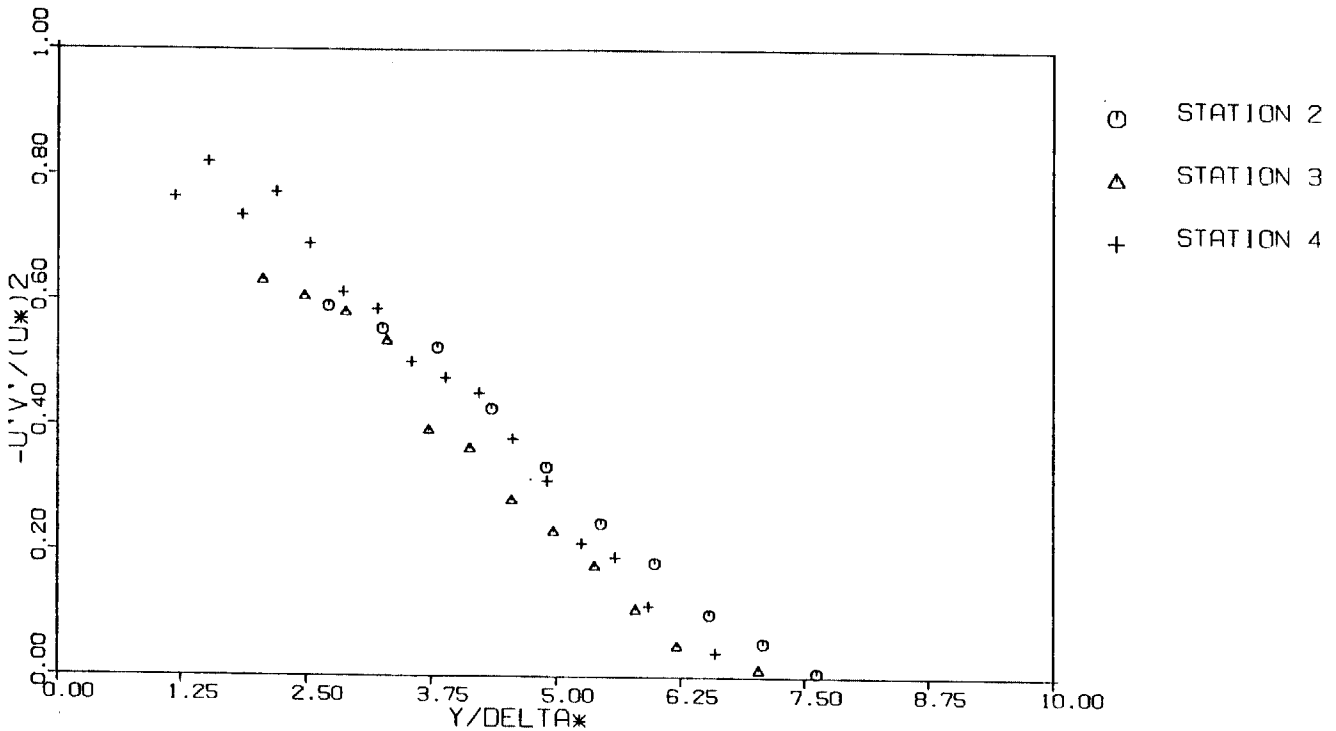

Fig. 21. Reynolds stress profiles for smooth, solid wall tests, station 2, 3, and 4, q=12.7 cm. H_2O.

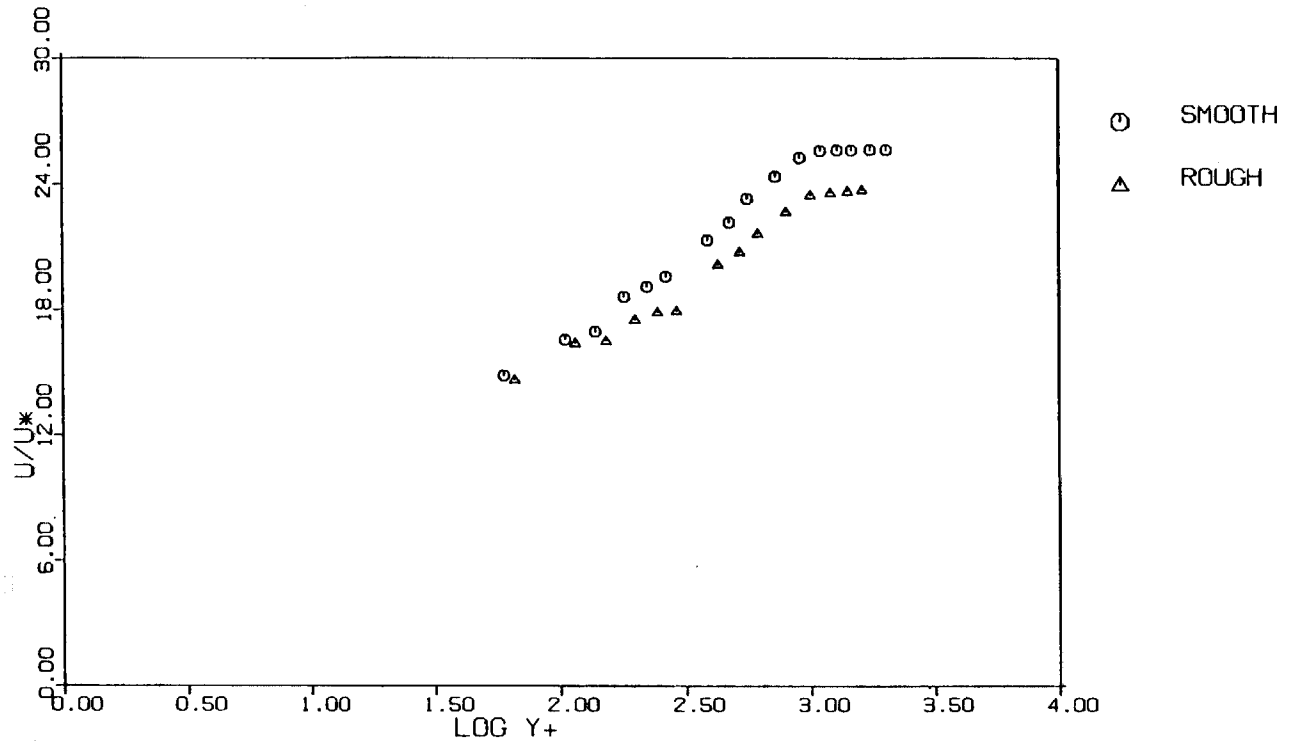

Fig. 22(a). Law of the Wall plot of smooth and sand-roughened wall tests, station 1, q=12.7 cm. H_2O.

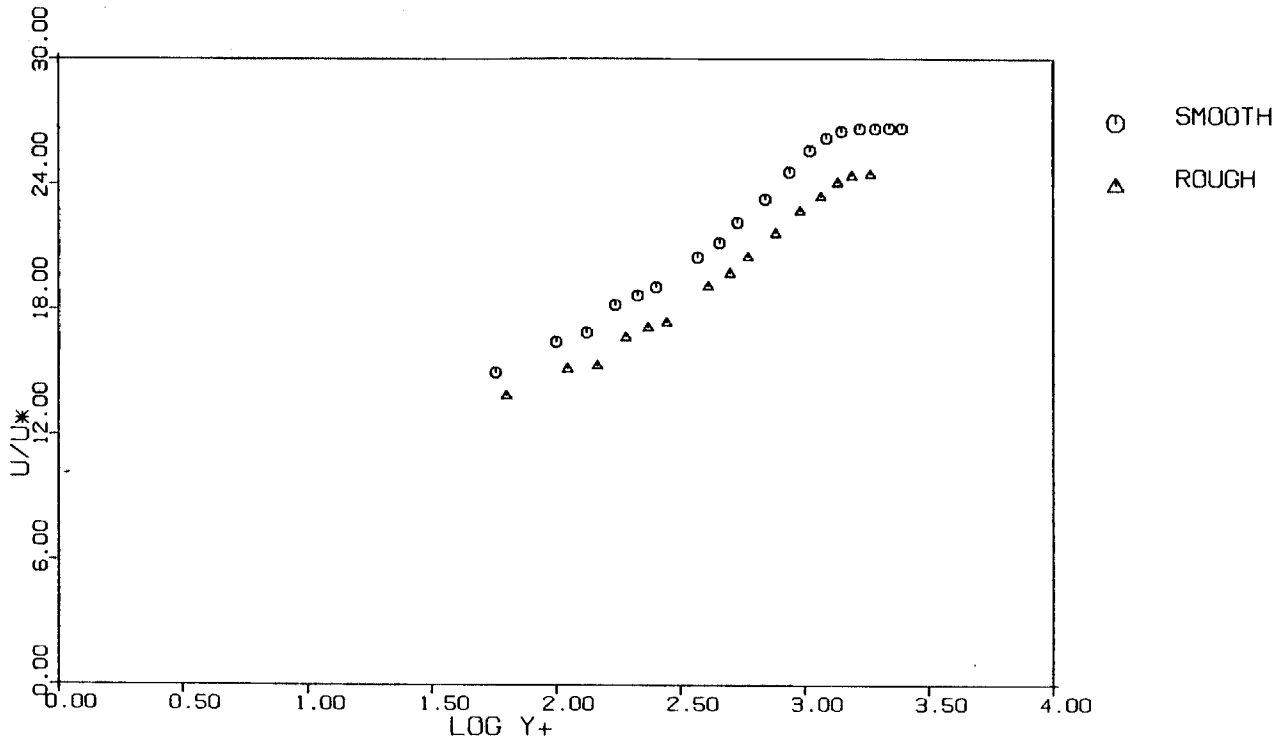

Fig. 22(b). Law of the Wall plot of smooth and sand-roughened wall tests, station 2, q=12.7 cm. H_2O.

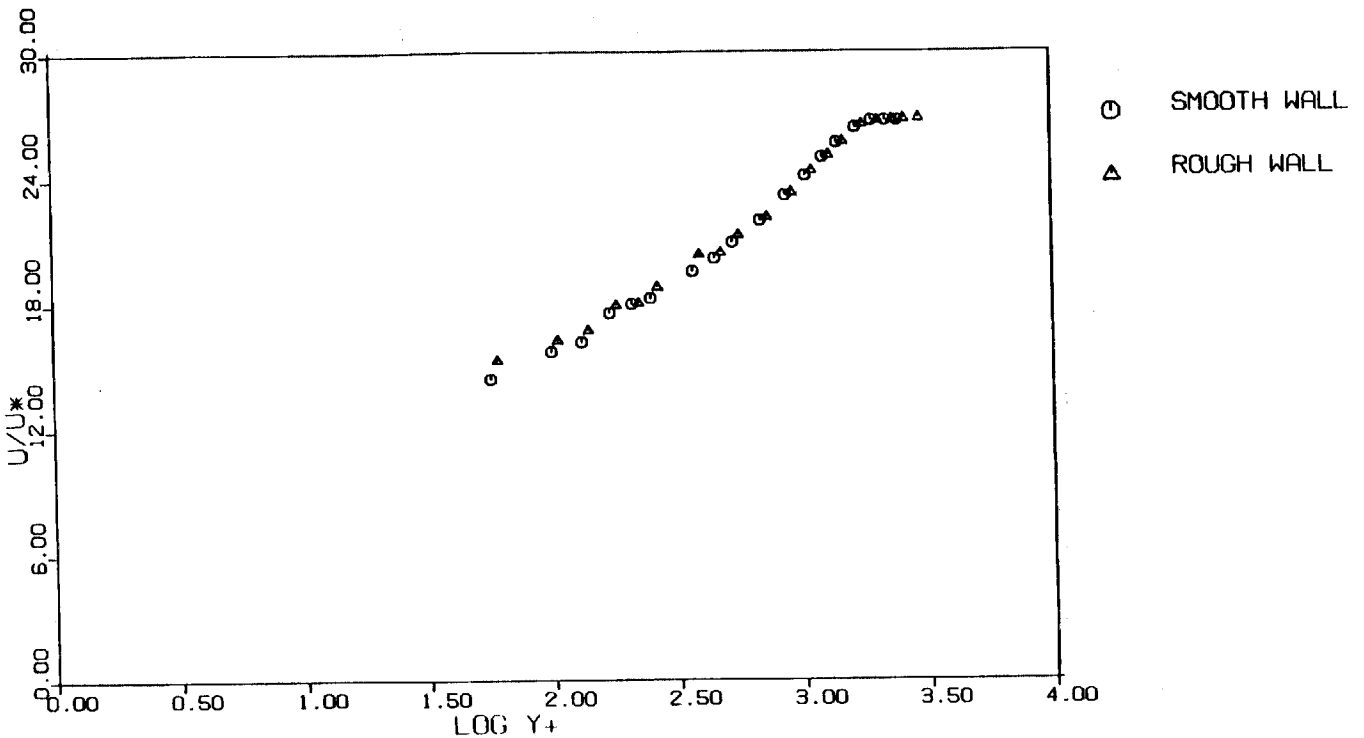

Fig. 22(c). Law of the Wall plot of smooth and sand-roughened wall tests, station 3, q=12.7 cm. H_2O.

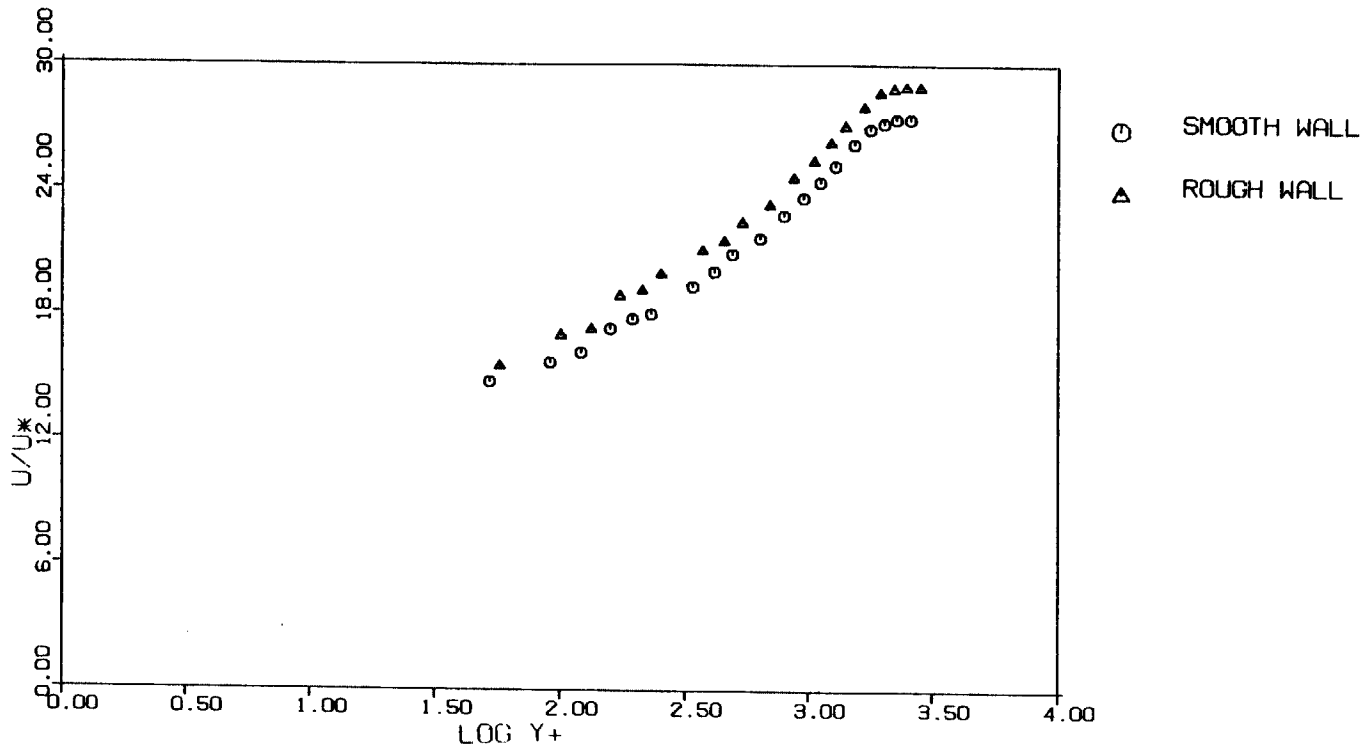

Fig. 22(d). Law of the Wall plot of smooth and sand-roughened wall tests, station 4, q=12.7 cm. H_2O.

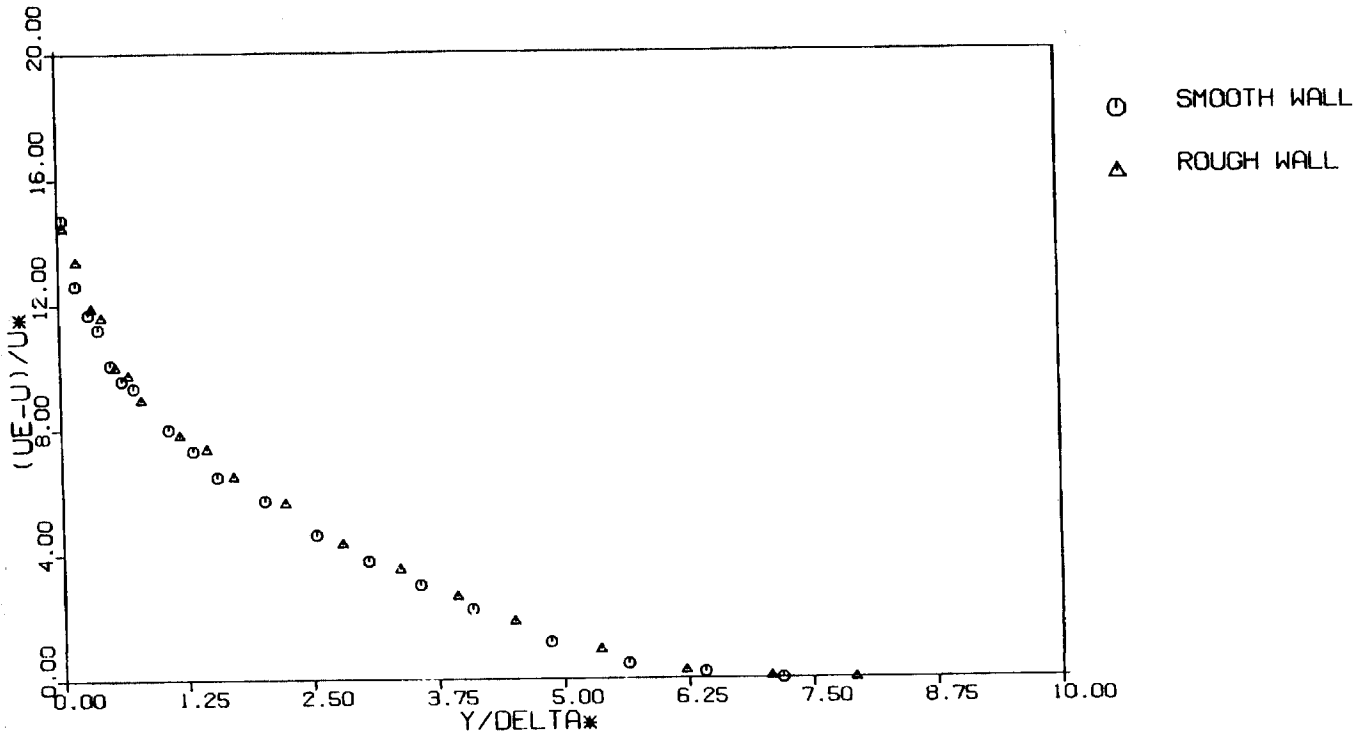

Fig. 23 . Defect Law plot of smooth and sand-roughened wall tests, station 4, q=12.7 cm. H_2O.

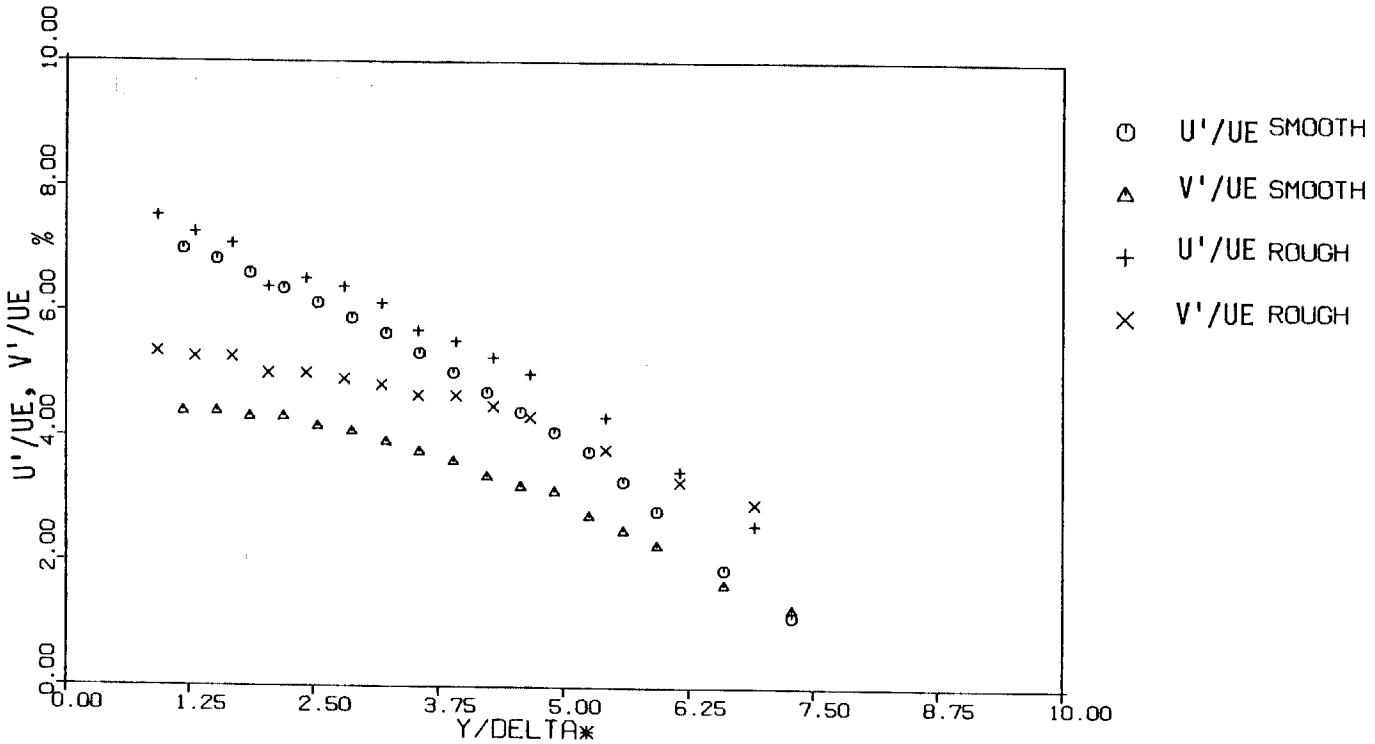

Fig. 24. Axial and normal turbulence intensity profiles for smooth and sand-roughened wall tests, station 4, q=12.7 cm. H_2O.

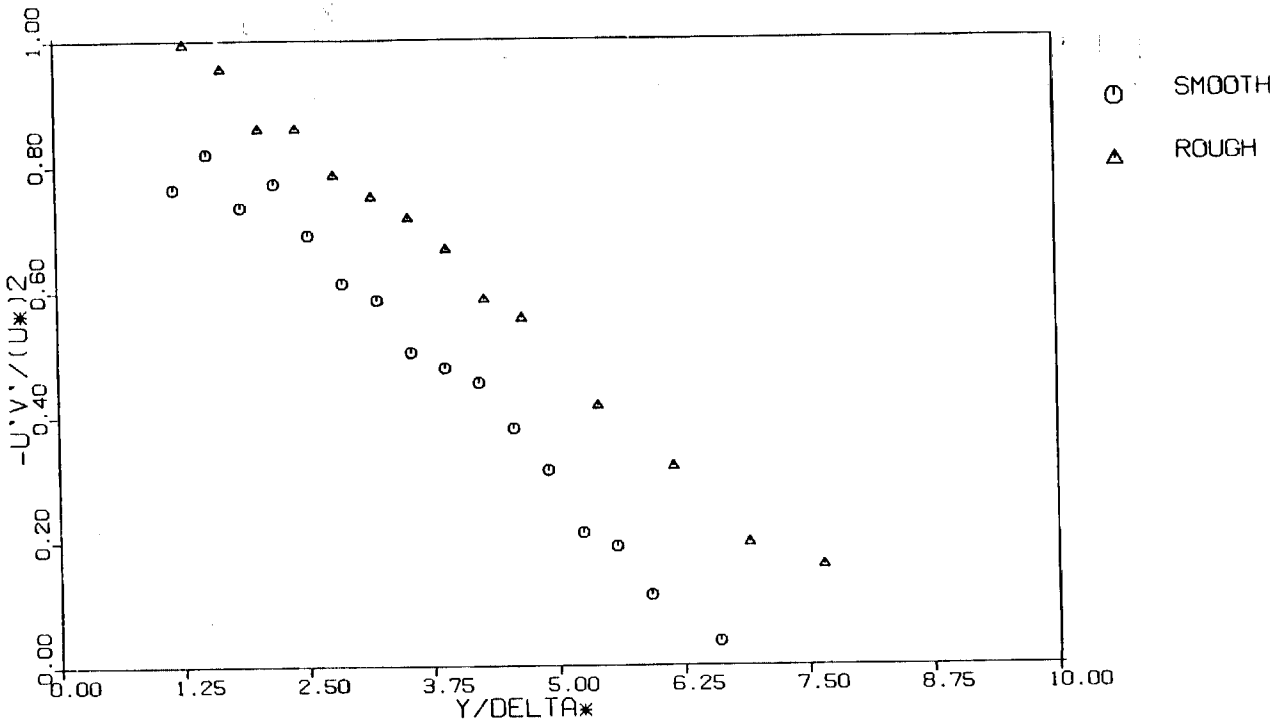

Fig. 25(a). Reynolds stress profiles for smooth and sand-roughened wall tests, station 4, q=12.7 cm. H_2O.

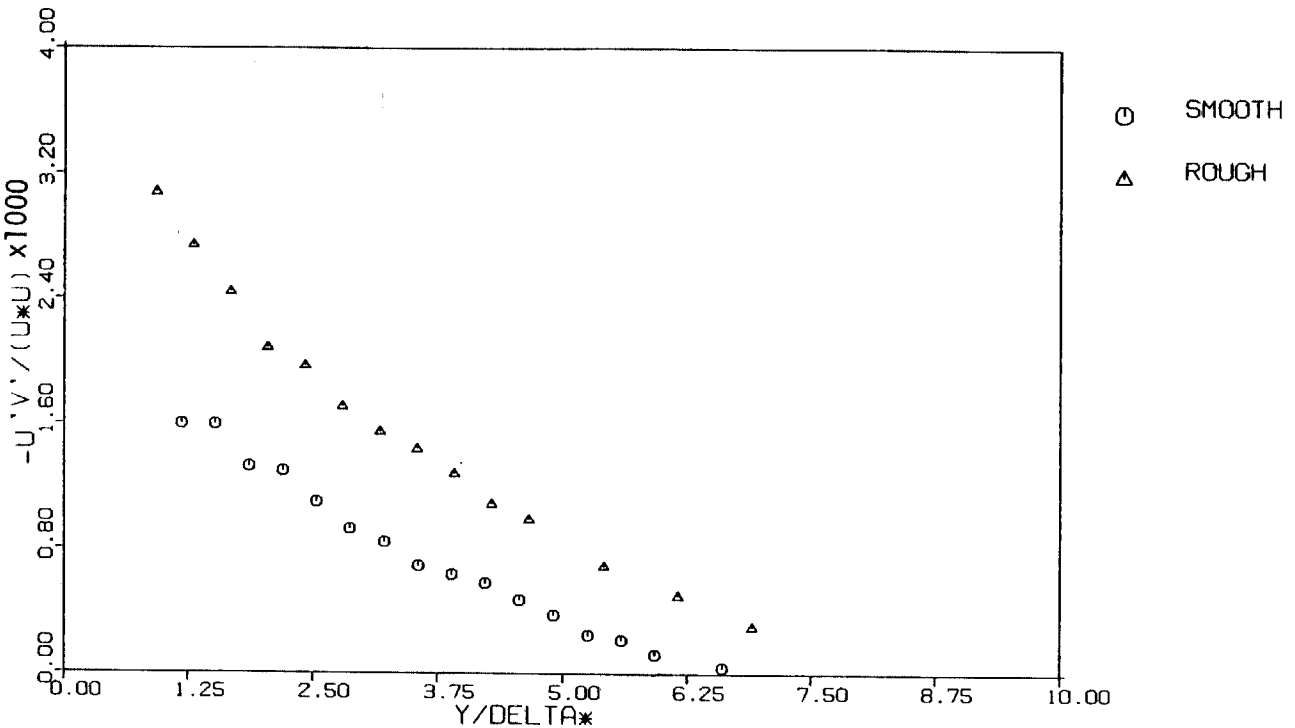

Fig. 25(b). Reynolds stress profiles normalized with local mean velocity for smooth and sand-roughened wall tests, station 4, q=12.7 cm. H_2O.

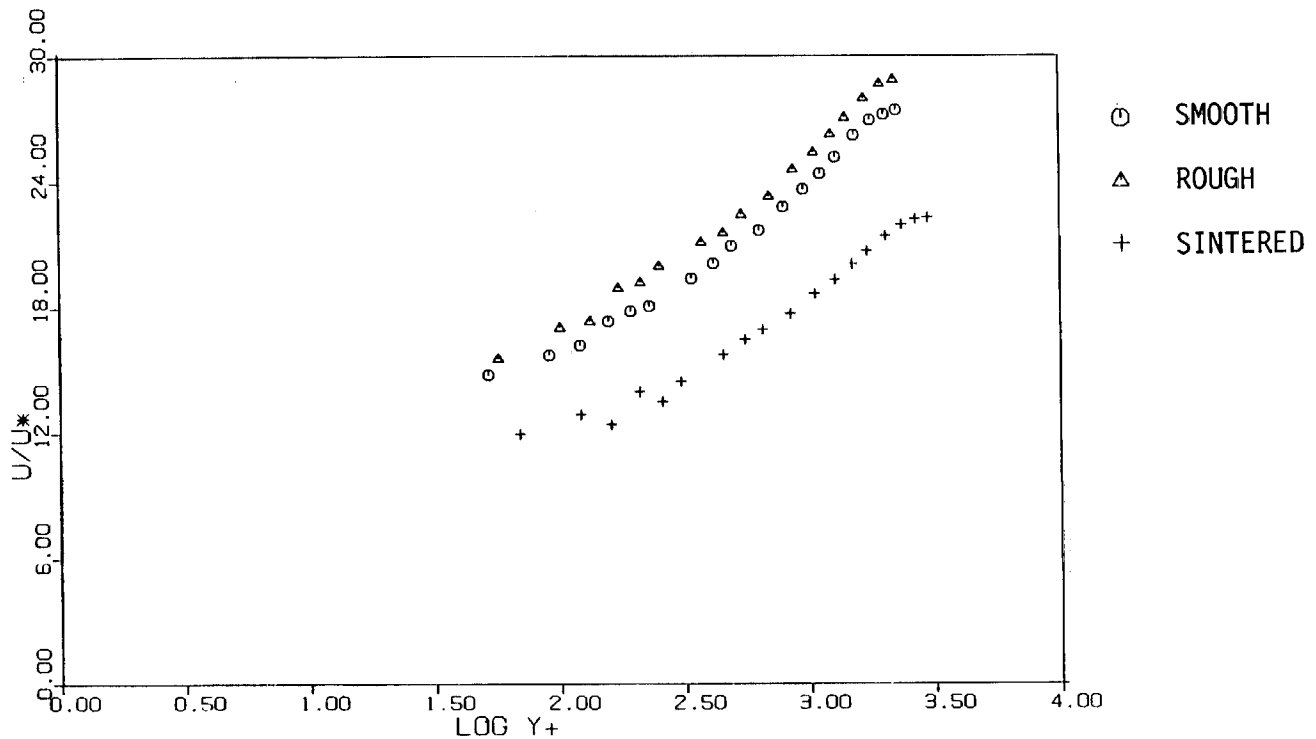

Fig. 26. Law of the Wall plot of smooth, sand-roughened and sintered metal, porous wall tests, station 4, q=12.7 cm. H_2O.

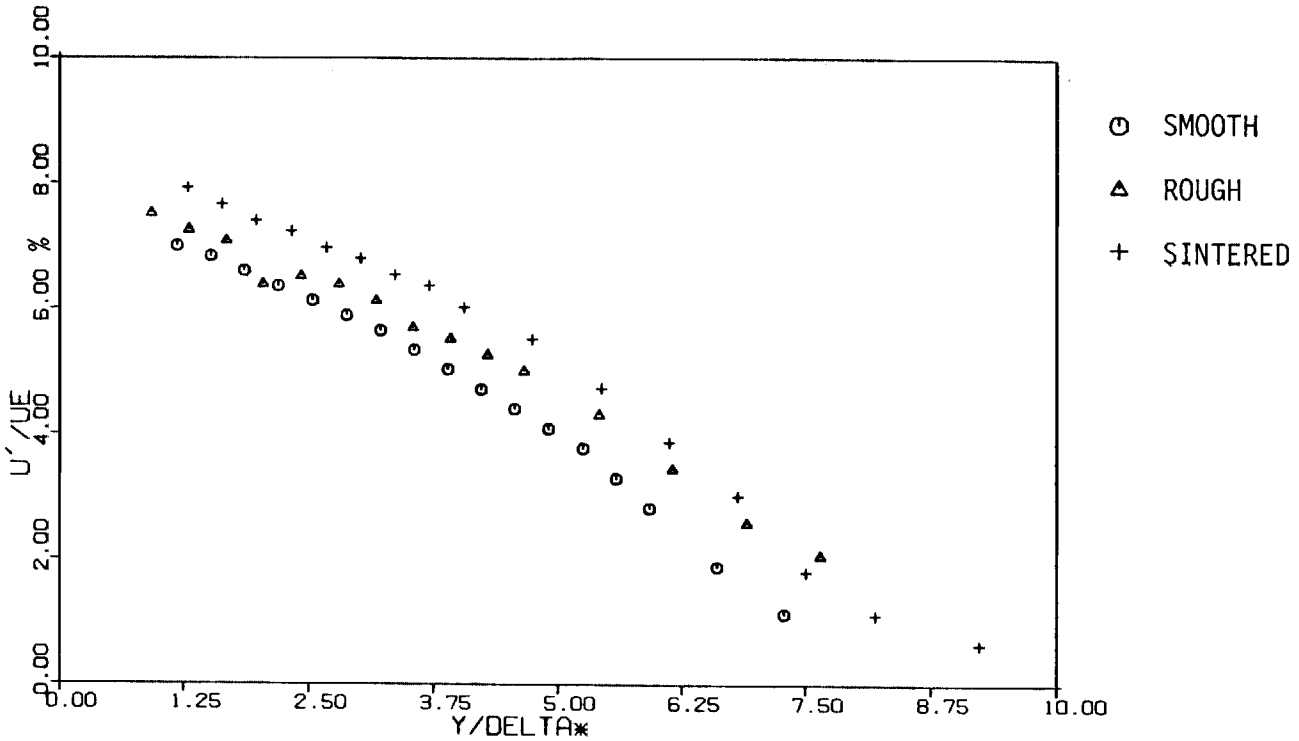

Fig. 27(a). Axial turbulence intensity profiles for smooth, sand-roughened and sintered metal, porous wall tests, station 4, q=12.7 cm. H_2O.

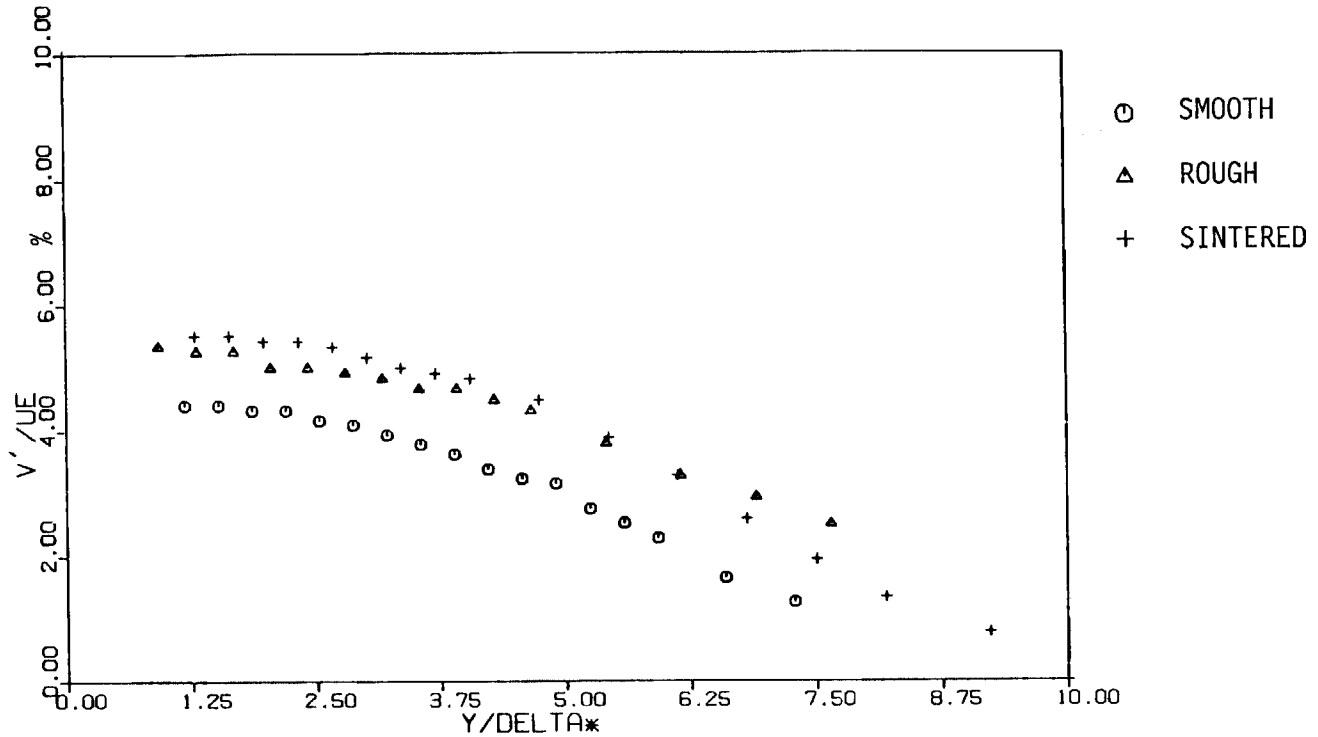

Fig. 27(b). Normal turbulence intensity profiles for smooth, sand-roughened and sintered metal, porous wall tests, station 4, q=12.7 cm. H_2O.

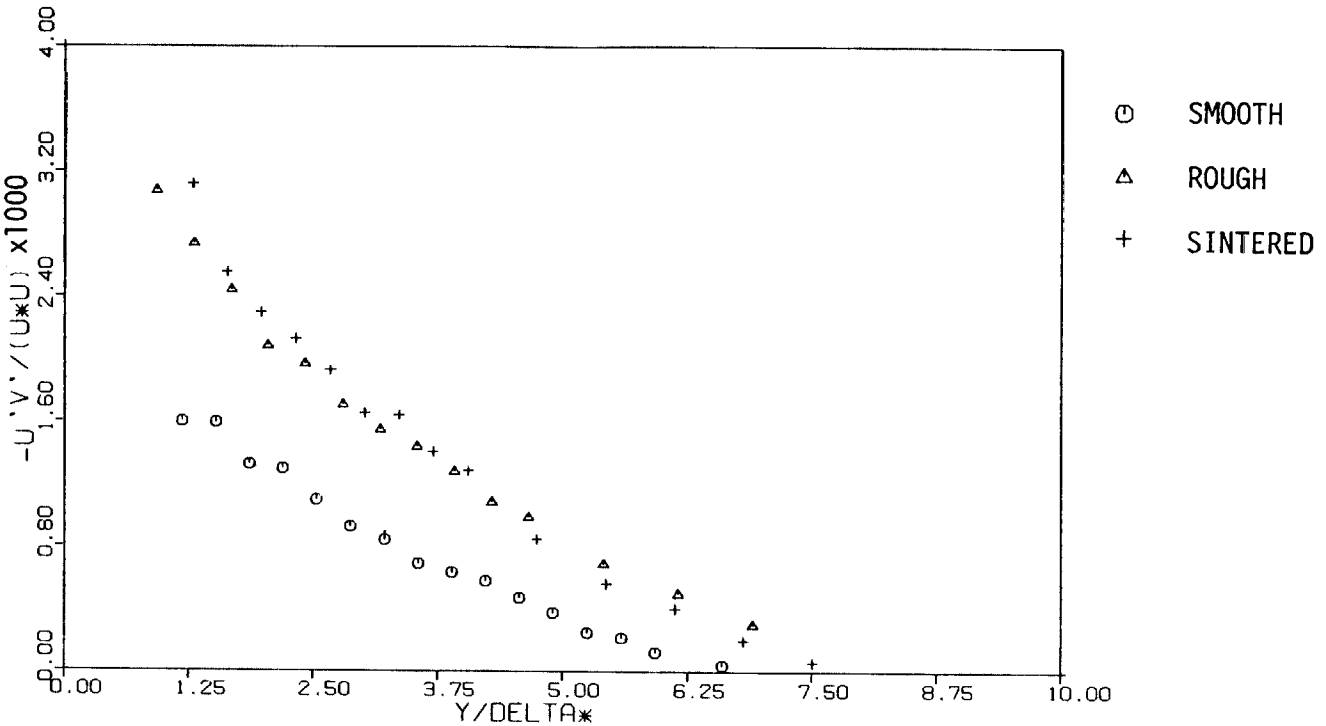

Fig. 28. Reynolds stress profiles normalized with local mean velocity for smooth, sand-roughened and sintered metal, porous wall tests, station 4, q=12.7 cm. H_2O.

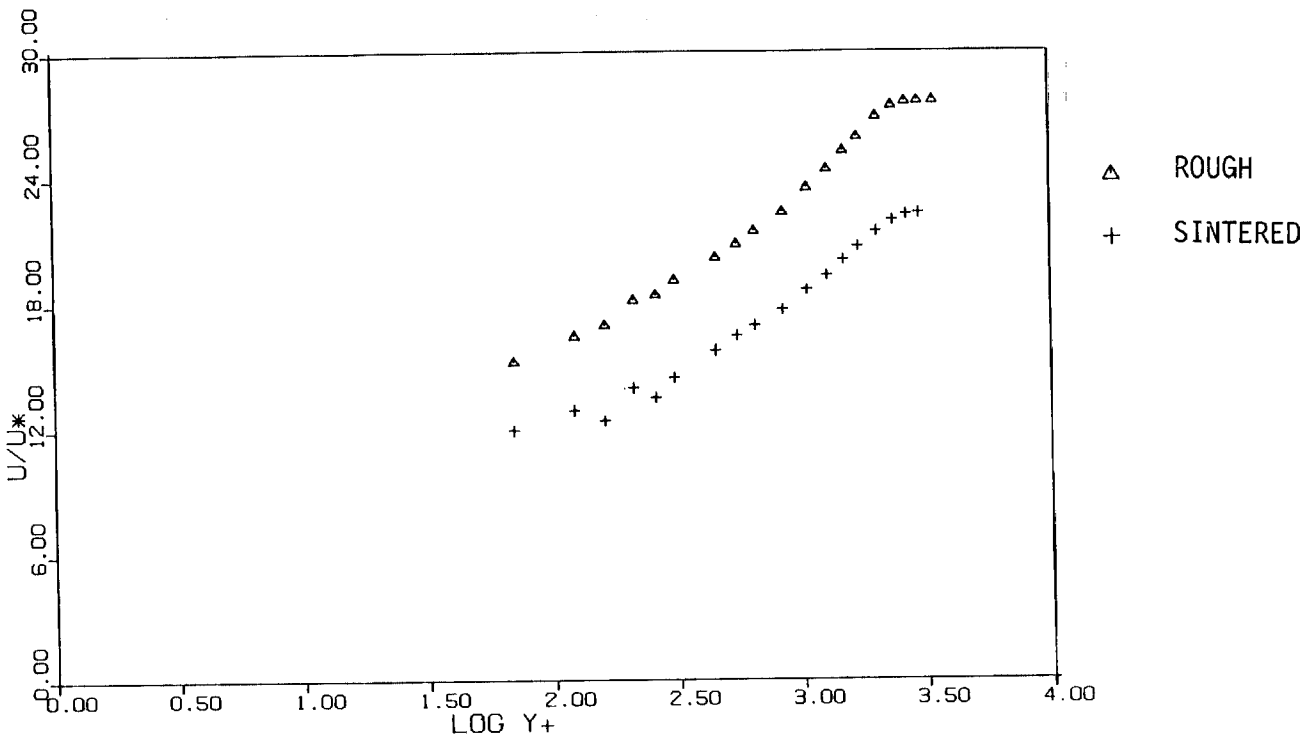

Fig. 29. Law of the Wall plot of sand-roughened wall test at station 3 and q=17.8 cm. H_2O and sintered metal, porous wall test at station 4, q=12.7 cm. H_2O——Matched k^+

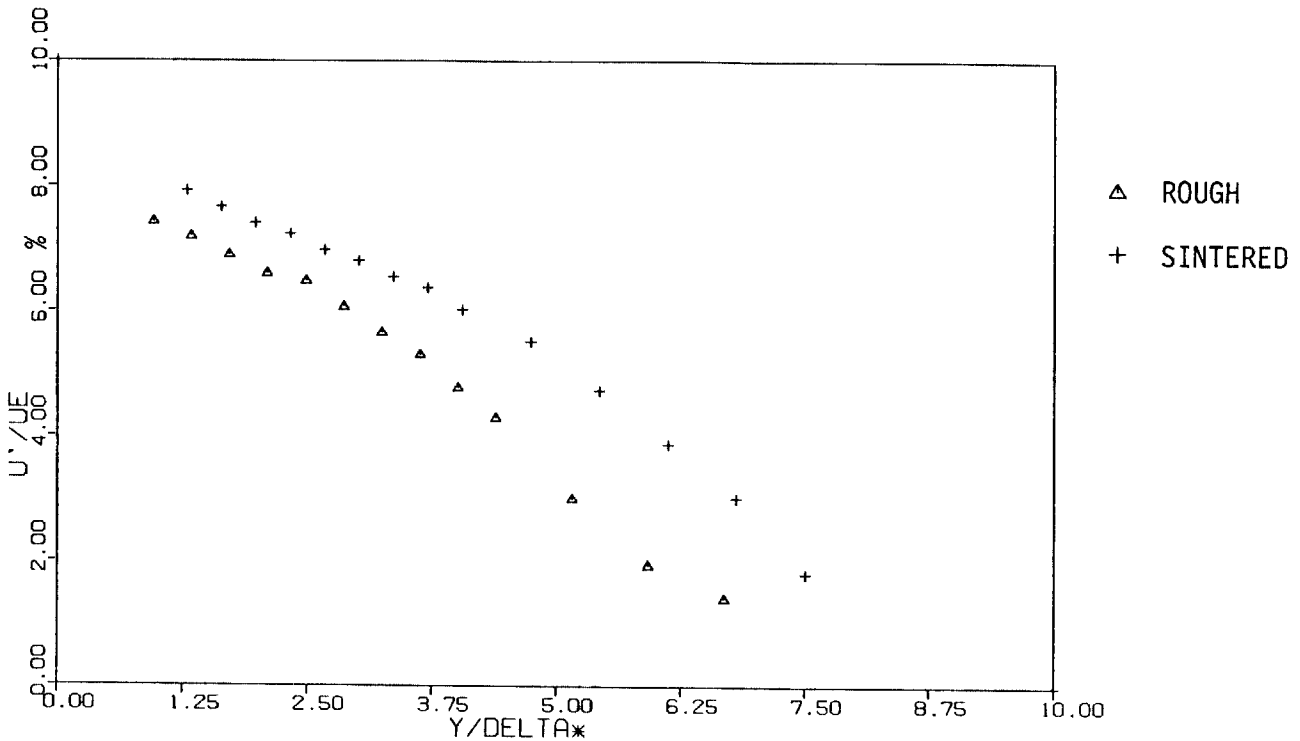

Fig. 30(a). Axial turbulence intensity profiles for sand-roughened wall test at station 3 and q=17.8 cm. H_2O and sintered metal, porous wall test at station 4 and q=12.7 cm. H_2O —— Matched k^+

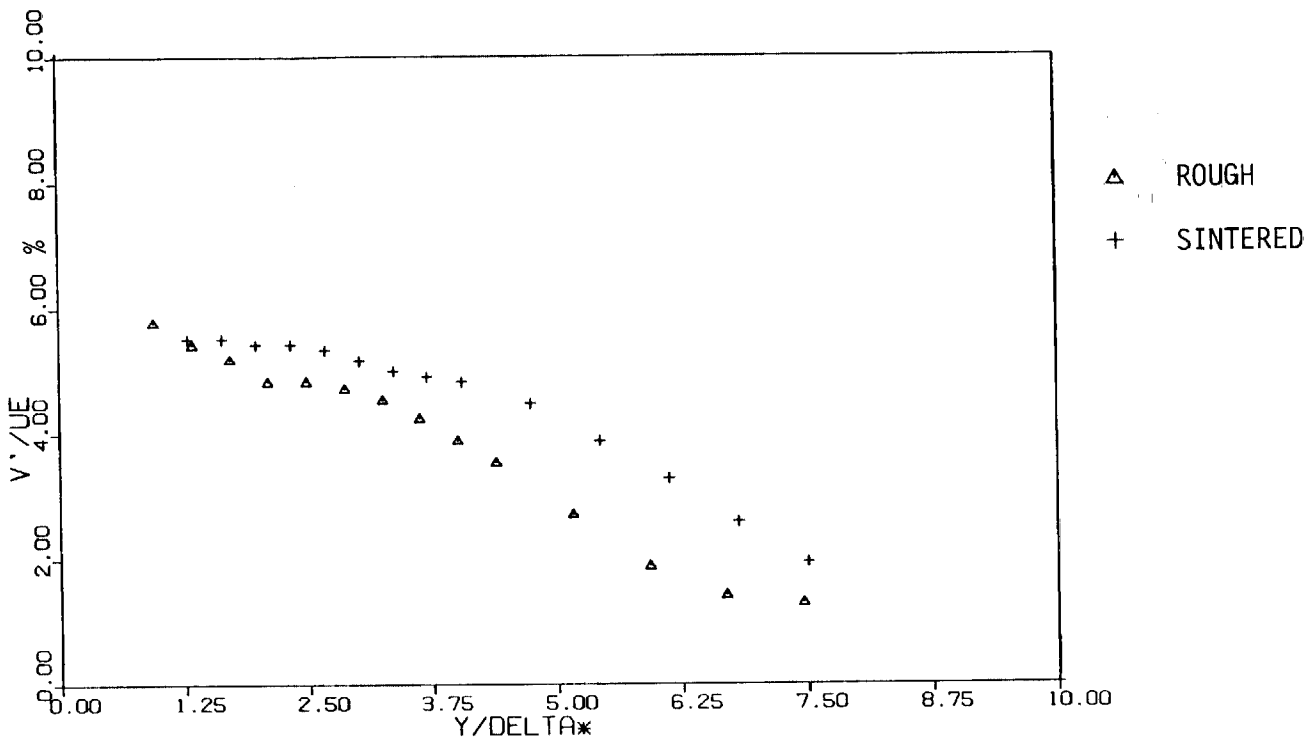

Fig. 30(b). Normal turbulence intensity profiles for sand-roughened wall test at station 3 and q=17.8 cm. H_2O and sintered metal, porous wall tests at station 4 and q=12.7 cm. H_2O —— Matched k^+

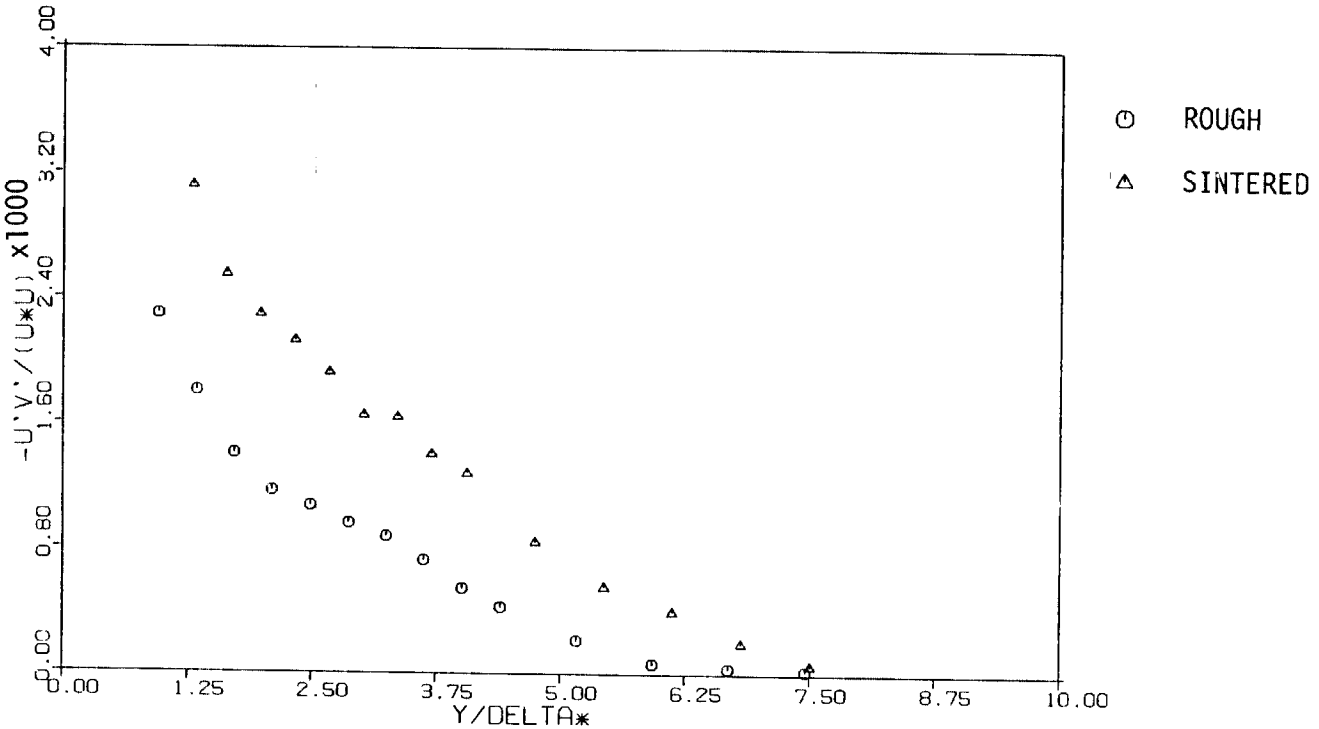

Fig. 31. Reynolds stress profiles normalized with local mean velocity for sand-roughened wall test at station 3 and q=17.8 cm. H_2O and sintered metal, porous wall test at station 4 and q=12.7 cm. H_2O
—— Matched k^+

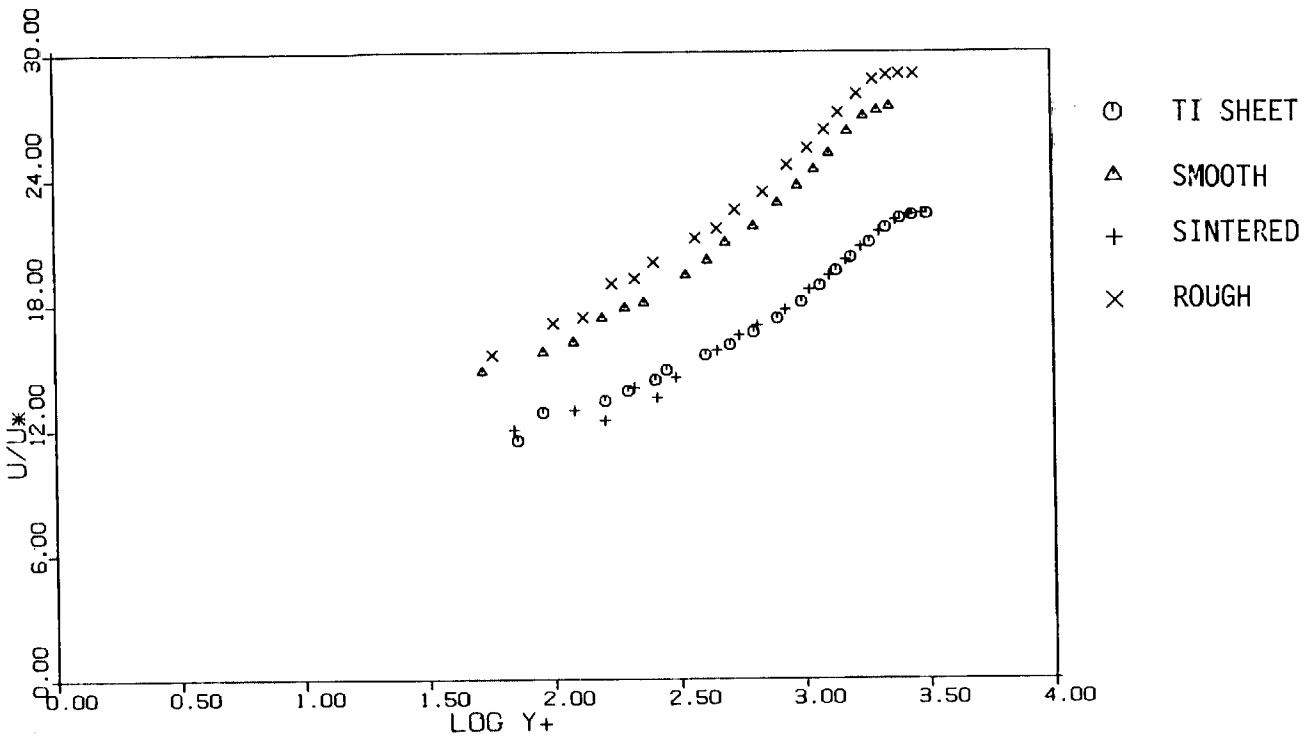

Fig. 32. Law of the Wall plot of smooth, sand-roughened, sintered metal porous, and perforated titanium wall tests, station 4, q=12.7 cm. H_2O.

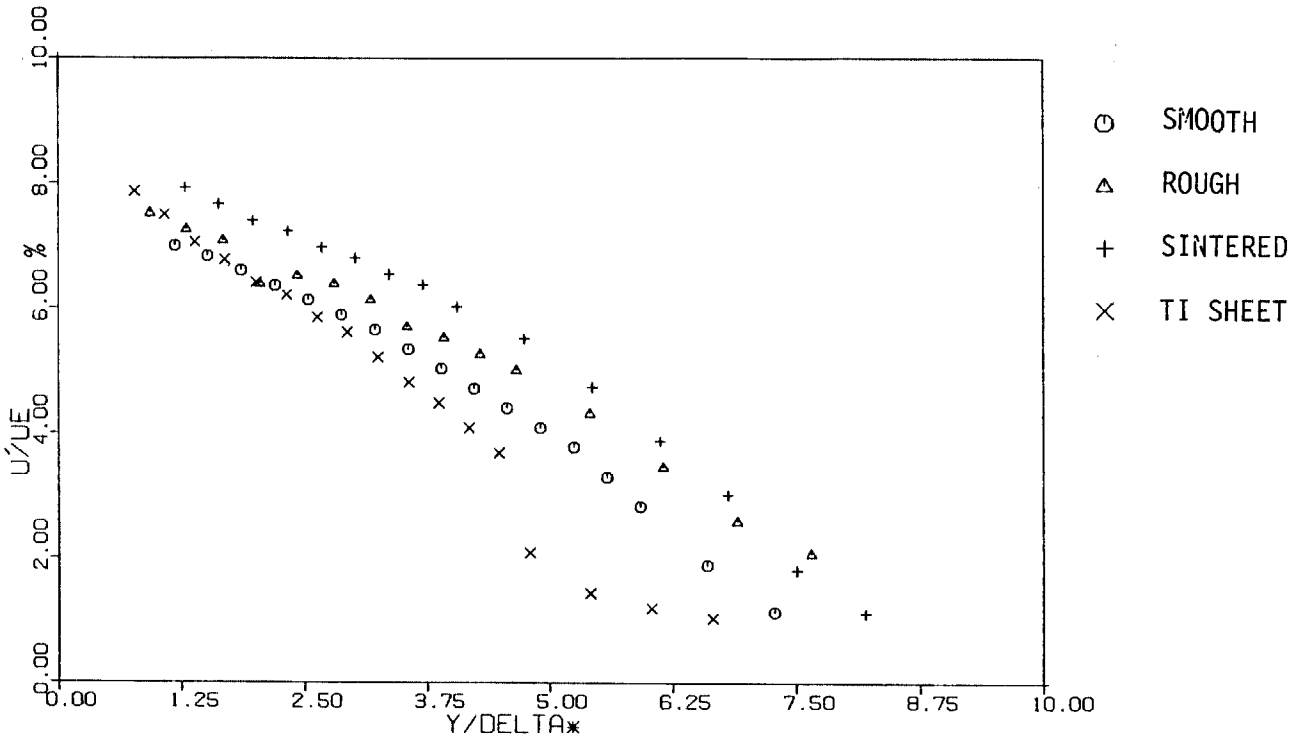

Fig. 33. Axial turbulence intensity profiles for smooth, sand-roughened, sintered metal,porous, and perforated titanium wall tests, station 4, q=12.7 cm. H_2O.

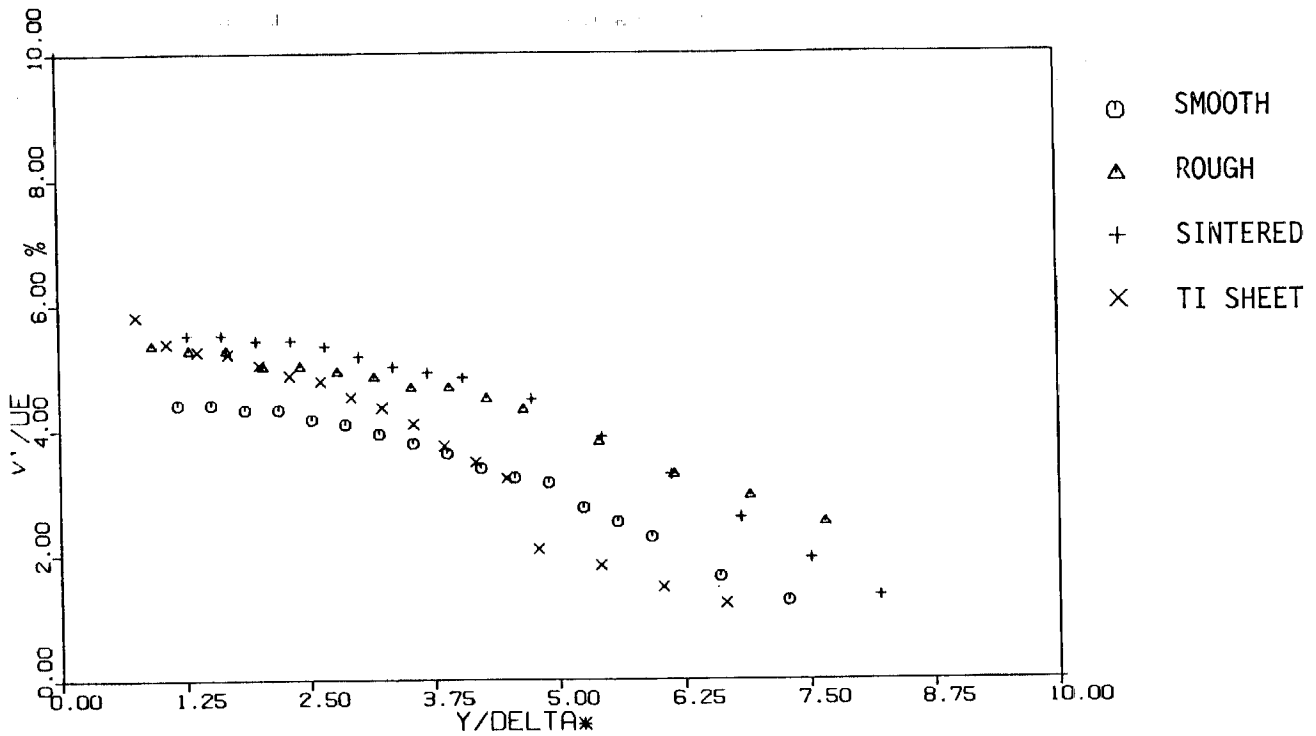

Fig. 34. Normal turbulence intensity profiles for smooth, sand-roughened, sintered metal, porous, and perforated titanium wall tests, station 4, q=12.7 cm. H_2O.

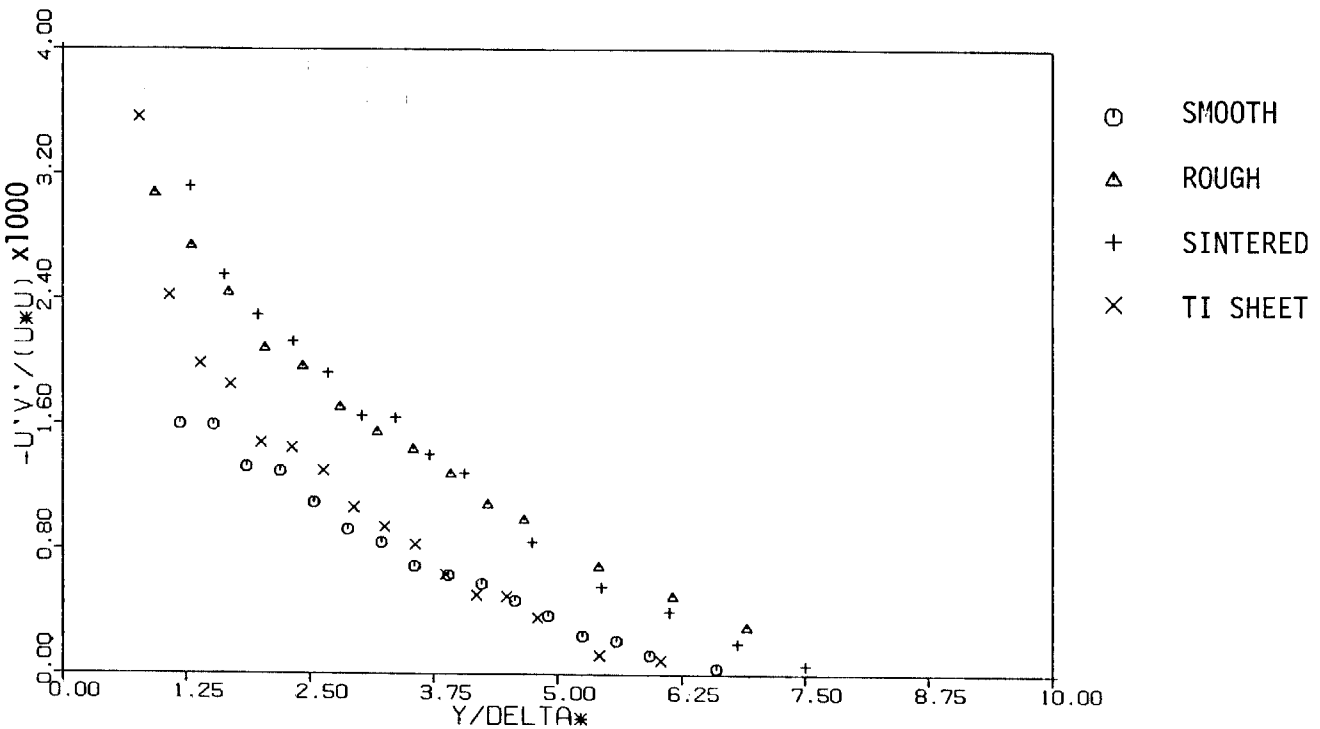

Fig. 35. Reynolds stress profiles normalized with local mean velocity for smooth, sand-roughened, sintered metal, porous, and perforated titanium wall tests, station 4, q=12.7 cm. H_2O.

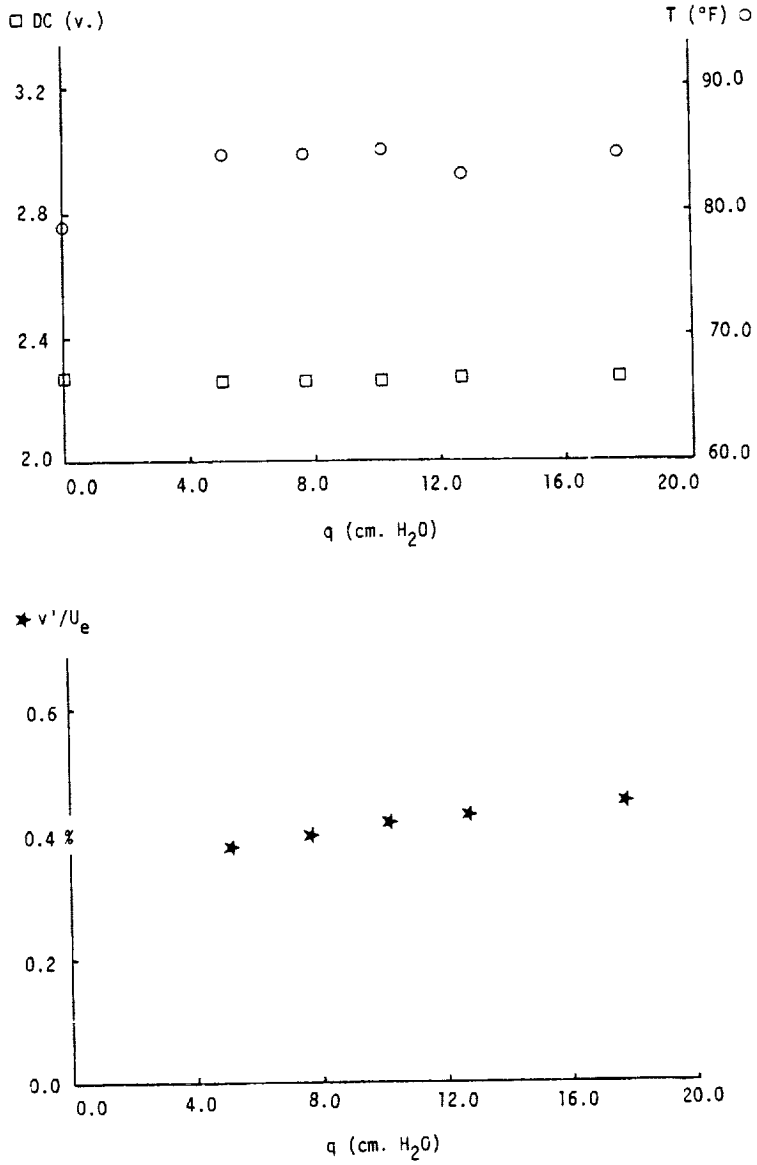

Fig. 36. Penetration of turbulence through the perforated titanium wall

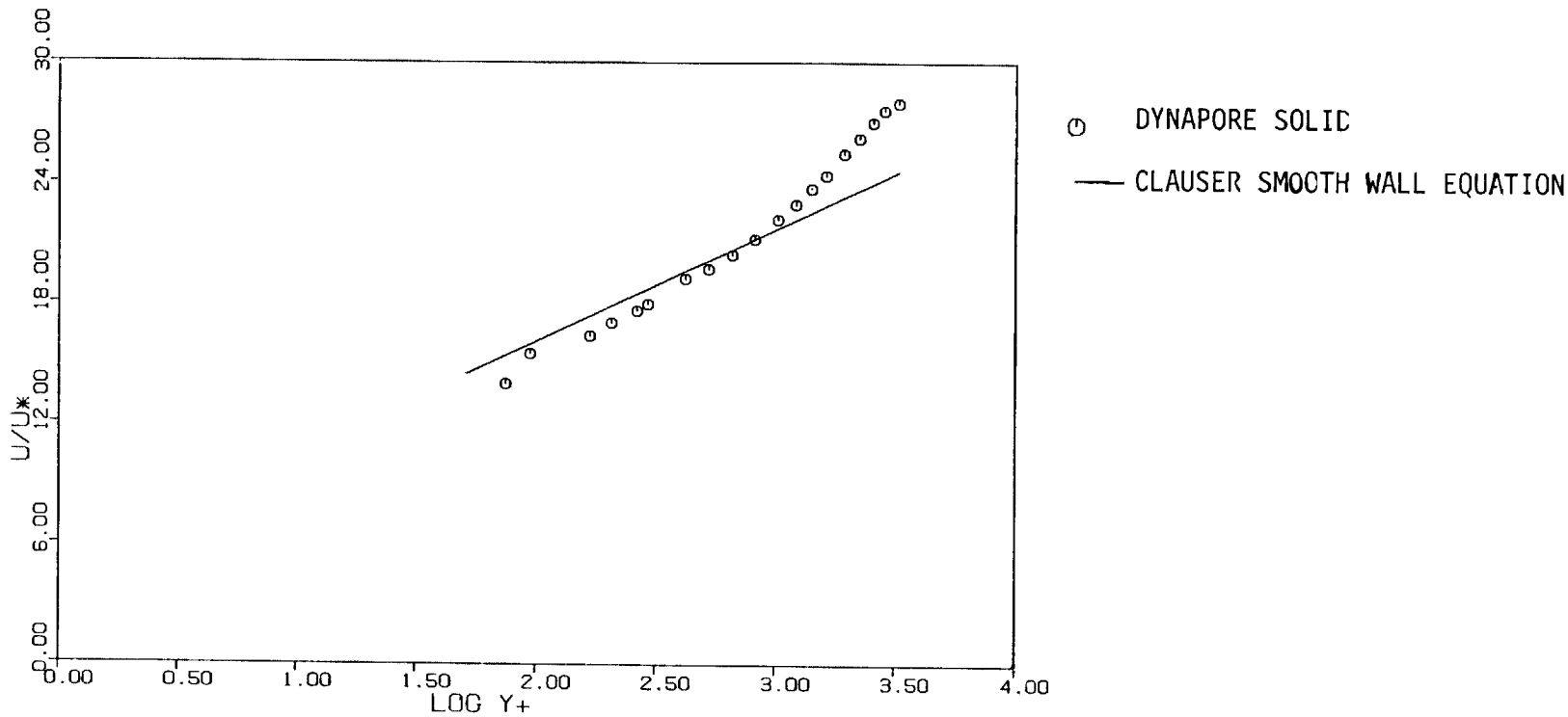

Fig. 37. Law of the Wall plot of solid Dynapore wall tests, station 5, q=17.8 cm. H_2O. Compared with Clauser's Log Law for a smooth wall.

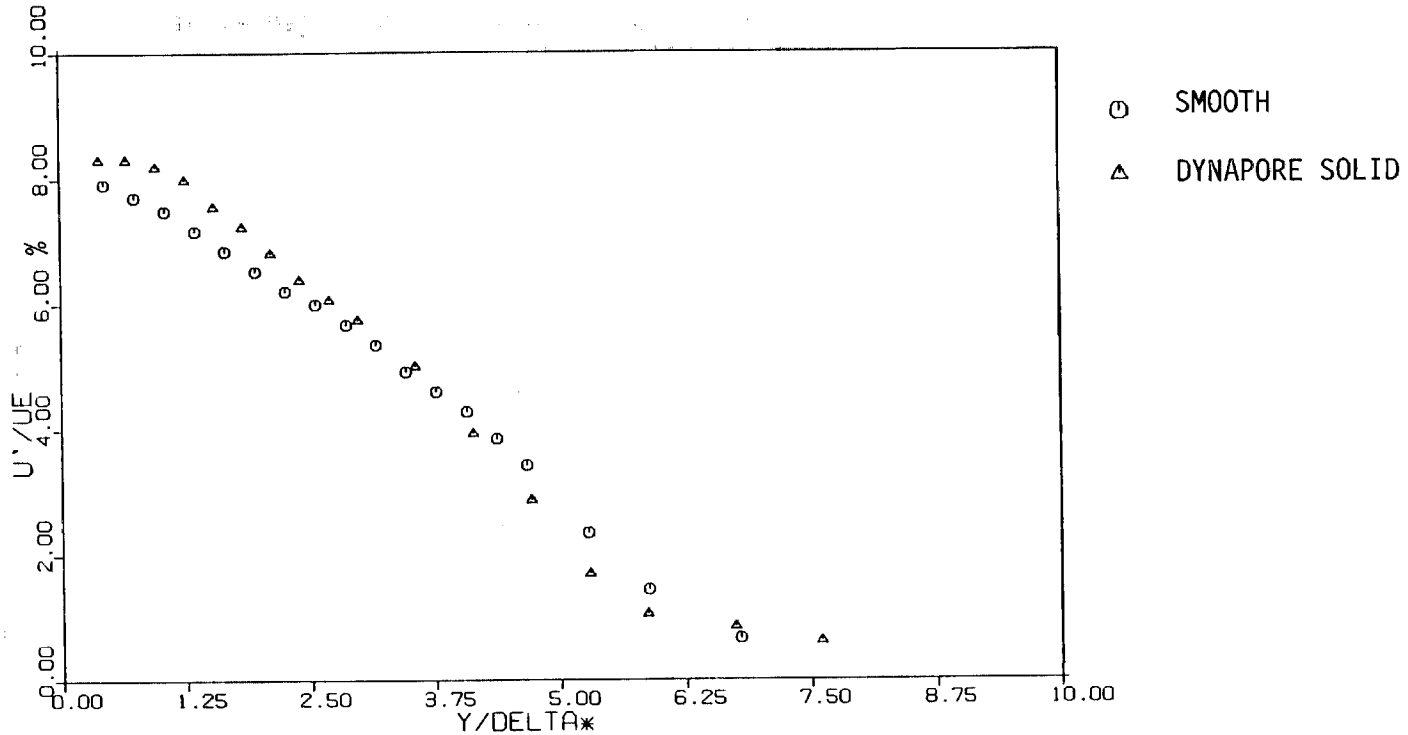

Fig. 38. Axial turbulence intensity profiles for smooth and solid Dynapore wall tests, station 4, q=17.8 cm. H_2O.

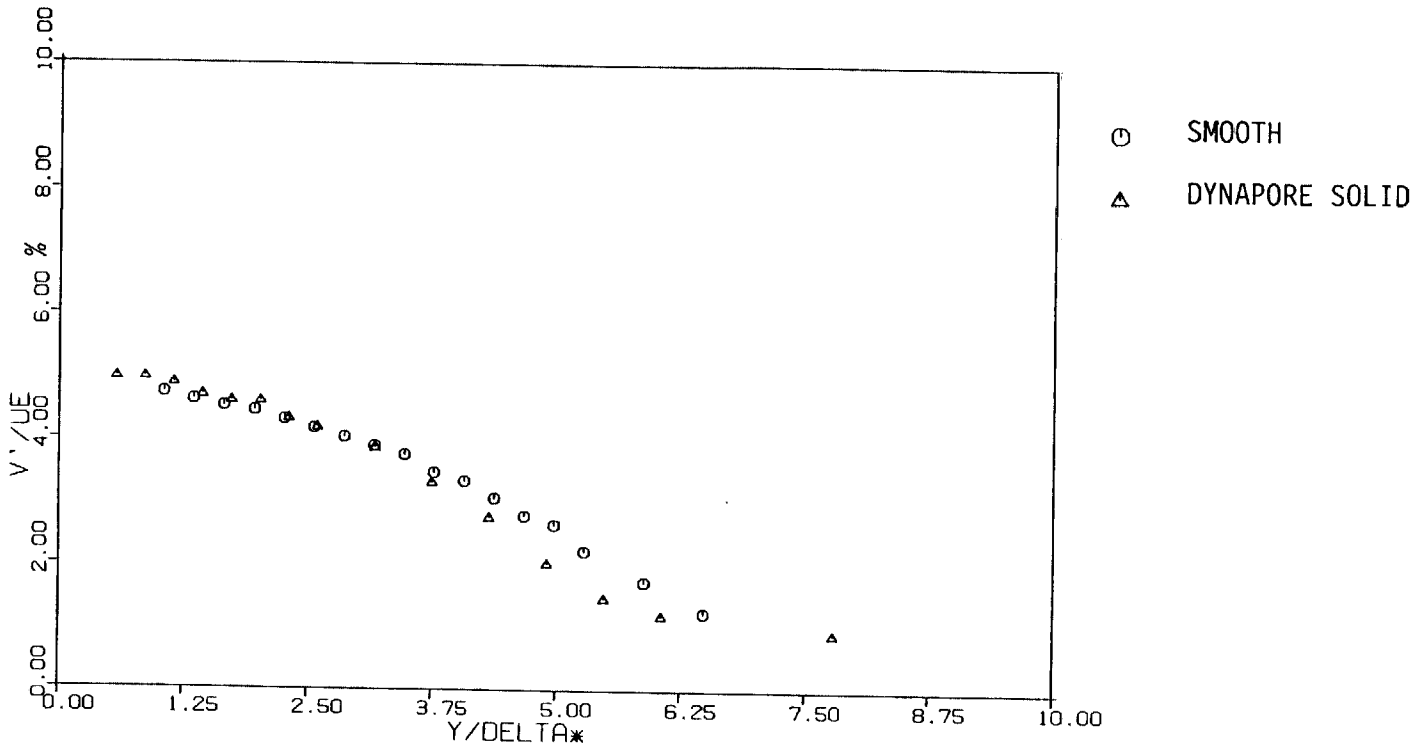

Fig. 39. Normal turbulence intensity profiles for smooth and solid Dynapore wall tests, station 4, q=17.8 cm. H_2O.

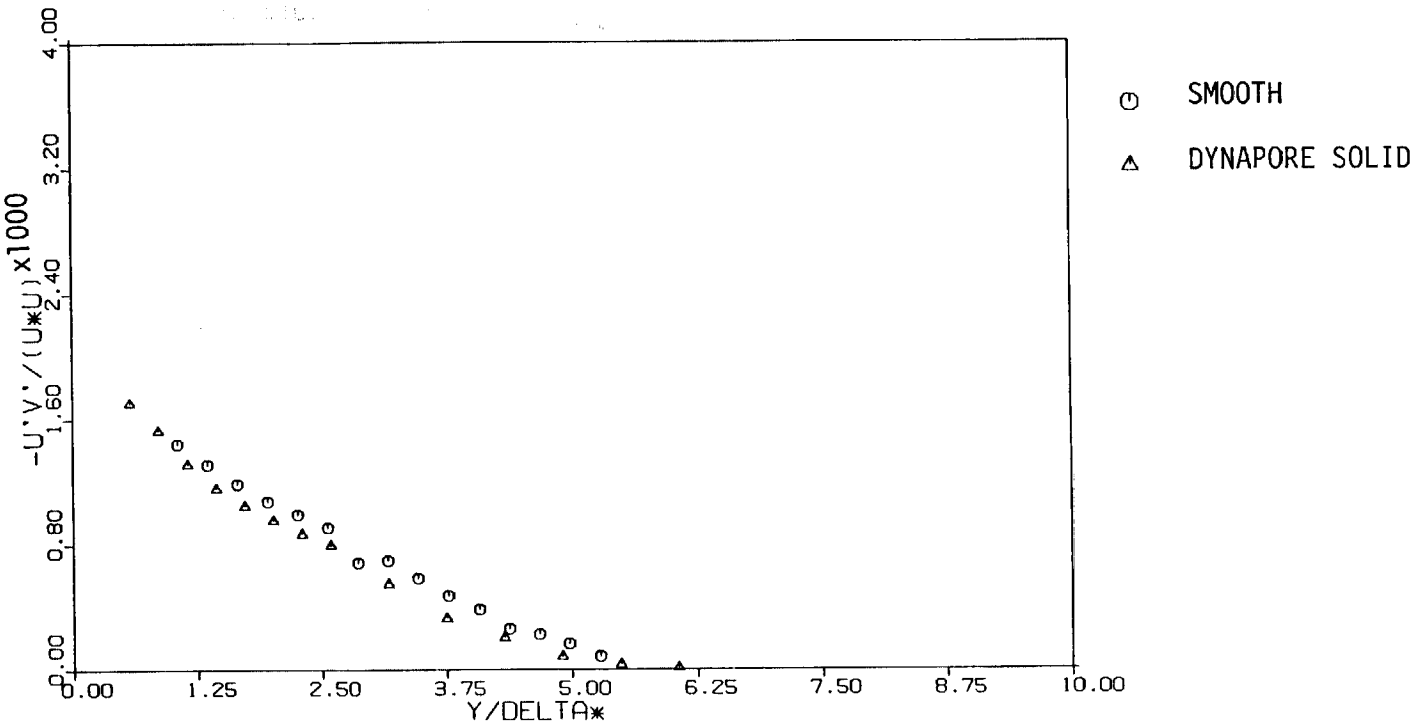

Fig. 40. Reynolds stress profiles normalized with local mean velocity for smooth and solid Dynapore wall tests, station 4, q=17.8 cm. H_2O.

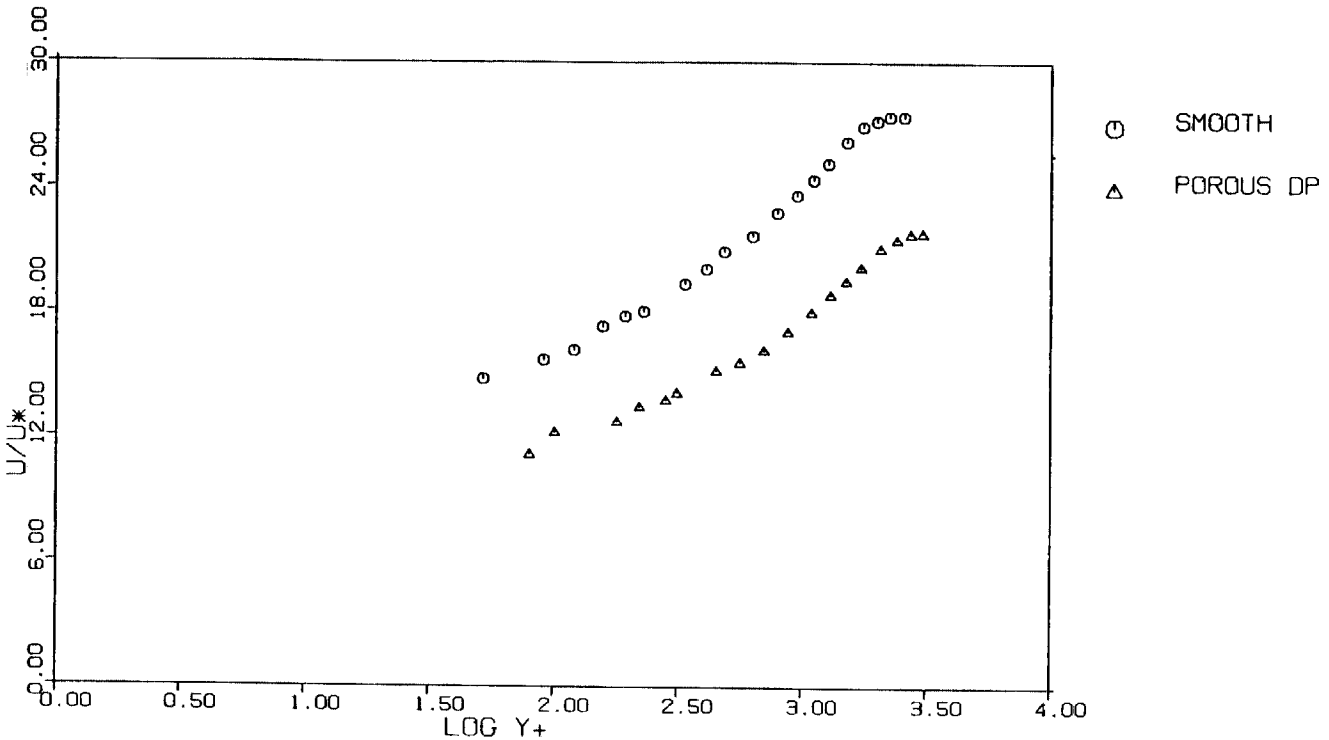

Fig. 41. Law of the Wall plot of smooth and porous Dynapore wall tests, station 4, q=12.7 cm. H_2O.

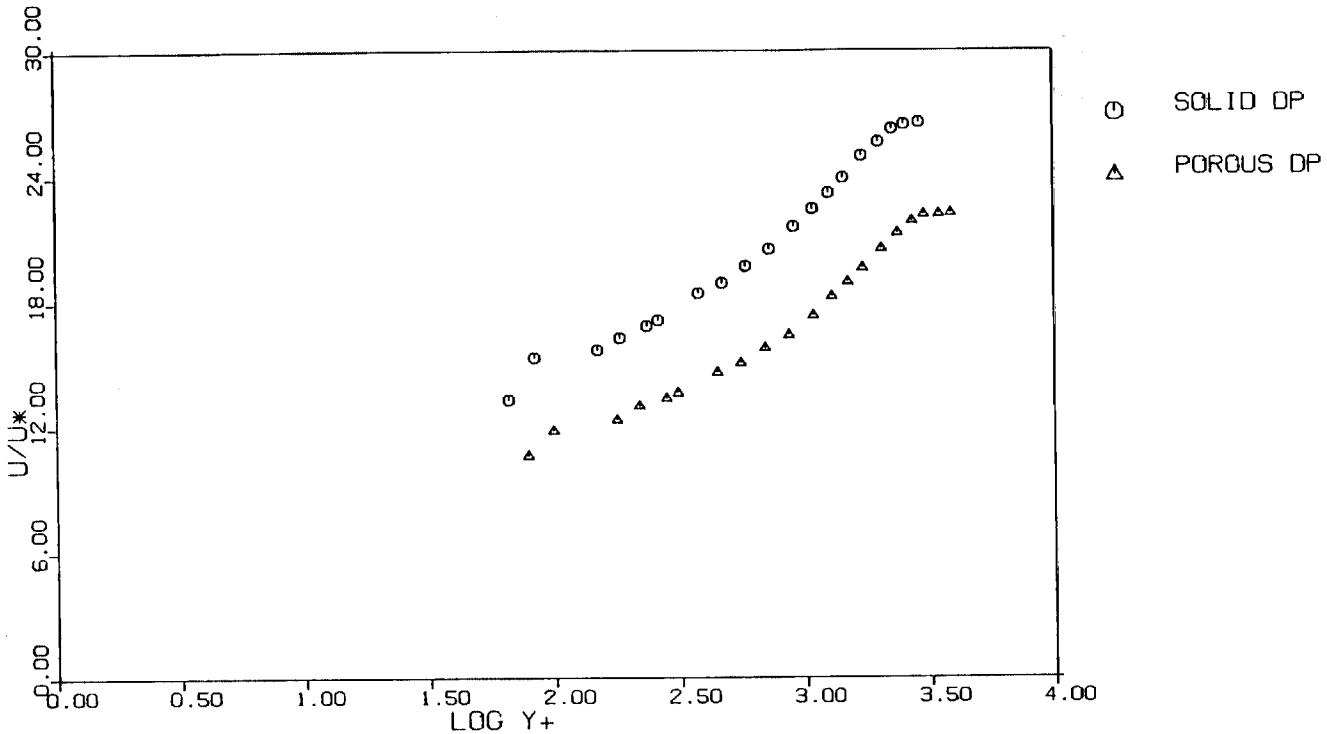

Fig. 42. Law of the Wall plot of solid Dynapore and porous Dynapore wall tests, station 5, q=12.7 cm. H_2O.

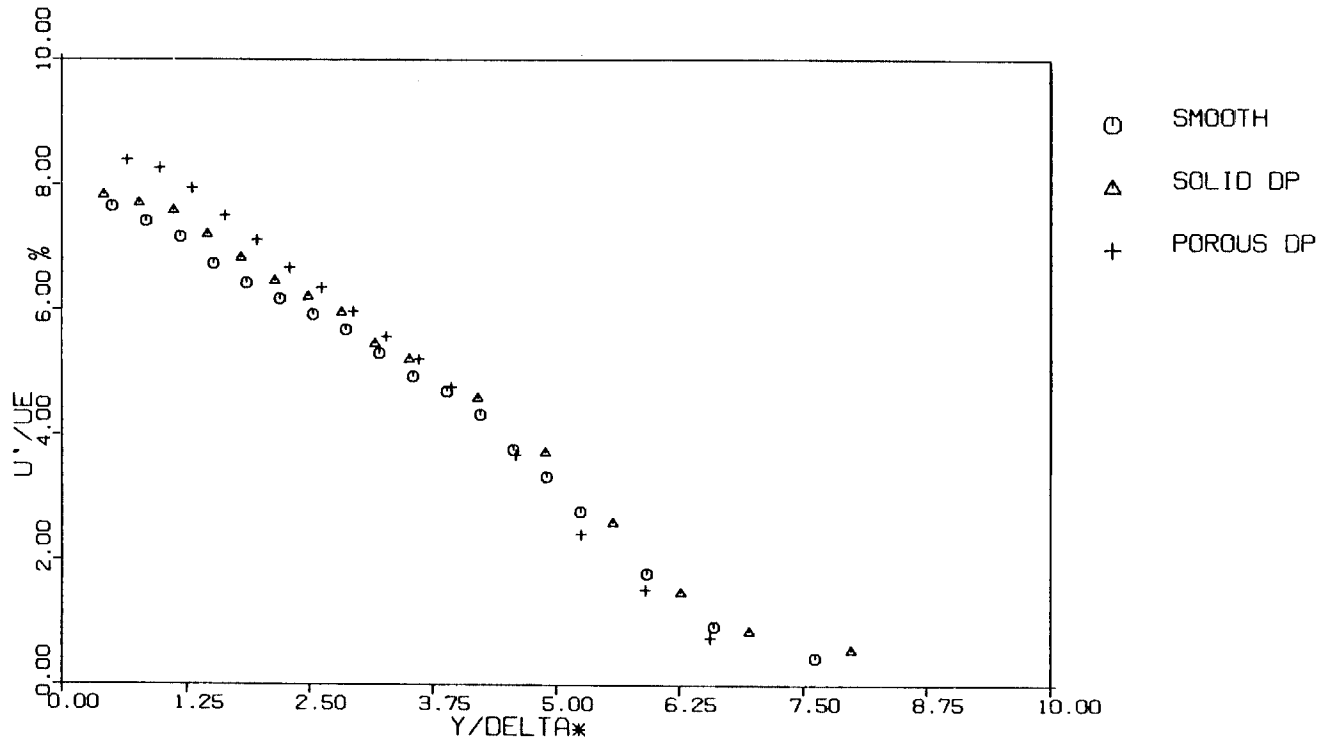

Fig. 43. Axial turbulence intensity profiles for smooth, solid Dynapore, and porous Dynapore wall tests, station 4, q=12.7 cm. H_2O.

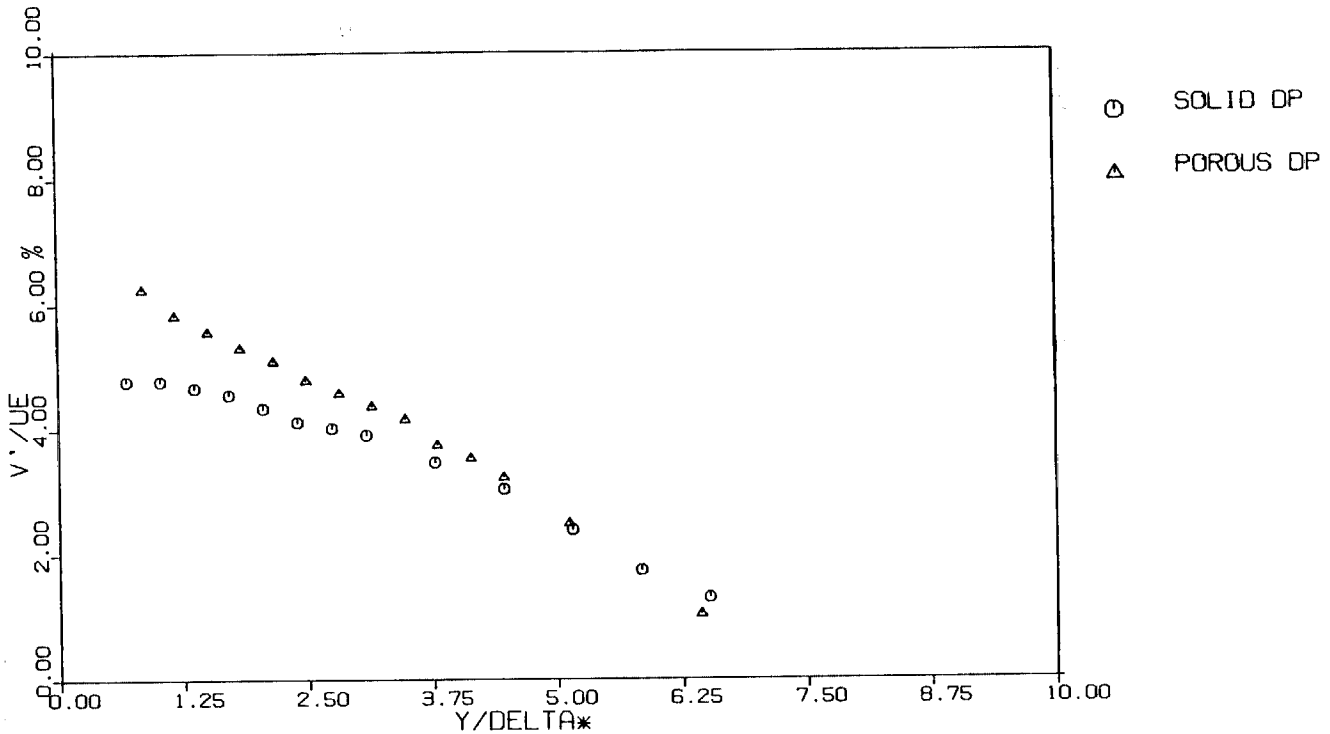

Fig. 44. Normal turbulence intensity profiles for solid Dynapore and porous Dynapore wall tests, station 4, q=12.7 cm. H_2O.

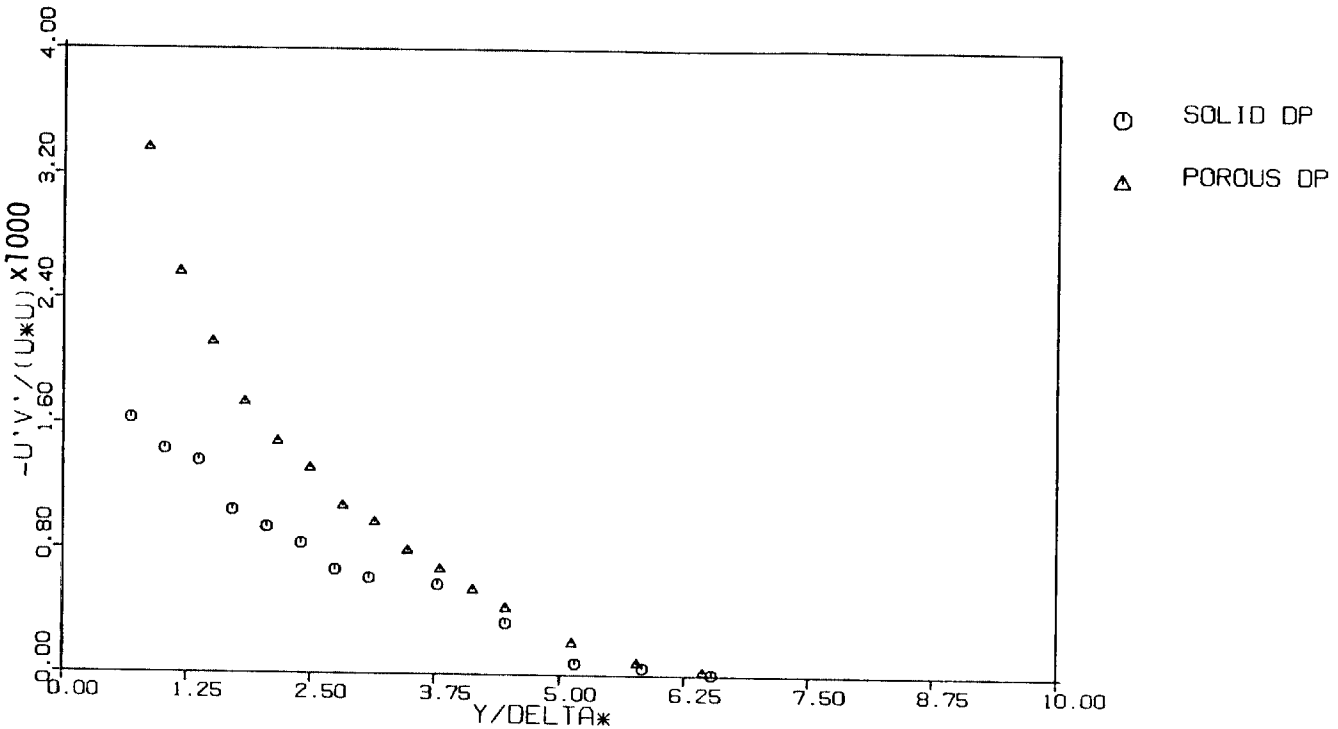

Fig. 45. Reynolds stress profiles normalized with local mean velocity for solid Dynapore and porous Dynapore wall tests, station 4, q=12.7 cm. H_2O.

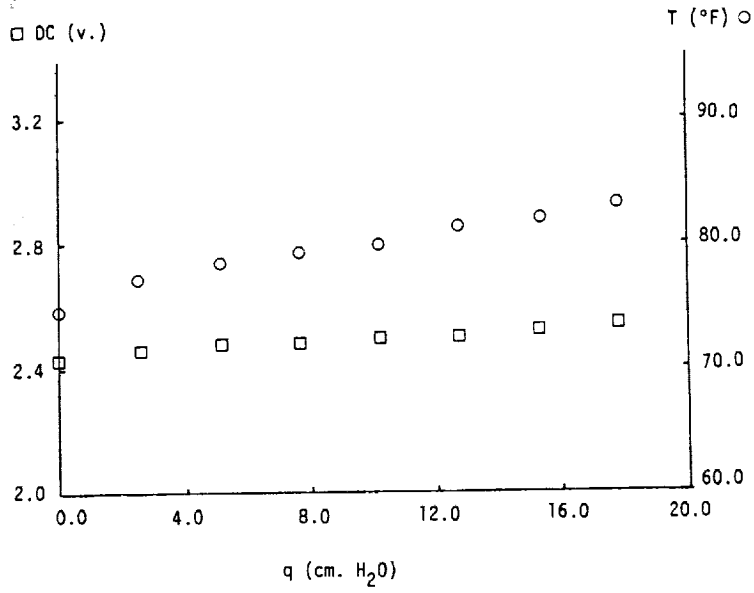

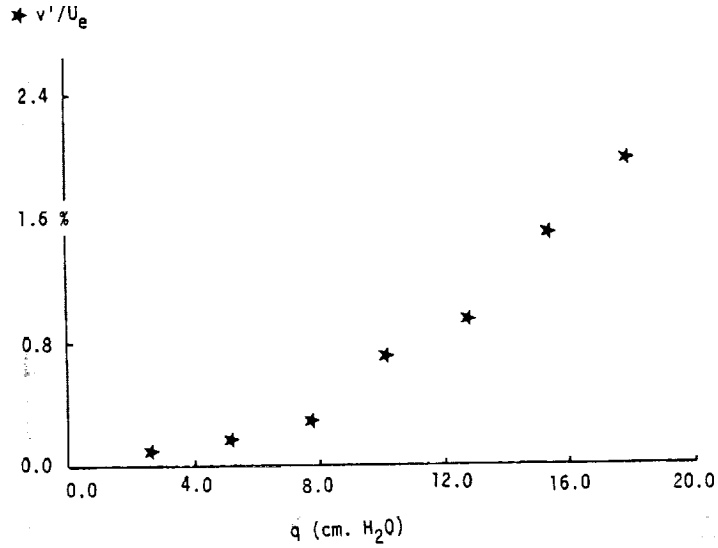

Fig. 46. Penetration of turbulence through the porous Dynapore wall.

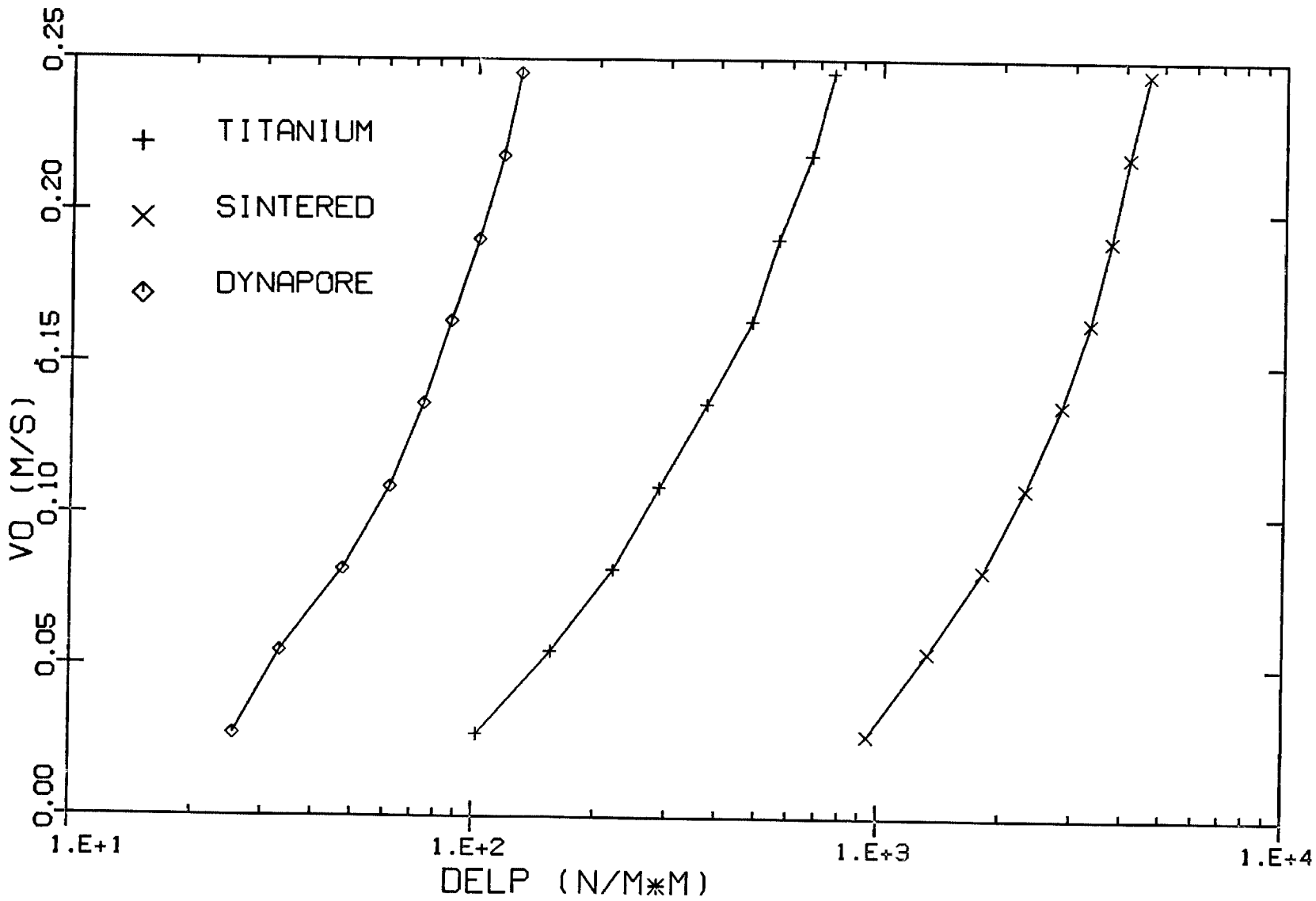

Fig. 47. Pressure Drop vs. Mass Flow for the Porous Materials

TABLE I

Some Recent Experimental Studies of Flow Over Solid and Porous Rough Surfaces

Investigator(s)	Model Geometry	Roughness Type	Roughness Size	Reynolds Number	Mach Number	Measured Quantities	Remarks
Fenter and Lyons 1958	flat plate (solid)	sphere of d = 0.004 in. and v - groove			M = 2.23 and 2.77	velocity profile	
Young 1965	flat plate (solid)	v - groove	$K^+ = 6 \sim 50$	$Re = 5 \times 10^6$	M = 5.0	velocity profile temp. profile skin friction directly	
Jeromin 1966	flat plate (porous)	sand grain d = 2.5 and 5 microns			M = 2.5 and	velocity profile, temp. profile, skin friction	air injection
Liu, Kline, and Johnson 1966	flat plate (solid)	square bar	K = 0.25 in.		U = 0.5 to 1.0 ft/sec	velocity profile, axial turb. intensity skin friction	water channel test

TABLE I (CONTINUED)

Investigator(s)	Model Geometry	Roughness Type	Roughness Size	Reynolds Number	Mach Number	Measured Quantities	Remarks
Scttron 1967	flat plate (solid)	screen d = 0.105 in.			U = 30 to 100 ft/sec	velocity profile, all turb. intensities, skin friction	adverse pressure gradient
Baker 1967	flat plate (porous)	sphere (sintered bronze) d = 0.003, 0.126, and 0.019 in.			U = 300 ft/ sec	velocity profile, axial turb. intensity skin friction	air injection
Perry, Schofield, and Joubert 1968	flat plate (solid)	d - type	K = 0.125, 0.5, and 1.0 in.		U = 67 to 106 ft/ sec	velocity profile skin friction	adverse pressure gradient
Thompson 1970	flat plate (solid)	sand grain	K = 0.005, 0.01, and 0.03 in.	Re = 2∿19x10^6	M = 1.5 2.5	velocity profile, temp. profile skin friction directly	
Wu 1973	flat plate (solid)	sphere d = 2.7 mm		Re = 10^5∿10^6	U = 0.77 2.62 m/sec	velocity profile skin friction directly	water channel test

TABLE I (CONTINUED)

Investigator(s)	Model Geometry	Roughness Type	Roughness Size	Reynolds Number	Mach Number	Measured Quantities	Remarks
Healzer, Moffat, and Keys 1974	flat plate (porous)	sphere d = 0.05 in.	K^+ = 20 to 200		U = 32 242 ft/sec	velocity pro- skin friction station number	air injection
Wood and Antonia 1975	flat plate (solid)	d-type	K = 0.125 in. K^+ = 70~150		U = 19 ft/sec	velocity pro- file, turb. intensities, shear stress	
O'Keefe, Casarella, and Demetz 1975	flat plate (solid)	sand grain	K^+ = 22~659	Re = 5.46×10^6	U = 100, 150, and 200 ft/ sec	velocity pro- file, skin friction wall pressure	
Reda, Ketter, and Far 1975	flat plate (solid)	sand grain and wave type	K = 0.002 to 0.027 in.		M = 2.9	velocity pro- file, skin friction directly	
Furuya, Miyata and Fuyita 1976	flat plate (solid)	wire d = 2 mm			U = 13 and 21 m /sec	velocity pro- file, skin friction, pressure distribution around the wire	

TABLE I (CONTINUED)

Investigator(s)	Model Geometry	Roughness Type	Roughness Size	Reynolds Number	Mach Number	Measured Quantities	Remarks
Keel 1977	cone (solid)	sand grain	K = 0.02 and 0.045 in. K^+ = 100~1000		M = 2.5 and 5.0	velocity profile, skin friction directly wall temp.	
Naragana 1977	flat plate (solid)	sand grain 24 and 40 grit			U = 20m/sec	velocity profile, skin friction	adverse and favorable pressure gradient
Pimenta, Moffat, and Keys 1979	flat plate (porous)	copper ball			U = 11~40 m/sec	velocity profile, temp. profile, velocity fluctuation temp. fluctuation, skin friction, station number	air injection
Voisinet 1979	flat plate (porous)	screen	K = 0.004, 0.013, and 0.049 in. K^+ = 10~500		M = 2.9	velocity profile, temp. profile, skin friction directly	air injection

TABLE II

Six Cases Studied in the Current Experiments

Cases Studied	Surface	Conditions	Roughness Type	Test Condition
smooth wall	solid	smooth		
sand-roughened wall	solid	rough	sand grain, type K = 0.0042 cm.	$K^+ \simeq 5 \sim 7$
sintered metal porous wall	porous	rough	particle type, K = 0.0040 cm.	$K^+ \simeq 5 \sim 7$
perforated titanium wall	porous	smooth		
solid Dynapore wall	solid	rough	screen mesh type, d = 0.0076 cm.	$K^+ \simeq 9 \sim 10$
porous Dynapore wall	porous	rough	screen mesh type, d = 0.0076 cm.	$K^+ \simeq 9 \sim 10$

TABLE III

Experimental Skin Friction Coefficients

Station	Smooth, Solid wall	600 Grit Sandpaper	Sintered Porous Wall	Perforated Titanium Wall	Solid Dynapore	Porous Dynapore
			Q = 12.7 cm. H_2O			
1	0.00327	0.00396	-	-	-	-
2	0.00299	0.00361	-	-	-	-
3	0.00297	0.00337	-	-	0.0033*	0.0049
4	0.00257 (0.00277, 1975)	0.00301	0.00433 (0.00404, 1975)	0.00373	0.0030*	0.0044
5	-	-	-	0.00351	0.00308	0.00428
			Q = 17.8 cm. H_2O			
1	0.00274	0.00368	-	-	-	-
2	0.00264	0.00332	-	-	-	-
3	0.00257	0.00316	-	-	0.0028*	0.0043
4	0.00254 (0.00259, 1975)	0.00308	0.00417 (0.00371, 1975)	0.00333	0.0027*	0.0040
5	-	-	-	0.00317	0.00278	0.00364

* Calculated from Momentum Integral Method

1. Report No.	2. Government Accession No.	3. Recipient's Catalog No.
NASA CR-3612		

4. Title and Subtitle	5. Report Date
TURBULENT BOUNDARY LAYER OVER SOLID AND POROUS SURFACES WITH SMALL ROUGHNESS	September 1982
	6. Performing Organization Code
7. Author(s)	8. Performing Organization Report No.
Fred Y. Kong, Joseph A. Schetz, and Fayette Collier	
	10. Work Unit No.
9. Performing Organization Name and Address	11. Contract or Grant No.
Virginia Polytechnic Inst. & State University Aerospace and Ocean Engineering Department Blacksburg, VA 24060	NAG-1-119
	13. Type of Report and Period Covered
12. Sponsoring Agency Name and Address	Contractor Report
National Aeronautics and Space Administration Washington, D.C. 20546	14. Sponsoring Agency Code

15. Supplementary Notes

Langley Technical Monitor - Jerry N. Hefner
Final Report

16. Abstract

Experimental studies were conducted to obtain direct measurements of skin friction, mean velocity profiles, axial and normal turbulence intensity profiles, and Reynolds stress profiles in the untripped boundary layer on a large-diameter, axisymmetric body with a smooth, solid surface; a sandpaper-roughened, solid surface; a sintered metal, porous surface; a "smooth" perforated titanium surface; a rough, solid surface made of fine, diffusion-bonded screening; and a rough, porous surface of the same screening. The roughness values were in low range (k^+ = 5-7) just above what is normally considered "hydraulically smooth." Measurements were taken at several axial locations and two nominal freestream velocities, 45.1 and 53.3 m/sec.

17. Key Words (Suggested by Author(s))	18. Distribution Statement
porous wall boundary layer turbulent boundary layer skin friction balance data	Unclassified - Unlimited Subject Category - 34

19. Security Classif. (of this report)	20. Security Classif. (of this page)	21. No. of Pages	22. Price
Unclassified	Unclassified	90	A05

For sale by the National Technical Information Service, Springfield, Virginia 22161

NASA-Langley, 1982